SAPIENZA
UNIVERSITÀ DI ROMA

Thermal Effects in Nuclear Matter and Neutron Stars

Scuola di dottorato "Vito Volterra"
Dottorato di Ricerca in Fisica (XXXVI cycle)

Lucas Tonetto Coimbra
ID number 1978054

Advisor
Prof. Omar Benhar

Academic Year 2022/2023

Thesis defended on 30 May 2024
in front of a Board of Examiners composed by:

Prof. Constança Providência, Prof. Roberto Maiolino, Prof. Paola Leaci (chairwoman)

Thermal Effects in Nuclear Matter and Neutron Stars
PhD thesis. Sapienza University of Rome

This thesis has been typeset by LaTeX and the Sapthesis class.

Author's email: lucas.tonetto@uniroma1.it

"Absque sudore et labore nullum opus perfectum est".

Schrevelius 1176

Abstract

In different astrophysical environments involving neutron stars, such as mergers or newly born stars, a reliable model of a finite-temperature equation of state is needed. Temperature has implications in equilibrium and dynamical phenomena, therefore a fully consistent framework should be able to take into account thermal effects in single-nucleon properties alongside yielding accurate results for average thermodynamic quantities.

In this Thesis, we employ a recently developed effective interaction based on the Correlated Basis Functions theory, being able to account for nuclear correlations and two- and three-nucleon potentials. After extensively discussing the properties of its generalisation to nonzero temperature, we apply it in the calculation of the neutrino mean free path and emissivity. In the latter, we study how effective weak transition operators alter the results.

Acknowledgements

Many individuals have significantly contributed to my scientific and personal development throughout my career, and I am profoundly grateful to each one of them.

First and foremost, I want to acknowledge my mother, a strong and independent woman who has always supported me in my journey through science and life. She instilled in me the value of acquiring knowledge, which has been invaluable to my growth.

Secondly, I extend my deepest gratitude to Omar, my Ph.D. supervisor. Beyond imparting vast knowledge of physics, he and his family have made me feel welcomed and at home — a kindness I will never forget. Our numerous meetings at Villa Borghese broadened my perspectives on science, life, art, and history (along with picking up the Roman accent).

My friends have played a pivotal role in this Thesis, and the list is extensive. I want to start with Andrea, my Ph.D. fellow, who has always been ready to answer my questions and engage in discussions about physics. Moreover, I must highlight the duo we formed during our historic Thursday football matches.

Since the beginning of my Ph.D., I have shared the joys and stresses of research with my close friend, Rodrigo. We embarked on and completed our Ph.D. journey together. As office mates, we also enjoyed many beers and panini in San Lorenzo, filled with laughter and conversations about Brazil and Mexico.

I also want to thank Andreas, who entered my life in the last year of my Ph.D. journey. Despite our late meeting, we became great friends, and our gym sessions struck a perfect balance between fun and serious discussions. I am looking forward to our first powerlifting competition.

Elisa, whom I met during my master's program, has been a special contributor to this Thesis. Her advice and friendship have been crucial to my development during my Ph.D. Always kind, she and I have shared many conversations about both professional and personal matters.

Lorenzo, whom I met in my early days at Sapienza, has proven to be an extremely valuable friend. Our trips to the beach and the mountains provided immense fun and peace of mind. I am glad we can complain about the price of gelato together.

I must also thank Jonas, who has continually opened doors for me since our meeting in 2016. He has become one of my best friends and is one of the most intelligent individuals I have ever known. He offered me numerous opportunities to learn about physics and many other aspects of life.

I extend my gratitude to all those who have contributed to my daily joy and work over the years. These include my office mates, department fellows, the gravity group, and my adoptive research group of soft matter: Francesco, Camilla, Elisa, Flavio, Fabrizio, Susy, Diogo, Leah, Beth, Gabriele, Ojus, Rafa, Viri, Caja, Adriano, Marco, Loris, Fabrizio, Giuseppe, Massimo, Pantelis, Sebastián, and Stefano.

I am also extremely grateful to my Brazilian friends, who, despite the distance, have remained fundamental to my life. They include Thiago, Jéferson, Daniel, André, Frizo, Sasso, Natália, Antônio, Pessôa, Rafael, João, Alessandro, Henrique, Maurício, and many more.

Finally, I want to thank Sapienza and all its personnel for their support over the

years. It is a pleasure to call Rome and Italy my second home. All of my friendships and experiences will remain deeply rooted in my mind.

Contents

List of Figures

Introduction

A quantitative description of the properties of dense nuclear matter at both zero and nonzero temperature—needed to carry out numerical simulations of many astrophysical processes involving neutron stars—entails non trivial conceptual and computational issues, associated with both the modelling of nuclear dynamics and the treatment of the quantum-mechanical many-body problem.

Advanced theoretical studies of dense hadronic matter are mainly based on either Relativistic Mean-Field Theory (RMFT) or non relativistic Nuclear Many-Body Theory (NMBT); see, e.g., Refs. [3] and [4], respectively. Both theoretical approaches rest on the paradigm according to which nuclear systems can be described as collections of interacting point like nucleons. It is remarkable that the validity of this assumption up to densities as high as $(4-5)\ \varrho_0$—with $\varrho_0 = 2.7 \times 10^{14}$ g/cm^3 being the equilibrium density of isospin-symmetric nuclear matter at zero temperature—is unambiguously confirmed by the observation of y-scaling in electron-nucleus scattering data at large momentum transfer[5].

This Thesis describes a recent approach, based on the formalism of NMBT and an effective Hamiltonian derived from phenomenological models of two- and three-nucleon interactions, suitable to carry out perturbative calculations of nuclear matter properties relevant to the interpretation of multimessenger signals detected by existing and future observational facilities. The proposed model is expected to be applicable in the region of temperatures $T \ll m_\pi$, with $m_\pi \approx 140$ MeV being the pion mass, in which nucleons are the relevant degrees of freedom.

A distinctive feature of our work is the use of a density-dependent effective Hamiltonian derived from state state-of-the-art phenomenological potentials—strongly constrained from nucleon-nucleon scattering data and the observed properties of the few-nucleon bound states—employing the formalism of correlated basis functions, or CBF, and the cluster expansion technique; see, e.g., Refs. [6, 7]. This procedure allows to renormalise the bare nucleon-nucleon potential in such a way as to take into account screening effects arising from nucleon-nucleon correlations, which dramatically suppress the probability of finding two nucleons within a distance $r \lesssim 1$ fm,

Unlike the bare nuclear forces, the CBF effective interaction, which takes into account both two- and irreducible three-nucleon interactions, is well behaved, and can be employed to study equilibrium and dynamical properties of hot nuclear matter using a scheme based on many-body perturbation theory, in which thermodynamic consistency is preserved by construction. In addition to the Equation of State (EOS) of charge-neutral β-stable matter, describing the density dependence of mater pressure at fixed temperature, the results discussed in this Thesis include single-

nucleon properties, notably energy spectra, effective masses and chemical potentials, obtained from the same effective Hamiltonian. These quantities have been employed as input for the calculations of the neutrino emissivity and mean free path in nuclear matter within the mean-field approximation. This study has been carried out taking into account, for the first time, the temperature dependence of the single-nucleon energies, the effects of which turn out to be significant.

The analysis of neutrino emission and interactions has been also pushed beyond the mean-field approximation by defining effective vector and axial-vector weak currents—driving the Fermi and Gamow-Teller nuclear transitions, respectively—using the same formalism employed to obtain the effective Hamiltonian. The inclusion of correlation effects leads to a significant quenching of the weak interaction rates, exhibiting distinct density and temperature dependence. The role of thermal and correlation effects in determining the density dependence of the neutrino emissivity associated with the occurrence of direct Urca processes has been thoroughly analysed and discussed.

This Thesis is organised as follows. Chapter 1 is devoted to a summary of nuclear structure, as well as of the microscopic models of nuclear dynamics underlying nuclear many-body theory. The theoretical description of the properties at zero and finite temperature nuclear matter based on the CBF effective Hamiltonian is discussed in Chapter 2. In Chapter 3, we present the results of the neutrino mean free path in neutrino-transparent and neutrino-opaque matter by using the mean field approximation with density-temperature dependent effective masses. The deviations from the mean field approximation arising from correlation effects, leading to a quenching of the weak transition matrix elements, are analysed in Chapter 4 considering the neutrino emissivity. Finally, Chapter 5 is devoted to a summary of our findings, as well as an overview of the future developments of our work.

Chapter 1

Nuclear dynamics

Understanding the properties of matter at densities comparable to the central density of atomic nuclei ($\varrho_0 = 0.16$ fm^{-3}) is made difficult by both the complexity of the interactions and the approximations necessarily implied in the theoretical description of quantum-mechanical many-particle systems. The scenario becomes even more problematic as we enter the regime of supranuclear densities ($\varrho > \varrho_0$), as the available empirical information is scarce, and one has to unavoidably resort to a mixture of extrapolation and speculation.

The fundamental theory describing strong interactions is currently accepted to be Quantum Chromodynamics (QCD). However, its application poses significant challenges due to the intricate nature of the strong force and the non-perturbative aspects of quark and gluon interactions, the elementary fields of the theory. The two approaches which yield the most well-grounded results are perturbative QCD and lattice QCD. The former is effective at describing high-energy processes where quarks and gluons interact with large momentum transfers. However, at low energies or in the confinement regime, the strong coupling constant becomes large, making perturbation theory impractical and unreliable. Lattice QCD, on the other hand, is a numerical approach particularly powerful for studying non-perturbative QCD phenomena, such as confinement and the properties of hadrons. The simulations face challenges related to the computational cost and the need for large-scale supercomputers, though. Additionally, the method is plagued by the so-called sign problem.

Bridging the gap between the above mentioned regimes is a central challenge in understanding the full spectrum of strong interactions. In particular, neutron stars (NSs), the astrophysical system that we analyse in this Thesis, belong to the density regime of few ϱ_0 and a temperature ranging from $T/T_F \ll 1$ (stars that have undergone most of their thermonuclear evolution) and $T/T_F \sim 0.1-1$ (proto-neutron stars or NS mergers), where $T_F \sim 10^{12} K$. In cold stars, thermal effects can be safely neglected when determining equilibrium properties, such that the equation of state (EOS) is assumed to be at $T = 0$. In the second scenario, temperature does play a role in equilibrium and non-equilibrium properties.

In the NS regime, the formalism of Nuclear Many-Body Theory (NMBT) comes in useful, because nucleons (protons and neutrons) are the dominant degrees of freedom. It has proven to be a successful and versatile theory when analysing atomic nuclei and infinite nuclear matter systems and will be the cornerstone of the results

we present in this Thesis.

In this chapter, we first discuss some empirical properties of nuclear matter and how we can take advantage of NMBT to describe physical systems. At the end, we point out the differences of the models used here with respect to alternative approaches to tackle the nuclear many-body problem, namely, chiral potentials and relativistic mean field theories.

1.1 Bulk properties of nuclear matter

The large body of data on nuclear masses can be used to constrain the density dependence predicted by theoretical models of uniform nuclear matter at zero temperature. The (positive) binding energy per nucleon can be defined as [1]

$$\frac{B(A,Z)}{A} = \frac{1}{A}[Nm_n + Z(m_p + m_e) - M(A,Z)] \tag{1.1}$$

where Z is the number of protons, A is the number of nucleons, $N = A - Z$ is the number of neutrons, while m_p, m_n, and $M(Z,A)$ denote the measured proton, neutron and nuclear masses, respectively. The A and Z dependence of $B(Z,A)$ can be parameterised according to the *semiempirical-mass* formula based on the liquid-drop model and the shell model [8, 9]

$$\frac{B(A,Z)}{A} = \frac{1}{A}[a_V A - a_S A^{2/3} - a_C \frac{Z^2}{A^{1/3}} - a_A \frac{(A-2Z)^2}{4A} + \lambda a_p \frac{1}{A^{1/2}}]. \tag{1.2}$$

The first term, called *volume term*, describes the bulk energy of nuclear matter. The second term is associated with the surface energy and the third one manifests the Coulomb repulsion between Z protons uniformly distributed within a sphere (nuclear radii are roughly proportional to $A^{1/3}$). The fourth term is called *symmetry* term, which accounts for the experimental observation that stable nuclei tend to have the same number of neutrons and protons. Furthermore, even-even nuclei (*i.e.* nuclei having even Z and even $A - Z$) tend to be more stable than even-odd or odd-odd nuclei. The last term accounts for that, where $\lambda = +1, 0, -1$ for even-even, even-odd and odd-odd nuclei, respectively.

In the $A \to \infty$ limit and neglecting the effect of Coulomb repulsion between protons, the only term surviving is the term linear in A. Therefore, a_V can be identified as the binding energy per nucleon of nuclear matter, defined as a uniform system consisting of inifinite numbers of protons and neutrons subject to strong interactions only. In the case of *isospin-symmetric nuclear matter* (SNM), with $N = Z = A/2$, one finds

$$\frac{B(A,Z)}{A} = -\frac{E_0}{A} \approx 16 \ \frac{\text{MeV}}{A}, \tag{1.3}$$

where E_0 can be identified as the ground-state energy of the system.

The equilibrium density of such a system, ϱ_0, can be inferred exploiting saturation of nuclear densities. Nuclear charge-density distributions, obtained from

[1] In this Chapter, we adopt the system of natural units, in which $\hbar = c = k_B = 1$. Unless otherwise specified, we also neglect the small proton-neutron mass difference.

measurements of electron-nucleus cross sections in the elastic scattering regime, show that the central density of atomic nuclei, does not depend upon A for large A (see Fig. 1.1). This corresponding *saturation density*, ϱ_0, is found to be

$$\varrho_0 = \lim_{A\to\infty} \frac{A}{Z}\varrho_{\rm ch}(r=0) = 0.16 \text{ fm}^{-3}. \tag{1.4}$$

The saturation property indicates that nuclei are nearly incompressible, i.e., that nuclear forces become strongly repulsive at short distances.

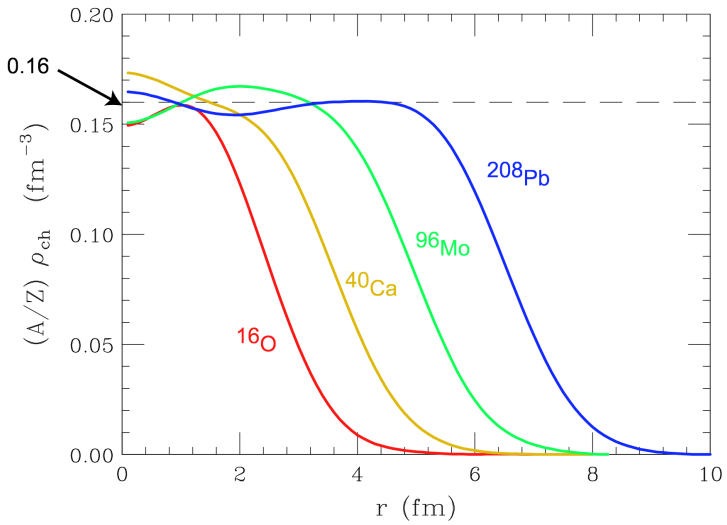

Figure 1.1. Radial dependence of the charge-density distributions of nuclei, normalised to the nuclear mass number A.

In the vicinity of ρ_0 in SNM, one can expand the energy per particle as

$$E_{\rm SNM}(n) = E_{\rm SNM}(n_0) + \frac{1}{2}\left(\frac{d^2E_{\rm SNM}}{dn^2}\right)_{n_0}(n-n_0)^2 + \frac{1}{6}\left(\frac{d^3E_{\rm SNM}}{dn^3}\right)_{n_0}(n-n_0)^3 + \cdots \tag{1.5}$$

where we can define the compressibility

$$K_0 = 9n_0^2\left(\frac{d^2E_{\rm SNM}}{dn^2}\right)_{n_0} \tag{1.6}$$

and skewness

$$Q_0 = 27n_0^3\left(\frac{d^3E_{\rm SNM}}{dn^3}\right)_{n_0}. \tag{1.7}$$

K_0 can be easily related to the pressure noting that $P = \varrho^2(\partial E_{\rm SNM}/\partial\varrho)$, so

$$K_0 = 9\left(\frac{\partial P}{\partial\varrho}\right)_{\varrho_0}. \tag{1.8}$$

K_0 can be extracted from the measured excitation energies of nuclear vibrational states. Due to the difficulties implied in the analysis of these experiments, empirical

estimates of K_0 have a large uncertainty. The values range from ≈ 200 MeV (*soft EOS*) to ≈ 300 MeV (*stiff EOS*). The authors of Refs. [10, 11] have obtained the value $K_0 = 240 \pm 20$ MeV after analysing experimental data.

NS matter is expected to be neutron rich, thus isospin asymmetric. Defining the proton and neutron fractions to be $x_p = \varrho_p/\varrho$ and $x_n = \varrho_n/\varrho = 1 - x_p$, respectively, one could also expand E/A in powers of $\delta = 1 - 2x_p$ around $\delta = 0$ for any given density

$$\frac{E(\varrho,\delta)}{A} = E(\varrho,0) + E_{\rm sym}\delta^2 + \mathcal{O}(\delta^4) \tag{1.9}$$

$$= E_{\rm SNM}(\varrho) + E_{\rm sym}(\varrho)(1-2x_p)^2 + \cdots \quad . \tag{1.10}$$

The term $E_{\rm sym}$ is the nuclear symmetry energy

$$E_{\rm sym} = \left(\frac{\partial^2 E(\varrho,\delta)}{\partial\delta^2}\right)_{\delta=0} \approx E(\varrho,1) - E(\varrho,0). \tag{1.11}$$

and can be readily interpreted as the energy required to convert SNM into Pure Neutron Matter (PNM).

The density dependence of $E_{\rm sym}(\varrho)$ can also be analysed expanding around the equilibrium density of SNM, ϱ_0,

$$E_{\rm sym}(\varrho) \approx E_{\rm sym}(\varrho_0) + \left(\frac{\partial E_{\rm sym}}{\partial\varrho}\right)_{\varrho_0}(\varrho-\varrho_0) = E_{\rm sym}(\varrho_0) + \frac{L}{3}\frac{(\varrho-\varrho_0)}{\varrho_0} + \cdots, \tag{1.12}$$

where the *symmetry energy slope* is defined as

$$L = 3\varrho_0\left(\frac{dE_{\rm sym}}{d\varrho}\right)_{\varrho_0}. \tag{1.13}$$

The symmetry energy dictates how energetically expensive it is to convert a proton into a neutron, hence it is extremely relevant in the context of NS matter. A broad discussion on the constraints on the symmetry energy and the slope L can be found in Refs. [9, 12–14]. In particular, the authors of Ref. [15] have done a survey of 28 analyses and report the results $E_{\rm sym}(\varrho_0) = 31.6 \pm 2.66$ MeV and $L = 58.9 \pm 16$ MeV.

On the astrophysical side, many works have attempted to infer $E_{\rm sym}$ and L from gravitational-wave and electromagnetic observations (see, e.g.,Refs. [16–21]). Despite being remarkable the progress in estimating these parameters from astrophysical observations, the uncertainty is still too large to draw a firm conclusion.

Special attention was drawn to the results of the PREX-II electron-nucleus scattering experiment when they were applied to the determination of L [22]. PREX-I and PREX-II had the goal of measuring the neutron skin thickness, related to L through a fit established within a given theory of dense matter. In Reed *et al.* [22], the FSU2Gold relativistic mean field parametrisation is used on PREX-II data to extract $L = (106 \pm 37)$MeV, a rather large value in comparison with previous experimental results. It suggests that the NS EOS may be much stiffer than what formerly thought after the observation of GW170817 [23]. Yüksel and Paar [24] provide an analysis of the joint results coming from PREX-I, PREX-II, and CREX experiments. It should be pointed out that, despite being interesting results, they should be carefully taken into consideration before strongly constraining nuclear properties.

1.2 The paradigm of Nuclear Many-Body Theory

Nuclear Many-Body Theory is based on the hypothesis that all nucleon systems—from the deuteron, having mass number $A = 2$, to neutron stars, wherein $A \sim 10^{57}$—can be described in terms of point-like protons and neutrons, the interactions of which are driven by the Hamiltonian

$$H = \sum_i \frac{\mathbf{k}_i^2}{2m} + \sum_{i<j} v_{ij} + \sum_{i<j<k} V_{ijk} \ , \tag{1.14}$$

with m and $\mathbf{k}_i$ denoting the mass and momentum of the i-th particle.

Before analysing the main features of the potentials appearing in Eq. (1.14), we should first comment on the foundation of NMBT. As written before, neutrons and protons have actually a finite size and present an internal structure determined by quarks and gluons. The nucleon radius, inferred from the proton charge distribution, turns out to be $\langle r_{\rm ch}^2 \rangle^{1/2} = 0.887 \pm 0.012$ fm [25].

There is a negligible overlap between the charge-density profiles of two protons if they are separated by a distance of $r \sim 1$ fm [8, 25]. For $r \lesssim 1$ fm, the larger overlap suggests that the NMBT description may be inadequate. However, there is experimental evidence indicating that, even in this scenario, the nucleon inner quark structure is poorly affected. These hints come from the observation of y-scaling in experiments of electron scattering off various nuclei targets. It shows that the beam particles can couple to nucleons carrying momenta up to ~ 700 MeV [8, 26].

1.2.1 Empirical facts on nuclear forces

Some key features of the NN interaction can be inferred by examining empirical data of atomic nuclei, without strict considerations about the underlying potential formalism.

- The *saturation of nuclear densities*, as mentioned in Section 1.1, indicates that the NN potential is stongly repulsive at short distances, that is

$$v(|\mathbf{r}|) > 0, \quad |\mathbf{r}| < r_c, \tag{1.15}$$

  where r_c denotes the radius of the repulsive core.

- The binding energy per nucleon is nearly constant for all nuclei with $A \geq 20$, indicating that nuclear forces have finite range r_0, i.e.

$$v(|\mathbf{r}|) = 0, \quad |\mathbf{r}| > r_0. \tag{1.16}$$

- Comparing the spectra of nuclei with the same A and charges differing by one unit, i.e. *mirror nuclei*, reveals similar nuclear interactions between protons and neutrons. The energies of levels with the same parity and angular momentum are essentially identical, with minor electromagnetic corrections. Therefore, this suggests that nuclear forces are *charge symmetric*.

Actually, charge symmetry is the manifestation of a more general property of nuclear forces, namely *isotopic invariance*. If we neglect the 0.1% mass difference, proton and neutron can be interpreted as two states of the same particle, the nucleon, that defines one or the other by specifying the isospin.

The Dirac equation can be used to describe a nucleon in vacuum, being obtained from the Lagrangian density

$$\mathcal{L} = \bar{\psi}_N(i\partial\!\!\!/ - m)\psi_N \tag{1.17}$$

where

$$\psi_N = \begin{pmatrix} \psi_p \\ \psi_n \end{pmatrix}, \tag{1.18}$$

with ψ_p and ψ_n being the four-spinors associated with the proton and the neutron, respectively. Also, $\partial\!\!\!/ = \gamma_\mu \partial^\mu$, where γ_μ denotes a Dirac gamma matrix, and $m \approx 939$ MeV is the nucleon mass.

The Lagrangian density (1.17) is invariant under the $SU(2)$ global phase transformation

$$U = e^{i\alpha_j \tau_j}, \tag{1.19}$$

where α_j $(j = 1, 2, 3)$ are constants, independent of the coordinate x, and the τ_j are Pauli matrices acting in isospin space. The commutation properties of Pauli matrices can be found in A.

From the above equations, we can see that the nucleon is represented by an isospin doublet, where the proton and the neutron correspond to isospin projections $+1/2$ and $-1/2$, respectively. Proton-proton and neutron-neutron pairs always have total isospin $T = 1$, whereas a proton-neutron pair may have either $T = 0$ or $T = 1$. We can write the isospin states in the same fashion as we usually expand the spin states in the basis of total spin. Therefore,

$$\begin{aligned} |00\rangle &= \frac{1}{\sqrt{2}}(|pn\rangle - |np\rangle), \\ |10\rangle &= \frac{1}{\sqrt{2}}(|pn\rangle + |np\rangle), \\ |1-1\rangle &= |nn\rangle\,, \\ |11\rangle &= |pp\rangle\,. \end{aligned} \tag{1.20}$$

Isospin invariance implies that the interaction between two nucleons separated by a distance $r = |\mathbf{r}_1 - \mathbf{r}_2|$ and having total spin S does not depend on the projection T_3, only on their total isospin T. For example, the potential $v(r)$ acting between two protons, or two neutrons, with spins coupled to $S = 0$ is the same as the potential acting between a proton and a neutron with spins and isospins coupled to $S = 0$ and $T = 1$.

We can also infer important information about the NN interaction through the observation of two-nucleon systems. There is only one observed nucleon-nucleon (NN) bound state in nature, namely deuterium (or deuteron) ^{2}H, consisting of a

proton and a neutron with total spin and isospin $S = 1$ and $T = 0$, respectively. This is a clear indication that nuclear forces are strongly *spin-isospin dependent*. Also, the deuteron has a non vanishing electric quadrupole moment, thus it possesses a non spherically symmetric charge distribution. This is a substantial evidence that NN forces are *non central*.

Apart from the NN bound state, there is a large database of phase shifts measured in proton-proton and proton-neutron scattering experiments (the Nijmegen database [27] includes ~ 4000 data points at beam energies up to 350 MeV in the lab frame). It has been extensively used to probe and constrain models of nuclear dynamics.

1.2.2 Two-nucleon potentials

A theoretical description of the NN interaction based on the formalism of quantum field theory was first attempted by Yukawa in 1935 [28]. In his work, Yukawa made the hypothesis that nucleons interact through the exchange of a particle whose mass, μ, can be deduced from the interaction range, r_0, that is

$$r_0 \sim \frac{1}{\mu}. \tag{1.21}$$

For $r_0 \sim 1$ fm, one finds $\mu \sim 200$ MeV ($1\ \text{fm}^{-1} = 197.3$ MeV).

Yukawa's idea led to the identification of the π-meson, or pion, as the exchanged particle with mass $m_\pi \sim 140$ MeV. The simplest π-nucleon coupling compatible with the observation that nuclear interactions conserve parity has the pseudoscalar form $ig\gamma^5\boldsymbol{\tau}$, where g is a coupling constant, and τ describes the nucleon isospin. The interaction Lagrangian can be written as

$$\mathcal{L}_I = -ig\bar{\psi}_N\gamma^5\tau^j\psi_N\pi^j, \tag{1.22}$$

where

$$\begin{aligned}\pi^1 &= \frac{1}{\sqrt{2}}(\pi^+ + \pi^-),\\ \pi^2 &= \frac{i}{\sqrt{2}}(\pi^+ - \pi^-),\\ \pi^3 &= \pi^0,\end{aligned} \tag{1.23}$$

with π^+, π^0, and π^- representing the three charge states associated with isospin projections $T_3 = +1,\ 0$, and -1, respectively. From the Lagrangian (1.22), it is possible to extract the corresponding invariant amplitude of the process depicted in Fig. 1.2. Taking the non-relativistic limit, it is possible to extract the so-called one-pion-exchange potential (OPEP) in momentum and coordinate spaces. In the former, we get

$$\tilde{v}_\pi(\boldsymbol{k}) = -\Big(\frac{f}{m_\pi}\Big)^2(\boldsymbol{\tau}_1\cdot\boldsymbol{\tau}_2)\frac{(\boldsymbol{\sigma}_1\cdot\boldsymbol{k})(\boldsymbol{\sigma}_2\cdot\boldsymbol{k})}{|\boldsymbol{k}|^2 + m_\pi^2}, \tag{1.24}$$

where $f^2 = g^2m_\pi^2/4m^2$, and

$$(\boldsymbol{\tau}_1\cdot\boldsymbol{\tau}_2) = (\eta_2'\boldsymbol{\tau}\eta_2)\cdot(\eta_1'\boldsymbol{\tau}\eta_1), \tag{1.25}$$

with η_i being the two-component Pauli spinor describing the isospin state of nucleon i. Also, the exchanged momentum is $k = p_1' - p_1 = p_2 - p_2' = (k_0, \mathbf{k})$.

Fourier transforming Eq. (1.24), we get the coordinate space representation

$$v_\pi(\boldsymbol{r}) = \frac{1}{3}\frac{1}{4\pi} f^2 m_\pi (\boldsymbol{\tau}_1 \cdot \boldsymbol{\tau}_2)\Big[T_\pi(r) S_{12}(\mathbf{r}) + \Big(Y_\pi(r) - \frac{4\pi}{m_\pi^3}\delta(\boldsymbol{r})\Big)(\boldsymbol{\sigma}_1 \cdot \boldsymbol{\sigma}_2)\Big], \quad (1.26)$$

where

$$S_{12}(\mathbf{r}) = \frac{3}{r^2}(\boldsymbol{\sigma}_1 \cdot \boldsymbol{r})(\boldsymbol{\sigma}_2 \cdot \boldsymbol{r}) - (\boldsymbol{\sigma}_1 \cdot \boldsymbol{\sigma}_2), \quad (1.27)$$

$$Y_\pi(r) = \frac{e^{-m_\pi r}}{m_\pi r}, \quad (1.28)$$

$$T_\pi(r) = \Big(1 + \frac{3}{m_\pi r} + \frac{3}{m_\pi^2 r^2}\Big) Y_\pi(r). \quad (1.29)$$

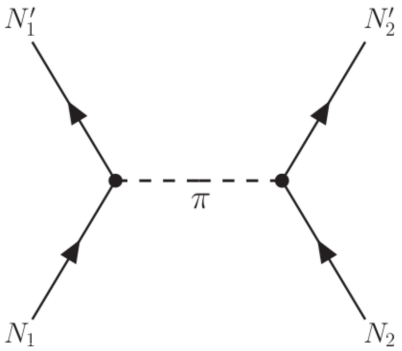

Figure 1.2. Feynman diagram describing the one-pion-exchange process in NN scattering.

For $g^2/4\pi \approx 14$, this expression provides a reliable description of the long range part of the NN interaction, corresponding to $|\mathbf{r}| > 1.5$ fm. At medium and short range, more complex processes should be taken into account in order to reliably describe the NN interaction. As mentioned before, one should, in principle, use QCD to describe them.

Recent advancements in studies focused on extracting the NN potential from lattice QCD calculations have shown noteworthy progress in predicting its essential characteristics. Nonetheless, when applying a lattice QCD potential to nuclear matter calculations, the outcomes indicate the necessity for substantial improvements to achieve the level essential for a comprehensive quantitative explanation of empirical data [29].

Phenomenological potentials can be generally written in the form

$$v = v_\pi + v_R \quad (1.30)$$

where v_π represents OPEP stripped of the δ-function contribution and v_R the interactions at medium and short range. A convenient way of writing phenomenological potentials in coordinate space is given by

$$v_{ij} = \sum_p v^p(r_{ij}) O_{ij}^p \ , \quad (1.31)$$

where the functions v^p only depend on the interparticle distance r_{ij}. The sum in Eq. (1.31) includes up to 18 terms with the corresponding operators, O^p_{ij} describing the strong spin-isospin dependence and noncentral nature of nuclear forces, as well as the occurrence spin-orbit interactions and small violations of charge symmetry and charge independence.

The most important contributions come from the first six operators

$$O^{p\leq 6}_{ij} = 1,\ (\boldsymbol{\tau}_1 \cdot \boldsymbol{\tau}_2),\ (\boldsymbol{\sigma}_1 \cdot \boldsymbol{\sigma}_2),\ (\boldsymbol{\sigma}_1 \cdot \boldsymbol{\sigma}_2)(\boldsymbol{\tau}_1 \cdot \boldsymbol{\tau}_2), S_{12},\ S_{12}(\boldsymbol{\tau}_1 \cdot \boldsymbol{\tau}_2). \tag{1.32}$$

The potential models obtained including the six operatorsof Eq. (1.32) explain deuteron properties and the S-wave scattering phase shifts up to pion production threshold. In order to describe the P wave, one has to include two additional components involving the momentum-dependent operators

$$O^{p=7,8}_{ij} = (\boldsymbol{\ell} \cdot \mathbf{S}) \otimes (1, (\boldsymbol{\tau}_i \cdot \boldsymbol{\tau}_j)) \tag{1.33}$$

where $\boldsymbol{\ell}_{ij}$ denotes the relative angular momentum of the interacting pair,

$$\boldsymbol{\ell}_{ij} = \frac{1}{2i}(\mathbf{r}_i - \mathbf{r}_j) \times (\boldsymbol{\nabla}_i - \boldsymbol{\nabla}_j), \tag{1.34}$$

and $\mathbf{S}_{ij}$ its total spin

$$\mathbf{S}_{ij} = \frac{1}{2}(\boldsymbol{\sigma}_i + \boldsymbol{\sigma}_j). \tag{1.35}$$

The operators corresponding to $p = 7, ..., 14$ are associated with the nonstatic components of the NN interaction, while those corresponding to $p = 15, ..., 18$ account for small violations of charge symmetry. All these terms are included in the state-of-the-art Argonne v_{18} (AV18) potential [30]. The definition of the AV18 potential involves 40 parameters, the values of which are adjusted in such a way as to reproduce the properties of deuterium, as well as the phase-shifts obtained from the measured NN cross sections. It fits the 4301 phase shifts collected in the Nijmegen database with a reduced χ-square of 1.09.

Besides the representation (1.31), we can also write the NN potential in the total spin-isospin representation, that is

$$v = \sum_{p=1}^{6} v^p_{ij} O^p = \sum_{TS} [v_{TS} + \delta_{S1} v_{tT} S_{12}] P_{2S+1} \Pi_{2T+1} \tag{1.36}$$

where the spin projectors are defined, respectively, as

$$P_{S=0} = P_1 = \frac{1 - (\boldsymbol{\sigma}_1 \cdot \boldsymbol{\sigma}_2)}{4}, \tag{1.37}$$

$$P_{S=1} = P_3 = \frac{3 + (\boldsymbol{\sigma}_1 \cdot \boldsymbol{\sigma}_2)}{4}. \tag{1.38}$$

The isospin projectors Π_1 and Π_3 are the defined in the same way, with the spin Pauli matrices substituted by the isospin Pauli matrices. The conversion between the two representations is given in Appendix A.

The results reported in this Thesis have been obtained using the Argonne v_6' (AV6P) potential, which is a reprojection of the full AV18 onto the basis of the six operators (1.32) [31]. It has been designed for easier use in many-body calculations and yields solid results. It reproduces the deuteron binding energy and electric quadrupole moment with accuracy of 1% and 5%, respectively, and provides an excellent fit of the phase shifts in the $^1S_0$ channel, corresponding to $T = 1$, $S = 0$ and angular momentum $\ell = 0$. This can be seen in Fig. 1 of Ref. [32].

In general, phenomenological potential models are capable provide an accurate description of NN scattering in vacuum by construction. However, their use to describe collisions in dense matter deserves thorough consideration. It has to be kept in mind that in strongly degenerate fermion systems, such as cold nuclear matter and relevant to NS physics, only nucleons with momentum close to the Fermi momentum k_F can participate in scattering processes. The latter is trivially related to matter density through $k_F = (6\pi^2\varrho/\nu)^{1/3}$, hence a simple relation can be established between the energy of the projectile particle in the laboratory frame and the matter density. In the case of head-on collisions,

$$E_{\text{lab}} = 4E_F = \frac{2}{m}(6\pi^2\frac{\varrho}{\nu})^{2/3} \tag{1.39}$$

The above equation suggests that phenomenological potentials can be reliably used to describe nuclear matter up to a density determined by the upper limit of the energy range in which they accurately reproduce NN scattering data. For example, the AV18 and AV6P models, which provide an excellent fit of the phase shifts at energy as high as 600 MeV, are expected to be adequate up to densities $\varrho \gtrsim 4\varrho_0$ [8, 32].

1.2.3 Three-nucleon potentials

The inclusion of three-nucleon (NNN) potentials in the Hamiltonian (1.14) is needed to explain the ground-state energy of the NNN bound states, the nuclei ^{3}H and ^{3}He, whose values can be computed exactly using deterministic techniques. In a broader sense, adding a three-body force to the dynamics is a way of describing the interactions of composite systems without explicitly considering their internal structure. A notable example is the system involving the Earth, the Moon and a satellite orbiting the Earth.

In the seminal paper of Fujita and Miyazawa [33], they suggest that the most prominent mechanism collaborating to NNN forces is the process where two pions are exchanged among nucleons and a Δ resonance (with $M_\Delta \approx 1232$ MeV) is excited in the intermediate state, as shown in Fig. 1.3.

Phenomenological NNN potentials can be generally written as

$$V_{ijk} = V_{ijk}^{2\pi} + V_{ijk}^{R}, \tag{1.40}$$

where $V_{ijk}^{2\pi}$ is the attractive Fujita-Miyazawa term and V_{ijk}^{R} is a purely phenomenological repulsive term. The coupling constant of the first term is adjusted to correctly reproduce the binding energy of ^{3}H and ^{3}He, while the one associated to the repulsive term is tuned to obtain the correct value of the SNM equilibrium density ϱ_0.

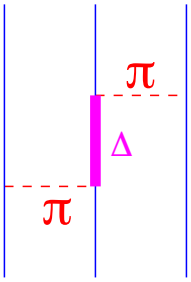

Figure 1.3. Diagram representing the Fujita-Miyazawa NNN interaction.

In this Thesis, we use the Urbana IX (UIX) NNN potential [34, 35]. Recent studies of the EOS of cold neutron matter—performed by Lovato *et al.* [36] using state-of-the-art computational techniques—show that the predictions of the somewhat simplified AV6P+UIX Hamiltonian are very close to those obtained from the full AV18+UIX model, providing the basis of the widely employed EOS of Akmal, Pandharipande and Ravenhall [37].

In order to illustrate the predictive power of using an NN+NNN dynamics, we show in Fig. 1.4 the results of Green's Function Monte Carlo (GFMC) calculations of ground and low-lying excited states, performed by Wiringa *et al.* [38], for atomic nuclei with $A \leq 8$. Such results were obtained by using AV18 as the NN potential and UIX as the NNN potential. We can see that including an NNN potential substantially improves the agreement with the experimental data.

1.3 Chiral potentials

Over the past two decades, significant attention has been directed towards formulating nuclear potentials using Chiral Effective Field Theory (χEFT) (refer to, e.g., Ref. [39] and [40], and references therein). Initially proposed by Weinberg [41], this formalism relies on effective Lagrangians that incorporate pions and low-momentum nucleons, constrained by the broken chiral symmetry of strong interactions. The approach establishes a structured method wherein the nuclear interaction is systematically expanded in terms of a small parameter, such as the ratio involving the pion mass or the nucleon momentum, and the scale of chiral symmetry breaking, $\Lambda_\chi \sim 1$ GeV. It provides an efficient way of consistently extracting two-, three-, and many-nucleon potentials.

The initial χEFT potentials were initially formulated in momentum space, given that they are based on a momentum expansion [39, 40]. Nevertheless, a method has also been developed to acquire representations in coordinate space, needed for use in QMC calculations [42, 43]. The results of an investigation conducted utilizing the Auxiliary Field Diffusion Monte Carlo (AFDMC) technique reveal that local coordinate-space $\mathrm{N^2LO}$ potentials, characterizing both two- and three-nucleon interactions, deliver a notably accurate description of the ground-state energies and charge radii of nuclei with $A \leq 16$ [44].

The most noteworthy feature of χEFT is the mechanism of carrying out two-

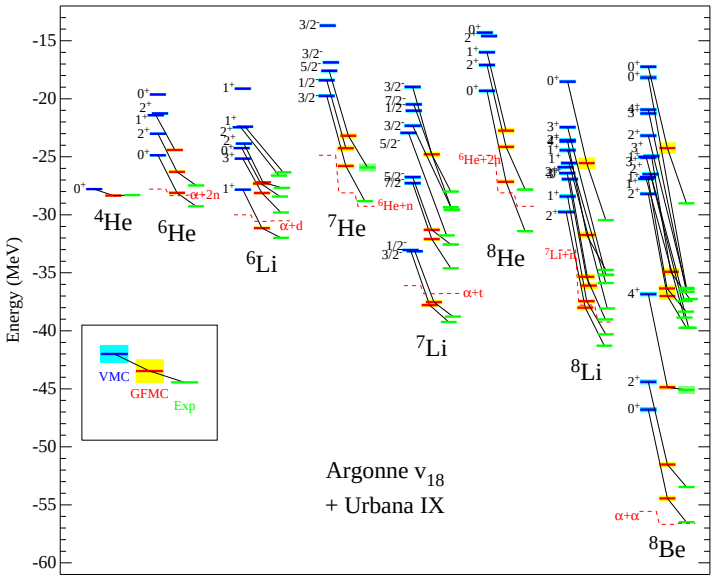

Figure 1.4. Comparison between the spectra of light nuclei obtained by the authors of Ref. [38] using the Green's Function Monte Carlo (GFMC) technique and experimental data. The nuclear Hamiltonian utilised in the calculation comprised the AV18 NN potential and the UIX NNN potential.

and many-nucleon interaction potentials in a fully consistent fashion, alongside the leverage of adding higher order terms with the estimate of theoretical uncertainty. In the context of NS physics, it has been widely applied in studies of NS structure [45–53]. We must remember, however, that χEFT is based on a low momentum expansion, hence it is inherently limited when describing nuclear interactions in high-density nuclear matter. In the phase-shift analysis of Piarulli *et al.* [54], we see that chiral potentials provide an accurate fit to the data up to $E_{\text{lab}} \lesssim 200$ MeV, therefore up to $\sim 2\varrho_0$, according to the reasoning of Sect. 1.2.2. Given that NS matter is expected to reach densities higher than $2\varrho_0$, the applicability of such chiral potentials does not span over the full relevant density regime and purely phenomenological potentials such as AV18 or AV6P seem a more solid option. It is worth mentioning, nonetheless, that some works combined astrophysical data and χEFT constraints in order to constrain the NS EOS at $\varrho \geq 2\varrho_0$ [55–58].

1.4 Relativistic approaches

The theoretical framework we have been discussing so far is non-relativistic, being remarkably successful at describing atomic nuclei and a large variety of nuclear matter properties. As the matter density increases, the relativistic propagation of the nucleons, as well as the retarded propagation of the virtual meson fields giving rise to nuclear forces, are expected to become more and more significant. It is known that NMBT-based EOSs violate causality at very high densities [59], thus being inconsistent in this regime. We can estimate the importance of including relativistic corrections through the ratio k^2/m^2 that would appear in the series expansion of

the relativistic dispersion relation. In degenerate matter, we have $k \sim k_F$, thus

$$\frac{k_F^2}{m^2} = \Big(\frac{6\pi^2 \varrho}{\nu m^3}\Big)^{2/3}. \tag{1.41}$$

In the density range $\varrho_0 - 4\varrho_0$, relevant to neutron stars, we get $k_F^2/m^2 \sim 0.1 - 0.3$. In the extreme limit of having $k_F^2/m^2 \approx 1$, we would have a corresponding density of $40\varrho_0$, way beyond the regime present in an NS core.

The theoretical approaches discussed so far are based on the assumptions that the degrees of freedom associated with the carriers of the interaction between nucleons can be eliminated in favour of potentials. QCD, on the other hand, is a relativistic quantum field theory and satisfies all relativistic constraints by construction. However, as mentioned before, we are still not able to use it to impose strong constraints on the behaviour of nuclear matter in the non-perturbative regime.

In this section, we briefly discuss two different relativistic approaches to circumvent these problems: boost corrections to the nuclear Hamiltonian and relativistic mean field (RMF) models.

1.4.1 Boost corrections

The relativistic Hamiltonian is the sum of relativistic nucleon kinetic energies and two- and three-body potentials, properly corrected to account for relativistic effects. We can write

$$H_R = \sum_i \sqrt{m_i^2 + k_i^2} + \sum_{j>i} [\tilde{v}_{ij} + \delta v_{ij}(\mathbf{K}_{ij})] + \sum_{k>j>i} [\tilde{V}_{ijk} + \delta V_{ijk}(\mathbf{K}_{ijk})] \tag{1.42}$$

where $\tilde{v}_{ij}$ and $\tilde{V}_{ijk}$ label two- and three-body potentials in the rest frame of the interacting particles. In this frame, we have

$$\mathbf{K}_{ij} = \mathbf{k}_i + \mathbf{k}_j = 0, \tag{1.43}$$

$$\mathbf{K}_{ijk} = \mathbf{k}_i + \mathbf{k}_j + \mathbf{k}_k = 0. \tag{1.44}$$

In Eq. (1.42), the terms δv_{ij} and δV_{ijk} are called boost corrections to the NN and NNN potentials, respectively. They are related to the motion of the center of mass of the interacting particles [60].

The potentials are determined in the center-of-mass frame of the interacting particles, and, if the center-of-mass is at rest, $\delta v_{ij} = \delta V_{ijk} = 0$. However, in the presence of the nuclear medium, the center-of-mass is not at rest, therefore boost corrections should be added to the dynamics in order to account for its motion.

The leading boost corrections arise from the static part of the NN potential, v_{ij}^s, and can be written [37, 60]

$$\delta v_{ij}(\mathbf{K}, \mathbf{r}) = -\frac{K^2}{8m^2} v_{ij}^s(\mathbf{r}) + \frac{(\mathbf{K} \cdot \mathbf{r})}{8m^2} \mathbf{K} \cdot \nabla v_{ij}^s(\mathbf{r}). \tag{1.45}$$

Inclusion of the boost correction results in the appearance of a sizable repulsive contribution to the potential energy associated with the NN potential and to a corresponding reduction of the repulsion arising from the NNN potential. Indeed, a

fit to the two- and three-nucleon data and the empirical properties of SNM with the Hamiltonian

$$H_R = \sum_i \frac{\mathbf{k}_i^2}{2m} + \sum_{j>i}[v_{ij} + \delta v_{ij}] + \sum_{k>j>i} V_{ijk}^* \tag{1.46}$$

shows that the repulsive contribution to the boost corrected NNN potential V_{ijk}^* is reduced by about 30% with respect to the non-relativistic counterpart [37].

Including boost corrections obviously alleviates the issue of causality violation, pushing the superluminal threshold to larger values of density [37]. Actually, this is a natural result coming from the softening of the EOS, which also causes the maximum mass of NSs to be reduced by $\sim 10\%$.

1.4.2 Relativistic Mean Field Models

Within the model first proposed by J. Walecka in the 1970s, nuclear matter consists of nucleons, described by Dirac spinors, interacting through exchange of a scalar and a vector meson, called σ and ω, reminiscent of the mesons employed in the derivation of one-boson-exchange potentials [61].

A general Lagrangian density can be written as

$$\mathcal{L} = \mathcal{L}_N + \mathcal{L}_B + \mathcal{L}_{int}, \tag{1.47}$$

where $\mathcal{L}_N$, $\mathcal{L}_B$ and $\mathcal{L}_{int}$ describe free nucleons, mesons and their interactions, respectively.

The dynamics of the free nucleon field is dictated by the Dirac Lagrangian

$$\mathcal{L}_N(x) = \bar{\psi}(x)(i\partial\!\!\!/ - m)\psi(x), \tag{1.48}$$

where the nucleon field, denoted by $\psi(x)$ combines the two four-component Dirac spinors describing the proton and the neutron. The meson Lagrangian reads

$$\mathcal{L}_B(x) = -\frac{1}{4}F^{\mu\nu}(x)F_{\mu\nu}(x) + \frac{1}{2}m_\omega^2 V_\mu(x)V^\mu(x) + \frac{1}{2}\partial_\mu\phi(x)\partial^\mu\phi(x) - \frac{1}{2}m_\sigma^2\phi(x)^2, \tag{1.49}$$

where

$$F_{\mu\nu}(x) = \partial_\mu V_\nu(x) - \partial_\nu V_\mu(x), \tag{1.50}$$

$V_\mu(x)$, and $\phi(x)$ are the vector and scalar meson fields, respectively, with the corresponding masses m_ω and m_σ.

In specifying the form of the interaction Lagrangian, it is required that, besides being a Lorentz scalar, $\mathcal{L}_{int}$ gives rise to a Yukawa-like meson exchange potential in the static limit. Hence,

$$\mathcal{L}_{int}(x) = g_\sigma\phi(x)\bar{\psi}(x)\psi(x) - g_\omega V_\mu(x)\bar{\psi}(x)\gamma^\mu\psi(x), \tag{1.51}$$

where g_σ and g_ω are coupling constants and the choice of signs reflect the fact that the NN interaction contains both attractive and repulsive contributions. The equations of motion extracted from these Lagrangians are

$$(\Box + m_\sigma^2)\phi(x) = g_\sigma \bar{\psi}(x)\psi(x), \tag{1.52}$$

$$(\Box + m_\omega^2)V_\mu(x) - \partial_\mu(\partial^\nu V_\nu(x)) = g_\omega \bar{\psi}(x)\gamma_\mu\psi(x), \tag{1.53}$$

$$[(\not{\partial} - g_\omega \gamma_\mu V^\mu(x)) - (m - g_\sigma \phi(x))]\psi(x) = 0, \tag{1.54}$$

which are fully relativistic and Lorentz covariant. However, their solution involves prohibitive difficulties, that can not be circumvented using approximations based on perturbation theory. A technique known as *relativistic mean field* (RMF) approximation consists essentially of treating $\phi(x)$ and $V_\mu(x)$ as classical fields.

The meson fields are replaced by their mean values in the ground state of uniform nuclear matter

$$\phi(x) \to \langle\phi(x)\rangle, \quad V_\mu(x) \to \langle V_\mu(x)\rangle, \tag{1.55}$$

where $\langle\phi(x)\rangle$ and $\langle V_\mu(x)\rangle$ must be computed from the equations of motion. The nuclear matter EOS can then be obtained in closed form, and the meson masses and coupling constants appearing in the Lagrangian density can be determined by fitting the empirical properties of SNM, that is, the binding energy, equilibrium density, and compressibility.

The Walecka model, as the most basic implementation of the RMF approximation, has been extended in various studies and widely utilised for the examination of NS properties. It is important to highlight, however, that although it is suitable for describing matter in the $\varrho \to \infty$ limit, its application at finite densities relies on the assumption that the Compton wavelengths of the exchanged mesons are significantly larger than the typical separation distance between nucleons. In the case of heavy mesons, the validity of this assumption may be questionable and should be carefully investigated.

Chapter 2

Nuclear Matter theory

The interpretation of the presently available and future astronomical data providing information on the post merger phase of coalescing binary neutron stars will require an accurate description of the properties of dense nuclear matter at temperatures as high as 100 MeV [62–66]. Of great importance, in this context, will be the development of a consistent framework suitable for modelling both the equilibrium configurations—determining the equation of state (EOS) of NS matter—and dissipative processes, involving mechanisms that lead to the appearance of bulk viscosity [67] and neutrino emission [68].

The EOS of hot nuclear matter is often derived from dynamical models based on the independent-particle approximation, using Skyrme-type effective interactions [69] or the formalism of quantum field theory and the RMF approximation [70]. More comprehensive studies have also been performed within the framework of Nuclear Many-Body Theory. Calculations along this line have been carried out using both G-matrix perturbation theory and the variational approach based on the formalism of correlated wave functions and the cluster expansion technique; see, e.g., Refs. [71, 72].

The authors of Refs. [73] have developed a procedure to renormalise the coordinate-space nuclear Hamiltonian by introducing screening effects arising from short-range nucleon-nucleon correlations. The resulting density-dependent effective potential—which includes the contributions of both two- and three-nucleon forces—is well-behaved, and can be employed to carry out perturbative calculations in the basis of eigenstates of the non interacting system. The extension of this formalism to the case of non-zero temperature—involving a proper definition of the gran canonical potential needed to achieve thermodynamic consistency—is based on the assumption that at temperature $T \ll m_\pi$, $m_\pi \approx 150$ MeV being the mass of the π-meson, thermal effects do not significantly affect strong-interaction dynamics [32].

In this chapter, we discuss the main features of the approach of Refs. [32, 73], as well as its application to a variety of equilibrium and dynamical properties of nuclear matter [74, 75]. This will pave the way for the results presented in the following chapters. In the last section, we also examine the possibility of using simple approximated procedures to parameterise deviations from the zero-temperature EOS associated with thermal effects.

2.1 Correlated Basis Functions and cluster expansion techniques

The primary objective of nuclear matter theory is to establish a comprehensive framework capable of making predictions for systems with any number of constituents, from the deuteron to neutron stars. In other words, it means solving the quantum-mechanical many-body problem

$$H\,|\Psi_n\rangle = E_n\,|\Psi_n\rangle \tag{2.1}$$

where H is the Hamiltonian (1.14), $|\Psi_n\rangle$ the many-particle state with energy level n.

As discussed before, the NN interaction is strongly repulsive at short distances, rendering standard perturbation theory not suitable to carry out calculations of nuclear matter properties. The first theoretical approach with the goal of overcoming this problem was proposed by K. Brueckner in the 1950s, the so-called G-matrix perturbation theory. It is based on the replacement of the bare NN potential with a well-behaved operator describing NN scattering in the nuclear medium. The lowest-order approximation of the resulting expansion has been widely utilized in early investigations of cold nuclear matter (see, e.g., Refs. [76, 77]). Recent advancements, which incorporate higher-order terms and address the matter at finite temperature, can be found in Refs. [78–80].

Another possibility of tackling the many-body problem is taking advantage of the variational principle associated with the Schrödinger equation. The variational approach to the many-body problem with strong forces was first proposed by Jastrow [81]. Within this scheme, the normalised trial ground-state wave function of the Hamiltonian (1.14) is written in the form

$$|\Psi_T\rangle = \frac{\mathcal{F}\,|\Phi_0\rangle}{\langle\Phi_0|\mathcal{F}^\dagger\mathcal{F}|\Phi_0\rangle^{1/2}}, \tag{2.2}$$

where $|\Phi_0\rangle$ denotes the Fermi gas ground state, given by the (normalised) Slater determinant

$$|\Phi_0\rangle = \frac{1}{\sqrt{A!}}\det\begin{bmatrix} \phi_{n_1}(x_1) & \phi_{n_1}(x_2) & \dots & \phi_{n_1}(x_A) \\ \phi_{n_2}(x_1) & \phi_{n_2}(x_2) & \dots & \phi_{n_2}(x_A) \\ \vdots & \ddots & \vdots & \vdots \\ \phi_{n_A}(x_1) & \phi_{n_A}(x_2) & \dots & \phi_{n_A}(x_A) \end{bmatrix}. \tag{2.3}$$

Note that the levels $n_1, \dots, n_A$ indicate orbitals consisting of spin, isospin and momentum. Here, the single-particle wavefunctions are given by

$$\phi_{n_a}(x_i) = \frac{1}{\sqrt{V}} e^{i\mathbf{k}_{a_i}\cdot\mathbf{r}_i}\chi^a(i)\eta^a(i), \tag{2.4}$$

where $\chi^a(i)$ and $\eta^a(i)$ label, respectively, the spinor and isospinor of particle i in the a-th spin-isospin-orbital, while $(x_1 \dots x_A)$ collect all the degrees of freedom of such a quantum wavefunction, both continuous and discrete (position, spin and isospin). Note that the integrations to be carried out in x_i are of the form

$$\int dx_i \equiv \mathrm{Tr}_i \int d\mathbf{r}_i. \tag{2.5}$$

The A-body operator F, describing the effects of correlations among nucleons, is written as a product of two-body operators, whose structure mirrors the form of the NN potential discussed in Chapter 1. The resulting expression (see Eq. (1.31)) is

$$\mathcal{F} = \mathcal{S} \prod_{i<j} F_{ij} \tag{2.6}$$

with

$$F_{ij} = \sum_p f^p(r_{ij}) O^p_{ij}. \tag{2.7}$$

It is worth mentioning that the symmetrisation operator $\mathcal{S}$ is needed in order to fulfill the requirement of antisymmetry of $|\Psi_T\rangle$ under particle exchange, given that $|\Phi_0\rangle$ is antisymmetric but, in general, $[O^p_{ij}, O^q_{jk}] \neq 0$.

The radial dependence of the *correlation functions* $f^p(r_{ij})$ is determined by minimising the expectation value of the Hamiltonian in the correlated ground state

$$E_V = \langle \Psi_T | H | \Psi_T \rangle \geq E_0, \tag{2.8}$$

that is, by imposing the conditions

$$\frac{\delta E_V}{\delta f^p} = 0. \tag{2.9}$$

Our work has been carried out using the so-called Correlated Basis Functions (CBF) theory. Being a natural extension of the variational approach, CBF perturbation theory is based on the assumption that the correlation operator F, determined from the above mentioned minimisation, can be used to build the complete set of correlated states [82, 83]

$$|\Psi_n\rangle \equiv \frac{\mathcal{F}\,|\Phi_n\rangle}{\langle \Phi_n | \mathcal{F}^\dagger \mathcal{F} | \Phi_n \rangle^{1/2}} \tag{2.10}$$

where $|\Phi_n\rangle$ is an n-particle n-hole state of the non interacting Fermi gas. Note that the correlated states defined by (2.10) are not orthogonal to one another, that is,

$$\langle \Psi_n | \Psi_m \rangle = \delta_{nm} + S_{nm}, \tag{2.11}$$

with $S_{nm} \neq 0$. The correlated states can be orthogonalised using standard methods of many-body theory [8]. However, the studies discussed in this Thesis are unaffected by corrections arising from non orthogonality.

Within the CBF scheme, the expectation values

$$E^V_n = \langle \Psi_n | H | \Psi_n \rangle \tag{2.12}$$

provide the lowest order approximation to the energy of the state $|\Psi_n)$.

The perturbative expansion is based on the decomposition

$$H = H_0 + H_1, \tag{2.13}$$

where H_0 and H_1 are defined in terms of their matrix elements in the correlated basis, by singling out the diagonal and off-diagonal contributions. The resulting expressions are

$$\langle \Psi_m | H_0 | \Psi_n \rangle = \delta_{mn} \langle \Psi_m | H | \Psi_n \rangle = \delta_{mn} E_n^V, \tag{2.14}$$

$$\langle \Psi_m | H_1 | \Psi_n \rangle = (1 - \delta_{mn}) \langle \Psi_m | H | \Psi_n \rangle. \tag{2.15}$$

If the correlation operator F is properly chosen, so that E_0^V is close to the ground-state energy E_0, the correlated states have large overlaps with the eigenstates of H, and the matrix elements of H_1 are small. As a consequence, a perturbative expansion in powers of H_1 is rapidly convergent.

In principle, CBF perturbation theory provides a consistent and systematic framework to improve the quality of variational calculations, as well as to perform accurate calculations of nuclear matter properties other than the ground-state energy. However, numerical implementation of the CBF formalism requires the calculation of matrix elements involving non-orthogonal correlated states, which entail non-trivial difficulties.

An efficient way to overcome this problem is the *cluster expansion technique*, reminiscent of the calculation of the partition function of classical liquids [84]. This approach enables the study of large and intricate many-body structures by breaking them down into more manageable (with fewer particles) components. Owing to the short range nature of correlations, the A-body operator F of Eq. (2.6) exhibits the cluster decomposition property. In other words, if any subset of m nucleons, labeled by the indices $i_1 ... i_m$, is moved from the rest, labelled by indices $i_{m+1} ... A$, F reduces to the factorised form

$$\mathcal{F}(1...A) = \mathcal{F}_m(i_1 ... i_m) \mathcal{F}_{A-m}(i_{m+1} ... i_A). \tag{2.16}$$

Note that we have $\mathcal{F}_1(i) \equiv 1$ and $\mathcal{F}_2(i,j) \equiv F_{ij}$, thus the two-nucleon correlation function satisfies the asymptotic condition

$$\lim_{r_{ij} \to \infty} F_{ij} = 1. \tag{2.17}$$

2.1.1 Cluster expansion

In the calculation of the expectation value of any many-body operator, it is convenient to perform separate cluster expansion for the numerator and the denominator, the latter arising from the normalization of CBF states

$$O_{mn} \equiv (\Phi_n | O | \Phi_m) \equiv \frac{\langle \Phi_n | \mathcal{F}^\dagger O \mathcal{F} | \Phi_m \rangle}{\langle \Phi n | \mathcal{F}^\dagger \mathcal{F} | \Phi_m \rangle} \equiv \frac{N_{nm}}{D_{nm}} \tag{2.18}$$

A general property of cluster expansions is the fact that divergent terms coming from the expansion and of the denominator cancel, so that the ratio N_{nm}/D_{nm} is finite.

When calculating energy expectation values as in Eq. 2.12, we deal only with diagonal matrix elements, i.e., with $n = m$. When dealing with operators that involve transitions from one state to another, non-diagonal matrix elements will be

present. In this section, we briefly discuss the $n = m$ scenario, which is relevant for the basic understanding of how the cluster expansion will work and for the calculation of the energy expectation value. When talking about the nuclear matter response function in Chapter 4, we come back to the non-diagonal elements.

In principle, the correlation operator F_{ij} should include all spin-isospin contributions and the contribution coming from three-body interactions. Nonetheless, the basic elements of the cluster expansion formalism are best illustrated considering the simplified Jastrow case, that is, neglecting NNN forces and assuming the correlations are purely scalar

$$\mathcal{F} = \prod_{j>i=1}^{A} f(r_{ij}), \tag{2.19}$$

with the function $f(r_{ij})$ being referred to as Jastrow correlation function. In this case, we have $\mathcal{F} = \mathcal{F}^\dagger$, and

$$\mathcal{F}^2 = \prod_{j>i=1}^{A} f^2(r_{ij}) = \prod_{j>i=1}^{A} [1 + h(r_{ij})], \tag{2.20}$$

where $h(r_{ij}) = f^2(r_{ij}) - 1$. From Eq. (2.17), we see that $h(r)$ is short-ranged and vanishes at large r, given that $f(r \geq d^c) = 1$. The variational parameter d^c is the *central healing distance* encompassing the fact that when two-particles are further apart than d^c they are not anymore correlated. Therefore, $h(r_{ij})$ can be treated as a smallness parameter for the cluster expansion.

Let us take the simplified Hamiltonian

$$H = T + V = \sum_i \frac{\mathbf{k}_i^2}{2m} + \sum_{i<j} v(\mathbf{r}_{ij}) \tag{2.21}$$

and compute the energy expectation value of the ground state

$$E_V = \langle \Psi_T | H | \Psi_T \rangle = \frac{\langle \Phi_0 | \mathcal{F}(T+V)\mathcal{F} | \Phi_0 \rangle}{\langle \Phi_0 | \mathcal{F}^2 | \Phi_0 \rangle} = \frac{\mathcal{N}}{\mathcal{D}}. \tag{2.22}$$

We will analyse the numerator and the denominator separately.

Cluster expansion of the denominator

We can write the denominator expansion as

$$\begin{aligned} \langle \Psi_T | \Psi_T \rangle &= \langle \Phi_0 | \prod_{j>i=1}^{A} [1 + h(r_{ij})] | \Phi_0 \rangle \\ &= \langle \Phi_0 | \Phi_0 \rangle + \sum_{i<j} \langle \Phi_0 | X^{(2)}(\mathbf{r}_i, \mathbf{r}_j) | \Phi_0 \rangle + \sum_{i<j<k} \langle \Phi_0 | X^{(3)}(\mathbf{r}_i, \mathbf{r}_j, \mathbf{r}_k) | \Phi_0 \rangle + \ldots, \end{aligned} \tag{2.23}$$

where $X^{(n)}$ represents the cluster involving n correlated particles. Due to the symmetry of the ground state Φ_0 under any two-particle exchange, we can factorise

the particles 1 and 2 out of the correlation parameters and write

$$\langle\Psi_T|\Psi_T\rangle = 1 + \binom{A}{2}\langle\Phi_0|X^{(2)}(\mathbf{r}_1,\mathbf{r}_2)|\Phi_0\rangle + \binom{A}{3}\langle\Phi_0|X^{(3)}(\mathbf{r}_1,\mathbf{r}_2,\mathbf{r}_3)|\Phi_0\rangle + \ldots, \tag{2.24}$$

with

$$X^{(2)}(\mathbf{r}_1,\mathbf{r}_2) = h(r_{12}), \tag{2.25}$$

$$X^{(3)}(\mathbf{r}_1,\mathbf{r}_2,\mathbf{r}_3) = h(r_{12})h(r_{13}) + h(r_{12})h(r_{23}) + h(r_{23})h(r_{13}) + h(r_{12})h(r_{13})h(r_{23}). \tag{2.26}$$

From the above expressions, we can use a diagrammatic representation for the expansion

$\mathcal{D} = 1 +$ 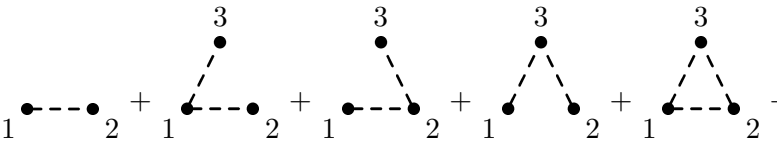 $+ \ldots$ (2.27)

We have started from the mathematical definition and then we have drawn these diagrams. It is also possible to follow this process in the opposite direction, i.e., to infer the cluster expansion from these pictorial representation [85, 86].

Cluster expansion of the numerator

For the numerator, we follow the same *modus operandi*. The difference now is the presence of an additional operator, the Hamiltonian. Let us start from the potential energy term, V

$$\mathcal{N} = \langle\Phi_0|\mathcal{F}V\mathcal{F}|\Phi_0\rangle = \sum_{i<j}\langle\Phi_0|\mathcal{F}v(\mathbf{r}_{ij})\mathcal{F}|\Phi_0\rangle = \frac{A(A-1)}{2}\langle\Phi_0|v(\mathbf{r}_{12})\mathcal{F}^2|\Phi_0\rangle\,. \tag{2.28}$$

Now the particles 1 and 2 also appear in $v(\mathbf{r}_{12})$. A clever way of using the symmetry of the ground state is factorising $f^2(r_{12})$ out of the correlation functions, such that

$$\mathcal{F}^2 = \prod_{i<j} f^2(r_{ij}) = f^2(r_{12}) \prod_{i<j\neq 1,2}[1 + h(r_{ij})], \tag{2.29}$$

and, therefore,

$$\mathcal{F}^2 = f^2(r_{12})\Big[1 + \sum_{i\neq 1,2} X^{(3)}(\mathbf{r}_1,\mathbf{r}_2;\mathbf{r}_i) + \sum_{i\neq 1,2} X^{(4)}(\mathbf{r}_1,\mathbf{r}_2;\mathbf{r}_i,\mathbf{r}_j) + \ldots\Big]. \tag{2.30}$$

We will call particles 1 and 2 as the *active particles*. Explicitly, the cluster contributions are

$$X^{(3)}(\mathbf{r}_1,\mathbf{r}_2;\mathbf{r}_i) = h(r_{1i}) + h(r_{2i}) + h(r_{1i})h(r_{2i}), \tag{2.31}$$

$$X^{(4)}(\mathbf{r}_1,\mathbf{r}_2;\mathbf{r}_i,\mathbf{r}_j) = h(r_{ij}) + h(r_{1i})h(r_{2j}) + h(r_{1i})h(r_{1j}) + h(r_{1i})h(r_{ij}) + h(r_{2i})h(r_{2j}) + h(r_{2i})h(r_{ij}) + h(r_{1i})h(r_{2j})h(r_{ij}) + \ldots \tag{2.32}$$

We could again draw a pictorial representation of the expansion

$\mathcal{N} =$ 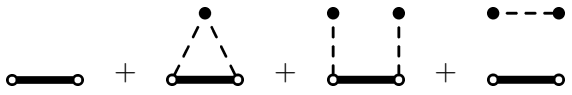 $+ \cdots ,$ (2.33)

where now the empty vertices represent the active particles, while the full vertices the background particles.

If one carries out the expansion with more terms, it is possible to see that

$\mathcal{N} =$ 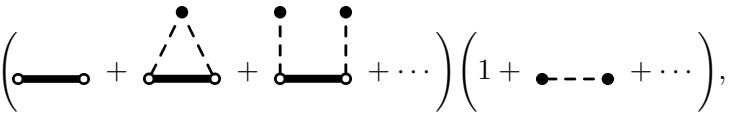 (2.34)

such that

$\frac{\mathcal{N}}{\mathcal{D}} =$ 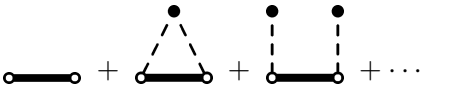 (2.35)

so we are left only with the *fully connected diagrams*.

Dynamical and statistical correlations

The calculations can be explicitly carried out by evaluating the internal products. It comes in useful to define the n-body distribution function associated with the Fermi gas ground-state wavefunction Φ_0

$$g_n^{FG}(\mathbf{r}_1, ..., \mathbf{r}_n) = \frac{1}{\varrho^n} \frac{A!}{(A-n)!} \mathrm{Tr}_1 \ldots \mathrm{Tr}_n \int dx_{n+1} \ldots dx_A |\Phi_0(x_1, \ldots, x_A)|^2, \quad (2.36)$$

such that

$$\begin{aligned} \mathcal{N} = & \frac{1}{2} \int d\mathbf{r}_1 d\mathbf{r}_2 v(\mathbf{r}_{12}) f^2(r_{12}) [\varrho^2 g_2^{FG}(\mathbf{r}_1, \mathbf{r}_2) \\ & + \sum_{n=3}^{A} \frac{\varrho^n}{(n-2)!} \int d\mathbf{r}_3 \cdots d\mathbf{r}_n X^{(n)}(\mathbf{r}_1, \mathbf{r}_2; \mathbf{r}_3, \ldots, \mathbf{r}_n) g_n^{FG}(\mathbf{r}_1, \ldots, \mathbf{r}_n)], \end{aligned} \quad (2.37)$$

and

$$\mathcal{D} = 1 + \sum_{n=2}^{A} \frac{\varrho^n}{n!} \int d\mathbf{r}_1 \ldots d\mathbf{r}_n X^{(n)}(\mathbf{r}_1, \ldots, \mathbf{r}_n) g_n^{FG}(\mathbf{r}_1, \ldots, \mathbf{r}_n). \quad (2.38)$$

Here, it is worth mentioning that correlations arise from two contributions: the dynamical terms $X^{(n)}$ and g_n^{FG}. The former is responsible for the dynamical correlations of the system related to the interactions, while g_n^{FG} accounts for the statistical correlations resulting from the Pauli exclusion principle.

Kinetic energy

The expectation value of the kinetic energy in the correlated ground state is given by

$$\langle T\rangle = \frac{\langle\Phi_0|\mathcal{F}^\dagger T\mathcal{F}|\Phi_0\rangle}{\langle\Phi_0|\mathcal{F}^2|\Phi_0\rangle} \tag{2.39}$$
$$= \frac{1}{N(\Psi_T)}\Big(\frac{-1}{2m}\Big)\sum_i\int dx_1\dots dx_A\Phi_0^*(x_1,\dots,x_A))\mathcal{F}^\dagger\nabla_i^2\mathcal{F}\Phi_0(x_1,\dots,x_A)),$$

where we have defined the normalisation of the correlated state Ψ_T as $N(\Psi_T)$. Now we can use the identity

$$\nabla_i^2(\mathcal{F}\Phi_0) = \mathcal{F}(\nabla_i^2\Phi_0) + 2(\nabla_i\mathcal{F})\cdot(\nabla_i\Phi_0) + \Phi_0(\nabla_i^2\mathcal{F}). \tag{2.40}$$

Using this expression and evaluating the integration in Eq. (2.39) is referred to as Pandharipande-Bethe (PB) form [87]. The first term yields the ground-state energy of the non interacting Fermi gas, i.e.

$$T_F = A\frac{3}{5}\frac{k_F^2}{2m}. \tag{2.41}$$

Now we could write

$$\nabla_i\mathcal{F} = \sum_{j>i}\frac{\nabla_i f(r_{ij})}{f(r_{ij})}\mathcal{F}, \tag{2.42}$$

and

$$\mathcal{F}\nabla_i^2 F = \sum_{j>i}\Big[\frac{\nabla_i^2 f(r_{ij})}{f(r_{ij})} - \frac{(\nabla_i f(r_{ij}))^2}{f^2(r_{ij})}\Big]\mathcal{F}^2 + \sum_{k>j>i}\frac{(\nabla_i f(r_{ij}))\cdot(\nabla_i f(r_{ik})}{f(r_{ik})f(r_{ik})}\mathcal{F}^2 \tag{2.43}$$

such that the calculation of the kinetic energy involves the expectation values of two- and three-body operators, and therefore requires the two- and three-body distribution functions.

An alternative approach would be exploring Clark-Westhaus form of the kinetic energy [82]. It is obtained integrating by parts the last contribution of Eq. (2.40) in Eq. (2.39) and using the identity

$$\sum_i[(\nabla_i\Phi_0^\dagger)\mathcal{F}(\nabla_i\mathcal{F})\Phi_0 - \Phi_0^\dagger(\nabla_i\mathcal{F})\mathcal{F}(\nabla_i\Phi_0)] = 0, \tag{2.44}$$

with the result

$$T_{\rm CW} = \frac{1}{N(\Psi_T)}\Big(\frac{-1}{2m}\Big)\sum_i\int dx_1\dots dx_A\Phi_0^\dagger\mathcal{F}[\mathcal{F}(\nabla_i^2\Phi_0) - (\nabla_i\mathcal{F})^2\Phi_0]. \tag{2.45}$$

Collecting together the two-body contribution to the CW kinetic energy and the interaction potential, one can define an effective potential

$$w(r) = \frac{1}{m}\Big(\frac{\nabla f(r)}{f(r)}\Big)^2 + v(r), \tag{2.46}$$

whose expectation value can be evaluated using the two-nucleon radial distribution function $g_2(r)$. Also, the calculation of the expectation value of the three-nucleon operator arising from the second term in square brackets in Eq. (2.45) requires the three-nucleon distribution function.

Finally, we also report the Jackson-Fennberg form of the kinetic energy [88], which corresponds to integrating by parts Eq. (2.40) in (2.39). It reads

$$T_{\rm JF} = -\frac{1}{4m}\frac{1}{N(\Psi_T)}\sum_i \int dx_1 \dots dx_A [\Phi_0^\dagger \mathcal{F}(\nabla_i^2 \mathcal{F}\Phi_0) - 2(\nabla_i \Phi_0^\dagger \mathcal{F})\cdot(\nabla_i \mathcal{F}\Phi_0) + (\nabla_i^2 \Phi_0^\dagger \mathcal{F})\mathcal{F}\Phi_0]. \tag{2.47}$$

The three different representations of kinetic energy, although theoretically interchangeable, yield different outcomes when implemented through a cluster expansion. For example, the JF kinetic energy is less affected by the approximations involved in the derivation of the three-body distribution function, while it is more affected by the description of the two-nucleon distribution function at short distances. The PB and CW forms, on the other hand, are more sensitive to the contribution of three-body terms. The difference between kinetic energies obtained using different prescriptions provides a measure of uncertainti associated with the truncation of the cluster expansion.

Generalisation to operatorial correlations

In order to achieve more accurate results, state-of-the-art calculations of nuclear matter properties demand the incorporation of more complicated forms of the correlation operator, which is necessary to mirror the structure of the NN interaction. When including spin-isospin correlations, the steps we have followed so far become much more difficult due to the non-commutativity of operators.

In the Jastrow case, a technique called Fermi Hyper-Netted Chain (FHNC) can be efficiently used to carry out the sum of successive many-body clusters (see,e.g., Refs. [8, 89]). For spin-isospin correlations, there is a generalisation referred to as Single Operator Chain (FHNC/SOC), originally developed by Pandharipande and Wiringa [90]. Within this approach, a set of coupled integral equations allowing to sum over the hypernetted chains of central links (FHNC) and single chains of operator links is derived.

A natural way to rewrite the correlation operator in the general case would be

$$F_{12} = \sum_p f^p(r_{12}) O_{12}^p = f^c(r_{12}) + \sum_{p>1} f^p(r_{12}) O_{12}^p, \tag{2.48}$$

where $f^c(r_{12})$ corresponds to the identity operator ($p = 1$). For $f^c(r_{12})$, we can use the same smallness parameter $h(r_{12})$ defined in Eq. (2.20). For $p > 1$,

$$\mathcal{F}^\dagger O_{12}^p \mathcal{F} = X^{(2)}(x_1, x_2) + \sum_{i\neq 1,2} X^{(3)}(x_1, x_2; x_i) + \sum_{i<j\neq 1,2} X^{(4)}(x_1, x_2; x_i, x_j) + \dots \tag{2.49}$$

with

$$X^{(2)}(x_1, x_2) = F_{12}^\dagger O_{12}^p F_{12}, \tag{2.50}$$

$$X^{(3)}(x_1, x_2; x_i) = \mathcal{S}(F_{12}F_{1i}F_{2i})^\dagger O_{12}^p \mathcal{S}(F_{12}F_{1i}F_{2i}) - F_{12}^\dagger O_{12}^p F_{12}. \tag{2.51}$$

Although being a more complex problem, the conceptual foundations of the Jastrow case can be applied to the full operatorial case.

2.2 Renormalisation of nuclear interactions in matter

In CBF perturbation theory, one has to evaluate matrix elements of the bare nuclear Hamiltonian, with the correlation effects embodied in the basis states. Alternatively, it is possible to obtain the same result by transforming the Hamiltonian and using the Fermi gas basis. This approach yields an effective Hamiltonian suitable for use in standard perturbation theory, therefore sidestepping the intricate challenges associated with employing a non-orthogonal basis [91].

The *CBF effective interaction* is *defined* through the matrix element of the bare Hamiltonian in the correlated ground state, according to

$$\langle H \rangle = \langle \Psi_0 | H | \Psi_0 \rangle = T_F + \langle \Phi_0 | \sum_{i<j} v_{ij}^{\rm eff} | \Phi_0 \rangle \,, \tag{2.52}$$

where $|\Phi_0\rangle$ and T_F denote the ground state of the non interacting Fermi gas at density ϱ and the corresponding energy at $T = 0$, respectively, while H is the nuclear Hamiltonian of Eq. (1.14). The correlated ground state is defined as

$$|\Psi_0\rangle = \frac{\mathcal{F}\,|\Phi_0\rangle}{\langle \Phi_0 | \mathcal{F}^\dagger \mathcal{F} | \Phi_0 \rangle^{1/2}}, \tag{2.53}$$

with $\mathcal{F}$ as in Eqs. (2.6) and (2.7). The structure of $v_{ij}^{\rm eff}$ is described in the same basis of Eq. (1.31)

$$v_{ij}^{\rm eff} = \sum_p v_{ij}^{{\rm eff},p}(r_{ij}) O_{ij}^p. \tag{2.54}$$

The determination of the effective interaction from Eq. (2.52) is based on the cluster expansion of the left-hand side, leading to

$$\langle H \rangle = T_F + \sum_n (\Delta E)_n = T_F + \langle \Phi_0 | \sum_{i<j} v_{ij}^{\rm eff} | \Phi_0 \rangle \,, \tag{2.55}$$

where $(\Delta E)_n$ denotes the contribution to the Hamiltonian expectation value arising from n-nucleon clusters.

In early works [92, 93], the effective interaction was obtained keeping only the two-body cluster contribution. While leading to a very simple and easily manageable expression for $v_{ij}^{\rm eff}$, this scheme is not suited to take into account the NNN potential V_{ijk}, which play a dominant role in the high-density regime relevant to neutron stars. A significant improvement has been achieved by the authors of Refs. [94, 95], where they included the effects of NNN microscopic interactions, such as the UIX model. The effective interaction employed to obtain the results discussed in this Thesis has been derived following the procedure described in Ref. [94], using AV6P+UIX potentials [73].

Note that the correlation functions $f^p(r_{ij})$ entering the definition of $v_{ij}^{\rm eff}$ are not the same as those obtained from the minimisation of the variational energy

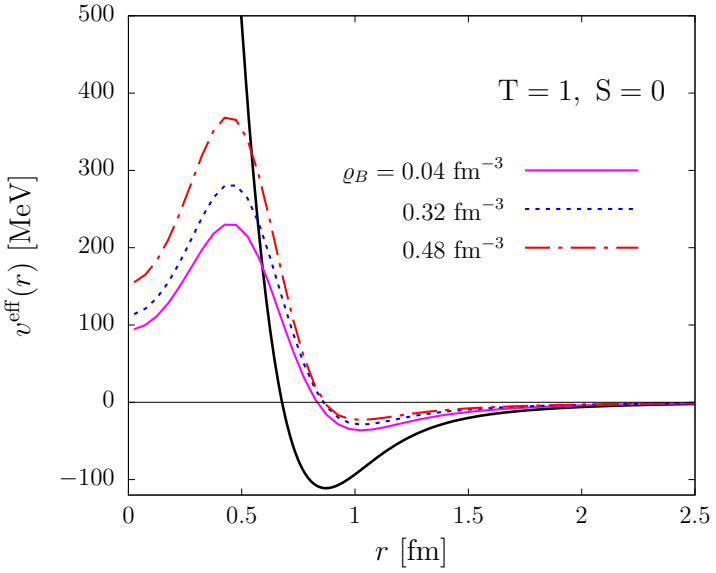

Figure 2.1. Radial dependence of the CBF effective potential in the $S = 0$, $T = 1$ channel. The solid, dashed, and dot-dash lines correspond to baryon number density $\varrho = 0.04$, 0.32 and 0.48 fm^{-3}. For comparison, the thick solid line shows the bare AV6P potential.

of Eq. (2.22). They are adjusted so that the ground state energy computed at first order in $v_{ij}^{\rm eff}$ —that, in the Hartree-Fock approximation —reproduces the value of E_V resulting from highly accurate many-body calculation, carried out using FHNC/SOC or Auxiliary Field Diffusion Monte Carlo (AFDMC), for example. The target values of E_V are simultaneously taken to be the ones of SNM and PNM. This is an important feature, because it allows to evaluate the properties of nuclear matter at fixed density and large neutron excess, which is believed to be present in NS matter.

It is possible to show that, at the two-body level [94],

$$v_{ij}^{\rm eff}\Big|_{\rm 2b} = F_{ij} v_{ij} F_{ij} - \frac{1}{m}(\nabla F_{ij}) \cdot (\nabla F_{ij}). \tag{2.56}$$

For the expressions of the three-body cluster contribution, please see Ref. [94] and references therein.

The derivation of the effective interaction based on the CBF formalism can be seen as a renormalisation of the bare NN potential in coordinate space, while taking into account dynamical and statistical correlations coming from the interactions in the nuclear medium. As a result, we have a screened nuclear interaction whose renormalisation parameter would be the matter density. This feature can be better seen in Fig. 2.1, where we show the $S = 0$, $T = 1$ channel of the effective potential in comparison to the bare AV6P potential. To further illustrate the role of the correlation functions, in Fig. 2.2 we present the curves of f^p at four different densities.

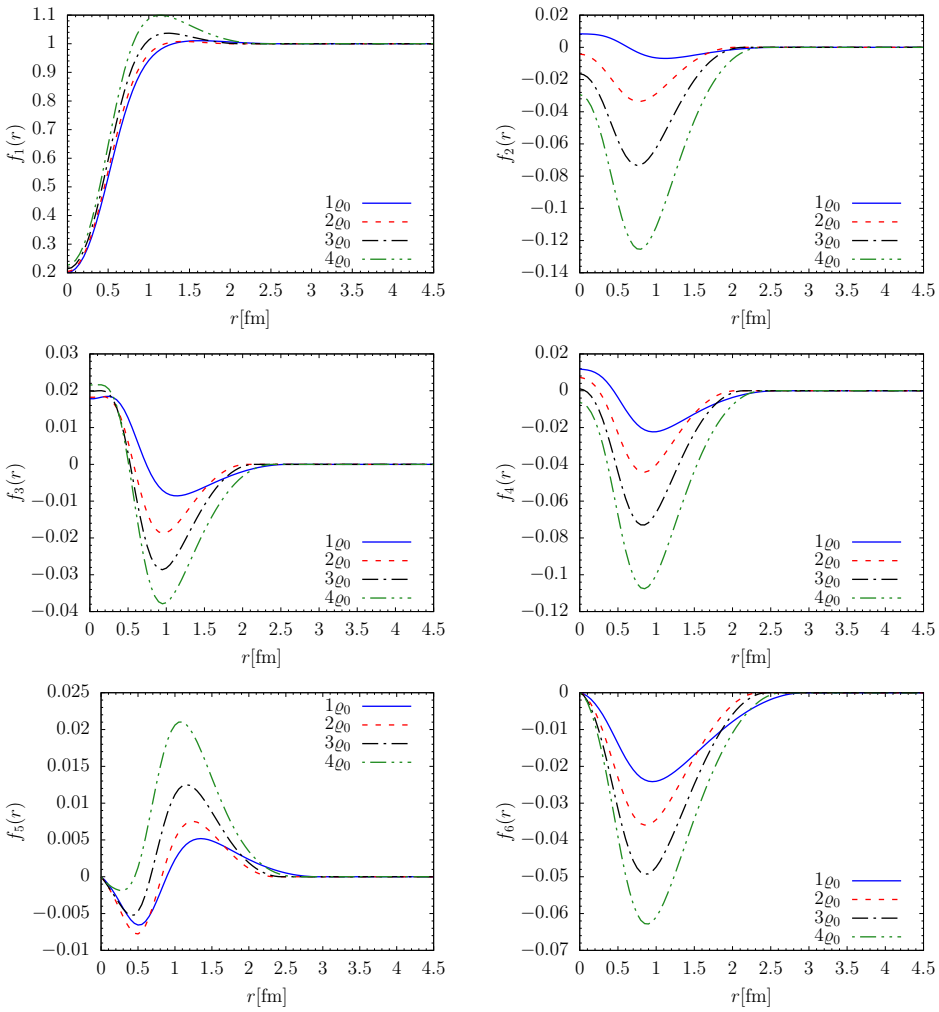

Figure 2.2. Correlation functions that enter the definition of the effective potential (2.52) at $\varrho = 1 - 4\ \varrho_0$.

2.3 Finite-temperature perturbation theory

The basic assumption underlying our treatment of nuclear matter at $T \neq 0$ is that at low-to-moderate temperatures —typically $T \ll m_\pi \approx 140$ MeV, described by the potentials appearing in the Hamiltonian of Eq. (1.14), is largely unaffected by thermal effects. In principle, the CBF effective interaction involves an additional temperature dependence associated with the correlation functions, since the Fermi distribution appears in the Euler–Lagrange equations determining their shape. However, the results of detailed numerical calculations have shown that thermal modifications of the f^p of Eq. (2.6) turn out to be negligibly small up to $T \sim 50$ MeV [96]. The results reported in this Thesis have been obtained using the zero-temperature effective interaction, involving correlation functions computed at $T = 0$, i.e., the same from Fig. 2.2.

Let us consider, for simplicity, a one-component Fermi system. The derivation

of perturbation theory at finite-temperature is based on the solution of the Bloch equation

$$-\frac{\partial \Phi}{\partial \beta} = (H - \mu N)\Phi \ , \tag{2.57}$$

where

$$\Phi(\beta) = e^{-\beta(H-\mu N)} \ , \tag{2.58}$$

with the initial condition $\Phi(0) = 1$; see, e.g., Ref. [97]. In the above equations $\beta = 1/T$, while H and μ denote the Hamiltonian and the chemical potential, respectively.

The perturbative expansion of the grand canonical partition function $Z = \mathrm{Tr}\ \Phi$ is easily obtained exploiting the formal similarity between Eq. (2.57) and the time-dependent Schrödinger equation of quantum mechanics, and rewriting the Hamiltonian in the form

$$H = H_0 + H_I. \tag{2.59}$$

Substitution of Eq. (2.59) into the right-hand side of the Bloch equation, leading to

$$-\frac{\partial \Phi}{\partial \beta} = [(H_0 - \mu N) + H_I]\Phi = (H_0' + H_I)\Phi \ ,$$

shows that the formalism of time-dependent perturbation theory can be readily generalised by replacing $t \to -i\beta$, and using H_0' to define operators in the interaction picture.

The fundamental relation

$$\Omega = -\frac{1}{\beta} \ln Z = -PV = F - \mu N = E - TS - \mu N \ , \tag{2.60}$$

where V is the normalization volume, provides the link between the grand canonical potential Ω, the pressure P, and the free energy $F = E - TS$, with E and S being the energy and entropy of the system, respectively; see, e.g., Ref. [98]. From Eq. (2.60) if follows that

$$P = -\frac{\Omega}{V} \quad , \quad S = -\frac{\partial \Omega}{\partial T} \quad , \quad N = -\frac{\partial \Omega}{\partial \mu} \ . \tag{2.61}$$

In the following, we will discuss the application of the above results to a system described by the Hamiltonian (2.59), with

$$H_0 = \sum_k e_k a_k^\dagger a_k \ , \tag{2.62}$$

where, in general

$$e_k = \frac{\mathbf{k}^2}{2m} + U_k = t_k + U_k \ , \tag{2.63}$$

and

$$H_I = \frac{1}{2}\sum_{k,k',q,q'} \langle k'q'|v|kq\rangle a^\dagger_{k'} a^\dagger_{q'} a_q a_k - \sum_k U_k a^\dagger_k a_k \ . \tag{2.64}$$

Here, the label k specifies both the particle momentum and the discrete quantum numbers corresponding to one-particle states, $a^\dagger_k$ and a_k denote creation and annihilation operators, respectively, and v is the potential describing interparticle interactions. The single-particle potential U_k, which in principle does not affect the results of calculations of physical quantities, is chosen in such a way as to improve the convergence of the perturbative expansion, or fulfil specific conditions; see, e.g., Ref. [78].

It has to be pointed out that, according to Eq. (2.60), the pressure can be written in the form

$$P = \varrho\Big(\mu - \frac{F}{N}\Big) \ , \tag{2.65}$$

with $\varrho = N/V$, implying that at equilibrium, that is, for $P = 0$, $\mu = F/N$. This result is the generalisation of the Hugenholtz-Van Hove theorem [99] to the case of non vanishing temperature.

It should be emphasised that, when used in conjunction with the CBF effective interaction discussed in Section 2.2, the perturbative approach based on the Hamiltonian defined by Eqs. (2.59) and (2.62)-(2.64) allows to take into account two- and three-nucleon interactions in a fully consistent fashion.

2.3.1 Perturbative expansion

At first order in H_I, the grand canonical potential is given by [100]

$$\Omega = \Omega_0 + \Omega_1 \ , \tag{2.66}$$

with

$$\Omega_0 = -\frac{1}{\beta}\sum_k \ln\left\{1 + e^{-[\beta(e_k-\mu)]}\right\} \ , \tag{2.67}$$

$$\Omega_1 = \frac{1}{2}\sum_{kk'} \langle kk'|v|kk'\rangle_A \ n_k n_{k'} - \sum_k U_k n_k \ , \tag{2.68}$$

where $|kk'\rangle_A = |kk'\rangle - |k'k\rangle$ denotes an antisymmetrised two-particle state, and n_k is the Fermi distribution, defined as

$$n_k = \left[1 + e^{\beta(e_k-\mu)}\right]^{-1} \ . \tag{2.69}$$

From Eqs. (2.67) and (2.68) it follows that the free energy per particle

$$\frac{F}{N} = \frac{1}{N}(\Omega_0 + \Omega_1) + \mu \ , \tag{2.70}$$

can be cast in the form

$$\frac{F}{N} = \frac{1}{N}\Big\{ \sum_k t_k n_k + \frac{1}{2}\sum_{k,k'} \langle kk'|v|kk'\rangle_A \; n_k n_{k'} \\ + \frac{1}{\beta}\sum_k \left[n_k \ln n_k + (1-n_k)\ln(1-n_k)\right] + \mu\Big(1 - \frac{1}{N}\sum_k n_k\Big)\Big\} \; . \tag{2.71}$$

In principle, for any assigned values of temperature and chemical potential, the above equations provide a scheme for the determination of the equation of state of nuclear matter at finite temperature, $P = P(\mu, T)$. Because baryon number is conserved by all known interactions, however, in nuclear matter it is more convenient to use baryon density as an independent variable, and determine the chemical potential from the relation

$$\varrho = -\frac{1}{V}\frac{\partial}{\partial\mu}(\Omega_0 + \Omega_1) = \frac{\nu}{V}\sum_k n(k,T) \; . \tag{2.72}$$

In the $T \to 0$ limit the momentum distribution reduces to the Heaviside step function $\theta(\mu - e_k)$, and the chemical potential is given by $\mu = e_{k_F}$, with the Fermi momentum defined as $k_F = \left(6\pi^2\varrho/\nu\right)^{1/3}$.

2.3.2 Thermodynamic consistency

For $T \neq 0$ and density-dependent potentials (as the CBF effective interaction), thermodynamic consistency is not trivially achieved at any given order of perturbation theory. A clear manifestation of this difficulty is the mismatch between the value of pressure obtained from Eq. (2.65) and the one resulting from the alternative—although in principle equivalent—thermodynamic expression

$$P = -\frac{\partial F}{\partial V} = \varrho^2 \frac{\partial}{\partial\varrho}\frac{F}{N} \; . \tag{2.73}$$

A procedure fulfilling the requirement of thermodynamic consistency by construction can be derived from a variational approach, based on minimisation of the trial grand canonical potential [101]

$$\widetilde{\Omega} = \sum_k t_k n_k + \frac{1}{2}\sum_{k,k'} \langle kk'|v|kk'\rangle_A \; n_k n_{k'} \\ + \frac{1}{\beta}\sum_k \left[n_k \ln n_k + (1-n_k)\ln(1-n_k)\right], \tag{2.74}$$

with respect to the form of distribution n_k. Note that the above expression—the use of which is fully legitimate in the variational context—can also be obtained in first order perturbation theory neglecting terms involving $\partial\Omega_1/\partial T$ and $\partial\Omega_1/\partial\mu$ [100].

The condition

$$\frac{\delta\widetilde{\Omega}}{\delta n_k} = 0 \; , \tag{2.75}$$

turns out to be satisfied by the distribution function

$$n_k = \left\{1 + e^{\beta[(t_k+U_k+\delta e)-\mu]}\right\}^{-1} , \tag{2.76}$$

with

$$U_k = \sum_{k'} \langle kk'|v|kk'\rangle_A \; n_{k'} , \tag{2.77}$$

and

$$\delta e = \frac{1}{V}\frac{1}{2}\sum_{k,k'} \langle kk'|\frac{\partial v}{\partial \varrho}|kk'\rangle_A \; n_k n_{k'} . \tag{2.78}$$

Within the above scheme, that reduces to the standard Hartee-Fock approximation in the case of density-independent potentials, all thermodynamic functions at given temperature and baryon density can be consistently obtained using the distribution n_k of Eq. (2.76). Note, however, that, because both U_k and δe depend on n_k, see Eqs. (2.77) and (2.78), calculations must be carried out self-consistently, applying an iterative procedure.

2.4 The equation of state of nuclear matter

In the following, we will assume the notation for the matter density as

$$\varrho = \sum_\lambda \varrho_\lambda = \varrho \sum_\lambda x_\lambda, \tag{2.79}$$

where $\lambda = 1, 2, 3, 4$ labels spin-up protons, spin-down protons, spin-up neutrons, and spin-down neutrons. In non-polarized matter, which corresponds to our case in this work, we have $x_1 = x_2 = Y_p/2$ and $x_3 = x_4 = Y_n/2$. As we are explicitly writing spin-isospin with λ, now k will refer only to momentum states.

For the gran canonical potential (2.74), we have

$$\begin{aligned}\widetilde{\Omega} = &\sum_{\lambda\mathbf{k}} t_{\lambda k} n_\lambda(k,T) + \frac{1}{2}\sum_{\lambda\mathbf{k},\lambda'\mathbf{k}'} \langle \lambda k, \lambda' k'|v|\lambda k, \lambda' k'\rangle_A \; n_\lambda(k,T) n_{\lambda'}(k',T) \\ &+ \frac{1}{\beta}\sum_{\lambda\mathbf{k}} \left[n_\lambda(k,T)\ln n_\lambda(k,T) + (1-n_\lambda(k,T))\ln(1-n_\lambda(k,T))\right],\end{aligned} \tag{2.80}$$

and the same reasoning applies for the internal energy and the entropy. The former can be written as

$$\frac{E}{N} = \frac{1}{N}\Big\{\sum_{\lambda\mathbf{k}} \frac{\mathbf{k}^2}{2m} \; n_\lambda(k,T) + \frac{1}{2}\sum_{\lambda\mathbf{k}}\sum_{\lambda'\mathbf{k}'} \langle \lambda k, \lambda' k'|v^{\text{eff}}|\lambda k, \lambda' k'\rangle_A \; n_\lambda(k,T) n_{\lambda'}(k',T)\Big\} . \tag{2.81}$$

while the latter is given by

$$\frac{S}{N} = -\frac{1}{N}\sum_{\lambda\mathbf{k}} \Big\{n_\lambda(k,T)\ln n_\lambda(k,T) + \left[1-n_\lambda(k,T)\right]\ln\left[1-n_\lambda(k,T)\right]\Big\} . \tag{2.82}$$

The free energy, F, can be easily obtained through

$$\frac{F}{N} = \frac{1}{N}(E - TS) \tag{2.83}$$

For the single-particle spectrum, we have

$$e_{\lambda k} = e^{\rm HF}_{\lambda k} + \delta e \ , \tag{2.84}$$

with

$$e^{\rm HF}_{\lambda k} = \frac{{\mathbf{k}_\lambda}^2}{2m} + \sum_{\lambda' \mathbf{k}'} \langle \lambda k, \lambda' k' | v | \lambda k, \lambda' k' \rangle_A \ n_{\lambda'}(k', T) \ , \tag{2.85}$$

and

$$\delta e = \frac{1}{V}\frac{1}{2} \sum_{\lambda \mathbf{k}} \sum_{\lambda' \mathbf{k}'} \langle \lambda k, \lambda' k' | \frac{\partial v}{\partial \varrho} | \lambda k, \lambda' k' \rangle_A \ n_\lambda(k, T) n_{\lambda'}(k', T), \tag{2.86}$$

with, obviously,

$$n_\lambda(k, T) = \Big\{ 1 + \exp[(e_{\lambda k} - \mu_\lambda)/T] \Big\}^{-1} \ . \tag{2.87}$$

Moreover, when carrying out the calculations in the thermodynamic limit, we have

$$\sum_k \to \int \frac{d^3k}{(2\pi)^3/V}, \tag{2.88}$$

yielding, then,

$$\varrho_\lambda = \int \frac{d^3k}{(2\pi)^3} n_\lambda(k, T). \tag{2.89}$$

The formulae used to evaluate these expressions are given in Appendix B.

In order to illustrate fundamental results of the formalism described above, in Fig. 2.3 we show the density and temperature dependence of the free energy per nucleon (2.83) of SNM and PNM, corresponding to a proton fraction $Y_p = 0.5$ and 0, respectively.

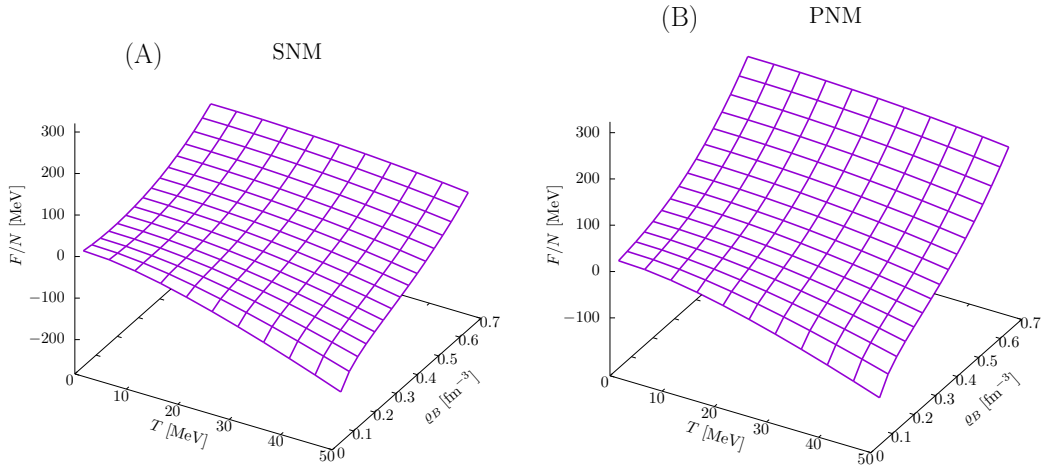

Figure 2.3. Density and temperature dependence of the free energy per nucleon of SNM (A) and PNM (B), computed using Eqs. (2.81)-(2.82), with the CBF effective interaction.

2.5 Matter in beta equilibrium

In the temperature regime discussed in this paper, thermal modifications of nuclear matter properties arise primarily from the Fermi distributions, defined by Eq. (2.87). Comparison to the $T \to 0$ limit shows that the probability distribution $n_\lambda(k, T > 0)$ is reduced from unity in the region corresponding to $\mu_\lambda - T \lesssim e_{\lambda k} \lesssim \mu_\lambda$, and acquires non vanishing positive values for $\mu_\lambda \lesssim e_{\lambda k} \lesssim \mu_\lambda + T$. It follows that, for any given temperature T, the extent of thermal modifications to the Fermi distribution is driven by the ratio $2T/\mu_\lambda$. This observation in turn implies that, because the chemical potential is a monotonically increasing function of the particle density ϱ_λ over a broad range of temperatures, for any given T thermal effects turn out to be more significant at lower ϱ_λ. On the other hand, they become vanishingly small in the high-density regime, in which degeneracy dominates.

The density-dependence of thermal effects—that also affects the particle energies and chemical potentials, defined by Eqs. (2.84) and (2.89), respectively—plays a significant role in the determination of the properties of multicomponent systems, such as charge-neutral β-stable matter, in which different particles have different densities. The latter is the case of NS matter [102–104].

In charge-neutral matter consisting of neutrons, protons and leptons in equilibrium with respect to the weak interaction processes

$$n \to p + \ell + \bar{\nu}_\ell \quad , \quad p + \ell^- \to n + \nu_\ell \ , \tag{2.90}$$

where $\ell = e, \mu$ labels the lepton flavour, the proton fraction Y_p is uniquely determined by the equations

$$\mu_n - \mu_p = \mu_\ell \quad , \quad Y_p = \sum_\ell Y_\ell \ . \tag{2.91}$$

At densities such that the electron chemical potential does not exceed the rest mass of the muon, $m_\mu = 105.7$ MeV, the sum appearing in the above equation includes

electrons only. At higher densities —typically at $\varrho \gtrsim \varrho_0$ —the appearance of muons becomes energetically favoured, and must be taken into account.

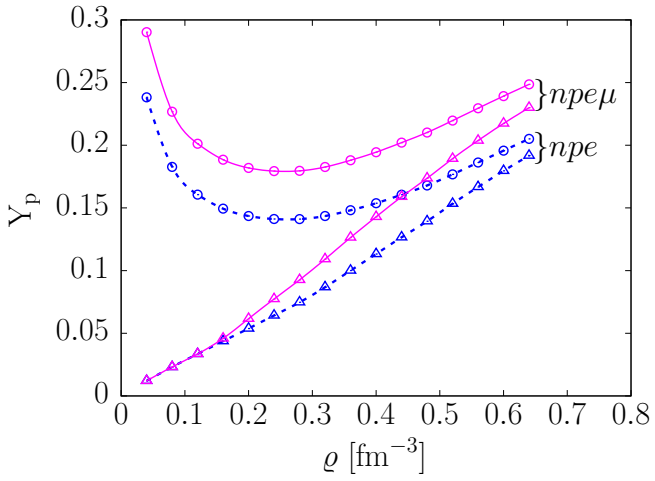

Figure 2.4. Density dependence of the proton fraction in charge-neutral β-stable matter. Solid lines marked with triangles and circles correspond to $npe\mu$ matter at $T = 0$ and 50 MeV, respectively. The same quantities in npe matter are represented by dashed lines.

The solid lines of Fig. 2.4 show the density dependence of the proton fractions corresponding to β-equilibrium of matter consisting of protons, neutrons, electrons and muons, or $npe\mu$ matter, at $T = 0$ (triangles) and 50 MeV (circles) [74]. For comparison, the same quantities in npe matter, in which the muon contribution is not included, are displayed by the dashed lines. The results have been obtained assuming that neutrinos do not interact with matter, and have therefore vanishing chemical potential. The discussion involving neutrinos is left for the next chapter.

The most prominent thermal effect is a significant departure from the monotonic behaviour observed in cold matter. The emergence of a minimum in the density dependence of the proton fraction results from the balance between the thermal and degeneracy contributions to the chemical potentials appearing in Eq. (2.91). For $T \gtrsim 20$ MeV and low density, typically $\varrho \lesssim \varrho_0$, the thermal contribution—whose leading order term can be written in the form $\delta\mu_\lambda \propto T^2/\varrho_\lambda^{1/3}$—turns out to be much larger for protons than for neutrons, and β-equilibrium requires large proton fractions. The results displayed in Fig. 2.4, showing that Y_p does not exceed 25% for $\varrho_0/2 \leq \varrho \leq 4\varrho_0$, imply that in β-stable matter thermal effects affect mainly the proton distributions.

2.5.1 Fermi distributions

The Fermi distribution of Eq. (2.87) depends on temperature both explicitly, through the factor $\beta = 1/T$ appearing in the argument of the exponential, and implicitly, through the T-dependence of both $e_{\lambda k}$ and μ_λ. Because the calculation of single-particle energies and chemical potentials in turn involves the Fermi distribution, $e_{\lambda k}$, μ_λ and $n_\lambda(k, T)$ must, in fact, be determined self-consistently, applying an iterative procedure.

Figure 2.5 shows the distributions of neutrons and protons in charge-neutral β-stable $npe\mu$ matter at baryon density $\varrho = 0.32$ fm^{-3}.

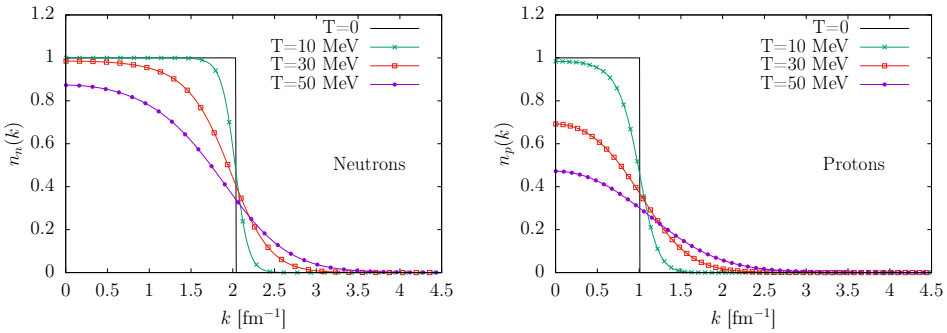

Figure 2.5. Neutron and proton Fermi distributions in charge-neutral β-stable $npe\mu$ matter at baryon density $\varrho = 0.32$ fm^{-3}.

It is apparent that, as pointed out in the previous section, thermal modifications to $n_\lambda(k,T)$—extending over a region of width $2T$ around the Fermi momentum $k_{F_\lambda} = (6\pi^2\varrho_\lambda)^{1/3}$—depend on *both* temperature *and* density. As a consequence, for any given temperature T they are more pronounced in the case of protons, whose density is suppressed by a factor $\mathrm{Y}_p/(1-\mathrm{Y}_p) \ll 1$ with respect to the neutron density.

2.5.2 Single-nucleon properties

The proton and neutron spectra employed to calculate the Fermi distributions of Fig. 2.5—corresponding to β-stable $npe\mu$ matter at baryon density $\varrho = 2\varrho_0$—are displayed in Fig. 2.6. It is apparent that $e_{\lambda k}$ is an increasing function of temperature at all values of k, with the T-dependence being stronger at lower momentum. At $k = 0$ the difference between the energies corresponding to $T = 0$ and 50 Mev reaches ~ 35.8 MeV for protons, and ~ 17.5 MeV for neutrons. In the case of protons, a ~ 29 MeV increase with respect to the zero-temperature spectrum is still clearly visible at $k = k_{F_p}$, $k_{F_p} = 1.01$ fm^{-1} being the proton Fermi momentum, while the $T = 0$ and 50 MeV neutron spectra at $k = k_{F_n}$, with $k_{F_n} = 2.04$ fm^{-1}, are nearly indistinguishable.

As an illustration of the overall decrease of thermal effects with increasing baryon density, Fig. 2.7 shows the proton and neutron spectra in β-stable $npe\mu$ matter at $\varrho = 0.48$ fm^{-3}.

In theoretical calculations of nuclear matter properties of astrophysical interest—such as the neutrino emission rates [68], and the shear and bulk viscosity coefficients [67, 105, 106]—the relevant information comprised in proton and neutron spectra is captured by the corresponding effective masses $m^\star_\lambda$, defined by the equations

$$\frac{1}{m^\star_\lambda} = \left(\frac{1}{k}\frac{de_{\lambda k}}{dk}\right)_{k=k_{F_\lambda}} . \tag{2.92}$$

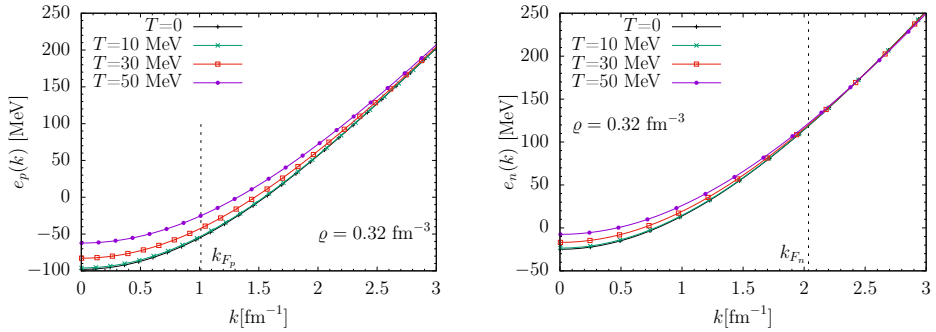

Figure 2.6. Neutron and proton spectra in β-stable $npe\mu$ matter at baryon density $\rho = 0.32$ fm^{-3}, and temperatures in the range $0 \leq T \leq 50$ MeV.

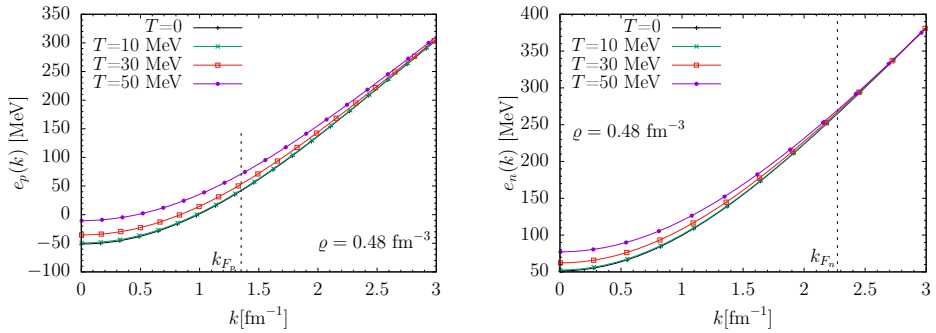

Figure 2.7. Same as in Fig. 2.6, but for matter at baryon density $\varrho = 0.48$ fm^{-3}.

The role played by the effective masses can be readily grasped considering that they determine the dispersion relations of matter constituents, which in turn affect their collision rates through both the incident flux and the available phase space.

The density dependence of the proton and neutron effective masses of charge-neutral β-stable $npe\mu$ matter at temperature $0 \leq T \leq 50$ MeV is illustrated in Fig. 2.8. It clearly appears that, regardless of temperature, $m^\star_\lambda$ is a monotonically decreasing function of baryon density. For neutrons, thermal effects—measured by the departure from the zero-temperature effective mass—turn out to be limited to $\sim 5\%$ over the whole temperature and density range considered. For protons, on the other hand, their size for $T = 50$ MeV turns out to be $\sim 25\%$ at $\varrho = \varrho_0$, and is still $\gtrsim 10\%$ at $\varrho = 4\varrho_0$.

The nucleon effective masses are routinely used to parameterise the momentum dependence of the nucleon spectra in cold nuclear matter according to [68]

$$e_{\lambda k} = \frac{k^2}{2m^\star_0} + U_\lambda \ , \tag{2.93}$$

where $m^\star_0$ denotes the value of $m^\star_\lambda$ at $T = 0$, while the offset U_λ is determined by the requirement that the above approximation reproduce the spectrum obtained from the full microscopic calculation in the $k \to 0$ limit.

In Fig. 2.9 the proton spectra in β-stable $npe\mu$ matter at baryon density $\varrho = 0.32$ fm^{-3} and temperature $T = 0$ and 50 MeV, obtained from Eqs. (2.84)-(2.86), are compared to those computed using Eq. (2.93). At $T = 0$ the quadratic

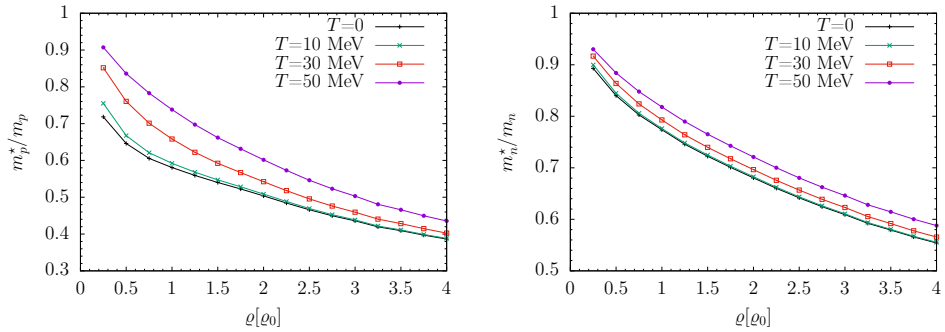

Figure 2.8. Density dependence of the proton and neutron effective masses of charge-neutral β-stable matter at temperature $0 \leq T \leq 50$ MeV. Baryon densities are measured in units of the equilibrium density of cold isospin-symmetric matter.

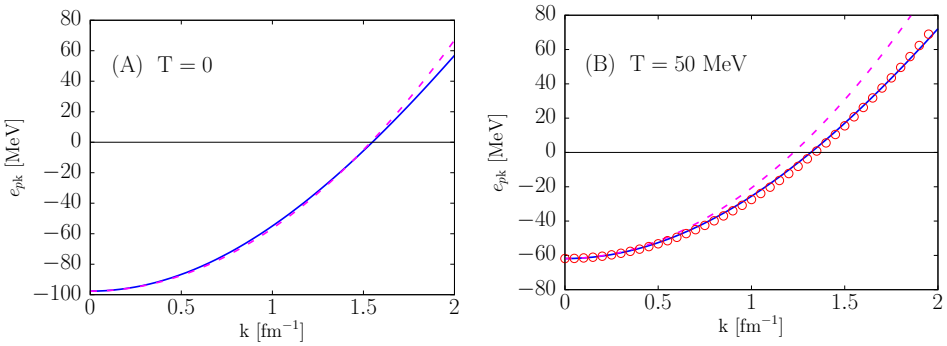

Figure 2.9. Momentum dependence of the proton spectrum in charge-neutral β-stable matter at baryon density $\varrho = 2\varrho_0$ and temperature $T = 0$ (A) and 50 MeV (B). The solid and dashed lines represent the result of full microscopic calculations and the approximation of Eq. (2.93), respectively. The open circles in panel (B) have been obtained using the quadratic approximation with $m_0^\star$ replaced by the effective mass computed at $T = 50$ MeV.

approximation turns out to be remarkably accurate up to momenta largely above the Fermi momentum, $k_{F_p} = 1.01$ fm^{-1}. At $T = 50$ MeV, on the other hand, the agreement between the results of the two calculations is somewhat degraded; the discrepancy is $\sim 25\%$ at $k = k_{F_p}$, and monotonically increases with k.

The spectra displayed in the right panel of Fig. 2.9 clearly show that the accuracy of Eq. (2.9) at $T > 0$ can be significantly improved by taking into account the temperature dependence of the effective mass, which amounts to replacing $m_0^\star$ with the appropriate finite-temperature value, obtained from Eq. (2.92).

In the literature, the temperature dependence of $e_{\lambda k}$ is often disregarded, and the properties of nuclear matter at $T > 0$ are calculated using zero-temperature spectra. This approximation, referred to as *Frozen Correlations Approximation* (FCA), has been recently employed in the studies of binary neutron star mergers of Figura *et al.* [64, 65]. The results reported in Ref. [107] suggest that the FCA has a nearly negligible effect on the thermodynamic properties of nuclear matter at $T \lesssim 30$ MeV. However, its accuracy has been shown to deteriorate at larger temperatures [108]. The validity of the assumption underlying the FCA can be

gauged from Figs. 2.6-2.7. The implications of using this approximation scheme in calculations of nuclear matter properties will be discussed further in the next section.

2.5.3 Chemical potentials and matter composition

Within the theoretical approach underlying our work, thoroughly discussed in Ref. [32], thermodynamic consistency is satisfied by construction. To illustrate this property, in Fig. 2.10 the chemical potential defined in Eq. (2.89) is compared to the one obtained from the thermodynamic definition

$$\mu_\lambda = \Big(\frac{\partial F}{\partial N_\lambda}\Big)_{V,N_{\lambda'\neq\lambda}} \ , \tag{2.94}$$

using the free energy of Eq. (2.83).

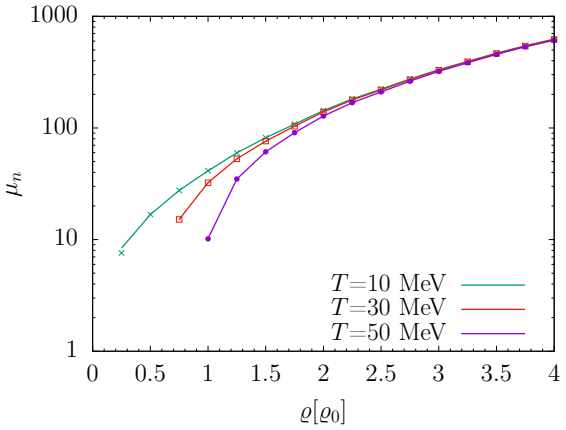

Figure 2.10. Comparison between the neutron chemical potential in pure neutron matter computed using Eq. (2.89), represented by the solid lines, and that obtained from the thermodynamic definition using the free energy of Eq. (2.83).

The chemical potentials of protons and neutrons in charge-neutral β-stable matter at temperature $T = 0$ and 50 MeV are displayed in Fig. 2.11 as a function of baryon density. For comparison, the difference $\mu_n - \mu_p = \mu_e$ is also shown.

Thermal effects on chemical potentials can be analysed considering the difference

$$\delta\mu_{\lambda,\mathrm{th}} = \mu_\lambda - \mu_{\lambda,0} \ , \tag{2.95}$$

with $\mu_{\lambda,0}$ being the value of μ_λ in cold matter at fixed baryon density ϱ and particle fraction x_λ. Figure 2.12 illustrates the temperature dependence of $\delta\mu_{n,\mathrm{th}}$ in charge-neutral β-stable matter at baryon density $\varrho = 2\varrho_0$.

Because thermal effects in β-stable matter have different impact on proton and neutron properties, the capability to accurately predict β-equilibrium and matter composition using FCA must be carefully investigated. The results of numerical calculations carried out within our approach indicate for temperatures up to $T = 50$ MeV the discrepancy between the proton fractions obtained from FCA and the exact results never exceeds $\sim 3\%$ over the considered range of baryon density.

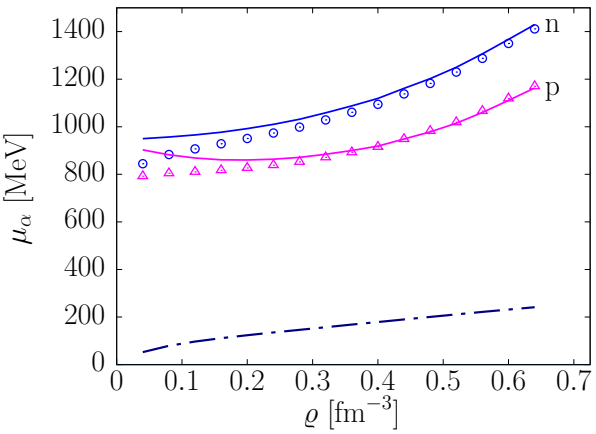

Figure 2.11. Density dependence of the chemical potentials of protons (p) and neutrons (n) in β-stable matter at $T = 50$ MeV. For comparison, the corresponding quantities at $T = 0$ are shown by the solid lines. The dot-dash line represents the difference $\mu_n - \mu_p$ at $T = 50$ MeV.

2.5.4 Internal energy and free energy

The results of a detailed study of the properties of cold nuclear matter—performed by the authors of Ref. [73] using the CBF effective interaction discussed in this article—are collected in Table 2.1. This analysis shows that the AV6P+UIX Hamiltonian reproduces the correct equilibrium density of isospin-symmetric matter, and yields values of the compressibility module and symmetry energy largely compatible with the available data. As for the energy per nucleon, it should be kept in mind that, because kinetic and interaction energies largely cancel one another, the 5 MeV discrepancy in the value of $E(\rho_0)/N$ translates into a $\sim 15\%$ underestimate of the empirical interaction energy. This result is within $\sim 7\%$ of that reported by Akmal *et al.* [37], who performed an accurate variational calculation of SNM with the full AV18+UIX Hamiltonian.

The density and temperature dependence of the internal energy and entropy per baryon of β-stable matter, defined according to Eqs. (2.81) and (2.82), respectively, is illustrated in Figs. 2.13 and 2.14.

	ρ_0 [fm^{-3}]	$E(\rho_0)/N$ [MeV]	K_0 [MeV]	$E_{\rm sym}(\rho_0)$ [MeV]
Ref. [73]	0.16	-11.	210.	30.9
Experiment	0.16	-16.	$240. \pm 20.$	31.6 ± 2.66

Table 2.1. Properties of isospin-symmetric matter at $T = 0$ obtained by the authors or Ref. [73] using the CBF effective interaction described in this article. The experimental values of the compressibility module, K_0, and symmetry energy, $E_{\rm sym}(\rho_0)$, are taken from Refs. [10, 11] and [15], respectively.

Figure 2.13 shows that, for any given ϱ, the internal energy is an increasing func-

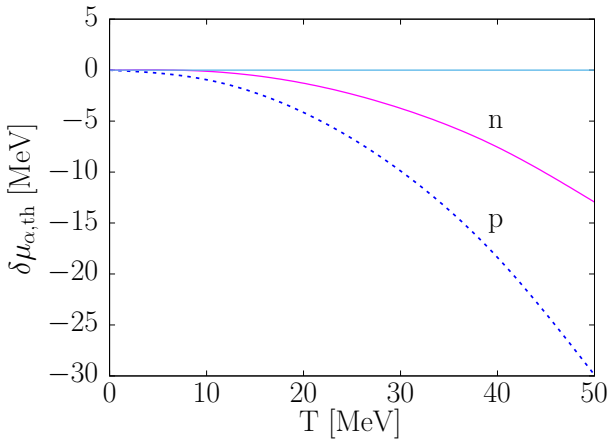

Figure 2.12. Temperature dependence of the thermal contribution to the proton (p) and neutron (n) chemical potentials, defined by Eq. (2.95), in β-stable matter at baryon density $\varrho = 2\varrho_0$.

tion of temperature. However, the concurrent increment of the proton fraction with T, discussed in Section 2.5, leads to the appearance of a minimum for temperatures larger than 10 MeV.

As expected, thermal contributions to the internal energy turn out to be less important at higher ϱ. However, for $T > 10$ MeV they are still significant at densities as high as $4\varrho_0$.

2.6 Parameterising thermal effects

The description of thermal effects on the thermodynamic functions determining the EOS, that is, pressure and energy density, is of paramount importance in view of astrophysical applications. The number of available EOSs of nuclear matter at $T \neq 0$ is much smaller when compared to the corresponding figure for cold matter. Moreover, the implementation of microscopic EOSs in numerical simulation of processes such as a binary neutron star merger involves non trivial difficulties [109, 110].

These above problems are often circumvented using simple but physically sound parameterisation of the EOSs. An extensively used expression is based on the so-called "hybrid-EOS" approach, in which thermal contributions to pressure and energy density are described using an approximation based on an oversimplified parameterisation called "hybrid-EOS" approach, in which thermal modifications of the thermodynamic functions of cold nuclear matter are approximated by the corresponding quantities of an ideal fluid [64, 111–115].

Within this scheme, pressure and internal energy per nucleon are respectively written in the form

$$p = p_{\mathrm{cold}} + p_{\mathrm{th}} \ ,$$
$$e = e_{\mathrm{cold}} + e_{\mathrm{th}} \ ,$$

and the thermal contribution to the pressure at nucleon density ϱ and temperature

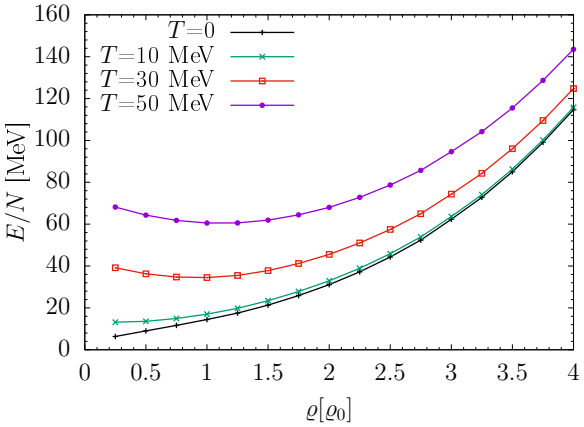

Figure 2.13. Internal energy per baryon of beta-stable matter as a function of baryon density for different temperatures. Note that ϱ is given in units of the equilibrium density of cold isospin-symmetric matter, $\varrho_0 = 0.16$ fm^{-3}.

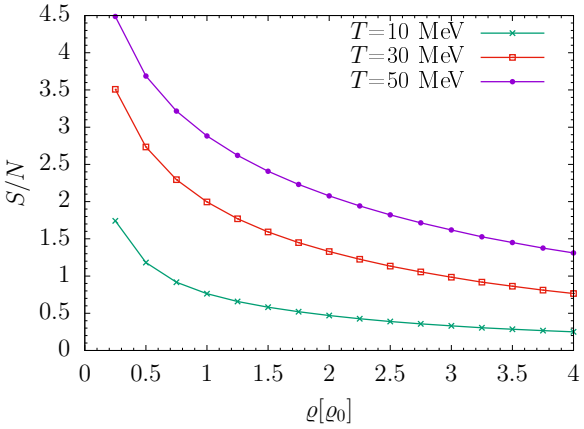

Figure 2.14. Entropy per baryon of beta-stable matter as a function of density for different temperatures. Note that ϱ is given in units of the equilibrium density of cold isospin-symmetric matter, $\varrho_0 = 0.16$ fm^{-3}.

T is parameterised by the adiabatic index, $\Gamma_{\rm th}$, according to

$$p_{\rm th}(\varrho, T) = \varrho\ e_{\rm th}(\Gamma_{\rm th} - 1)\ . \tag{2.96}$$

The above procedure involves the drastic assumption that the adiabatic index be independent of both density and temperature. However, a comparison between the pressure obtained from Eq. (2.96) and that resulting from microscopic calculations based on advanced models of nuclear dynamics shows that $\Gamma_{\rm th}$ does, in fact, depend strongly on density, and that the dependence on temperature, while being weaker, is also non negligible [64].

As pointed out in the previous sections, the results of microscopic calculations clearly signal a strong interplay between the dependencies of the nuclear matter properties on density and temperature. This feature obviously questions the adequacy of the assumption that thermal contributions to the EOS be the same to all densities.

Motivated by this observation, Raithel *et al.* have recently proposed a model that explicitly takes into consideration the effect of matter degeneracy [1, 2].

Rather than using the ideal fluid EOS in the whole density range, the authors of Ref. [1] employ the Sommerfeld expansion described by Constantinou *et al.* [116] in the region high ϱ. This formalism allows to write the deviations of the thermodynamic functions from their zero-temperature values as series of powers of T. The calculation of the next-to-leading order term involves the nucleon effective mass and its derivatives, which implies that a model of nuclear dynamics at $T \neq 0$ is needed beforehand.

In order to make their parameterisation as general as possible, Raithel *et al.* [1] considered a set of RMF models for which the effective masses at different temperatures are available in the literature, and performed a fit using analytical models, such as piecewise polytropes, as the zero-temperature baseline.

Our goal here is to establish the extent to which the results reported in Ref. [1] stand, when compared to an EOS obtained within the framework of NMBT, rather than the RMF approach. We use the parameter values $n_0 \sim 0.13$ fm^{-3} and $\alpha \sim 0.9$ —see Box 1 of Ref. [1] and the erratum, Ref. [2]—to obtain first the effective mass, and subsequently the internal energy per baryon and the matter pressure. Note that the results reported in Ref. [1] do not include the contribution of muons. Therefore, our analysis will be limited to the case of *npe* matter.

In Fig. 2.15 we show a comparison between the internal energy per baryon of β-stable *npe* matter obtained from the approach described in the previous section (solid lines) and the fit of Refs. [1, 2] (dashed lines). It is apparent that at $T = 10$ MeV, the agreement is almost perfect, while discrepancies—the size of which increases with increasing T—are clearly visible at larger temperatures. The maximum relative error between the fit and the miscroscopic calculation at $T = 50$ MeV (30 MeV) turns out to be $\sim 16\%$ ($\sim 11\%$), and occurs at density $\sim 1.5\varrho_0$ ($\sim \varrho_0$).

We have also analysed the accuracy of the approximation of Raithel *et al.* [1] for the pressure. A comparison with the results obtained from our microscopic approach, illustrated in Fig. 2.16, shows a good agreement over the temperature range employed. The parameterisation of Ref.[1] appear to reasonable take into account the effects of degeneracy at all densities.

In order to provide a quantitative estimate of the validity of the the approximations involved in the parameterisation of pressure, in Fig. 2.17 we report the relative difference

$$\frac{\Delta P}{P} = \frac{(P_{\rm approx} - P)}{P} \ , \tag{2.97}$$

where P is the result of our calculation, as a function of baryon density. It is apparent that for $T = 10$ MeV, the error reaches $\sim$11% at $0.5\varrho_0$ and decreases with larger densities. For the highest temperature, $T = 50$ MeV, the relative error stays always smaller than $\sim$6%.

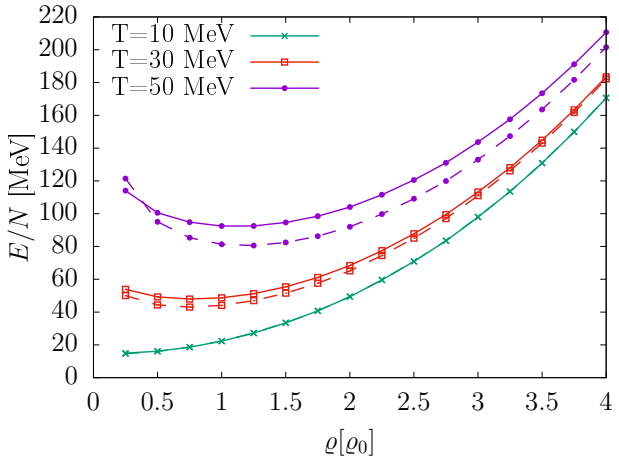

Figure 2.15. Density dependence of the internal energy per baryon of *npe* matter in β-equilibrium. Solid and dashed lines correspond to the results of our calculations and to the fit of Refs. [1, 2], respectively.

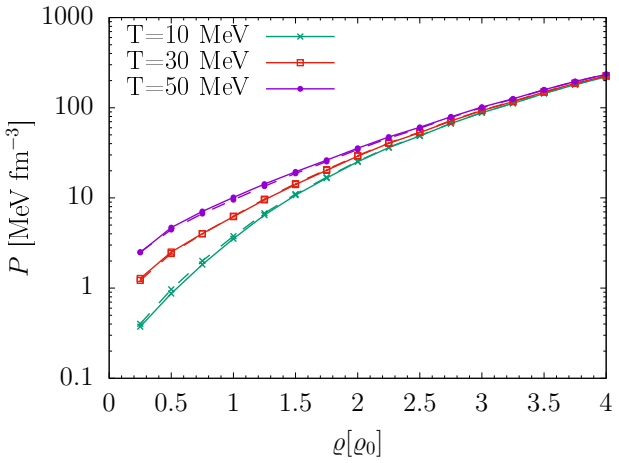

Figure 2.16. Comparison between the pressure of β-stable *npe* matter obtained using the approximate model of Ref. [1, 2] (dashed lines) and the microscopic approach described in this work (solid lines).

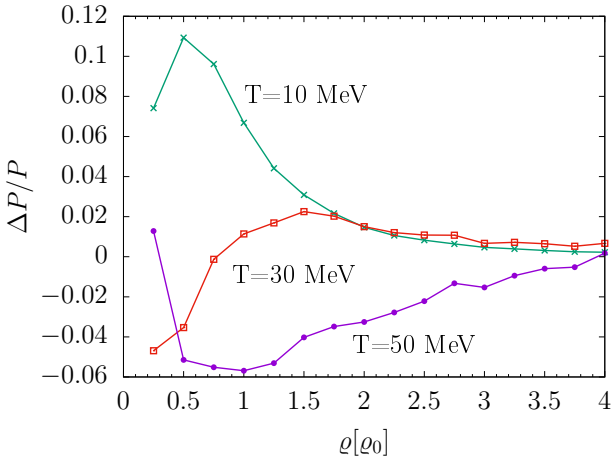

Figure 2.17. Relative difference between the pressure of β-stable *npe* matter obtained using the model of Raithel *et al.* [2] and that resulting from the microscopic approach described in this work.

Chapter 3

Neutrino mean free path and trapping

Weak interactions and neutrino transport are essential to describe hot dense matter in proto-neutron star (PNS) evolution or in a binary neutron star (BNS) merger. They are directly related to the cooling of the compact remnant and to out-of-equilibrium phenomena of the dynamic system, such as bulk viscosity [67, 75, 106, 117–121]. As discussed in the last chaper, the thermodynamic conditions of these systems are extreme, with densities up to several times the nuclear saturation density and temperatures ranging from a few MeV to tens of MeV.

Neutrino emissivity plays the most important role in the thermal evolution of these compact objects [122, 123], while the most important ingredient of neutrino transport calculations is the neutrino opacity [124–127]. The latter is assessed by calculating the neutrino cross section and mean free path (MFP), where both charged current and neutral current reactions contribute to the calculation of these properties. On the charged current side, the most important ones are the so-called Urca reactions, being split into two categories: direct (dUrca) and modified (mUrca). The dUrca reactions are written as

$$\begin{aligned} n &\to p + l + \bar{\nu}_l, \\ p + l &\to n + \nu_l, \end{aligned} \tag{3.1}$$

while mUrca is represented by

$$\begin{aligned} n + N &\to p + N + l + \bar{\nu}_l, \\ p + N + l &\to n + N + \nu_l, \end{aligned} \tag{3.2}$$

where $N = n,\ p$ (neutron and proton branch, respectively). In this Thesis, the only baryons we consider are nucleons, so we limit our discussion to nucleonic Urca reactions. The lepton l stands for e^- or μ^-.

The dUrca reaction is the most powerful, being associated to what is called *rapid* cooling of NSs. That is related to a larger reaction rate with respect to other reactions taking place in the star. Nonetheless, it is known there is a density threshold in the degenerate limit ($T/T_F \ll 1$), which may not be achieved in the interior of stable NSs depending on the maximum density that is present in the core [122].

The mUrca process is permitted below the dUrca threshold due to the presence of the spectator nucleon N, which brings additional momentum to the reaction. Despite being open for a much broader density range, the mUrca reaction rate is small and therefore it is associated to *slow* cooling.

On the neutral current side, the most relevant reactions are neutrino-nucleon scattering and neutrino pair bremsstrahlung from nucleon-nucleon scattering

$$\nu + N \to \nu + n, \tag{3.3}$$

$$N_1 + N_2 \to N_1 + N_2 + \nu + \bar{\nu}, \tag{3.4}$$

where a similar analysis applies. There are analogous reactions involving only leptons, but they are much weaker than the above-mentioned ones. If one considers the possibility of hyperons and deconfined quark matter, there will be a plethora of neutrino reactions that can take place in β-equilibrated matter (see,e.g., Ref. [122]). In this Thesis, we will not study purely leptonic reactions, given that we are interested in understanding how the realistic thermal effects in nuclear matter play a role in dynamical properties.

Neutrinos, being weakly interacting particles, can freely escape from the dense interior of *cold* neutron stars, carrying away significant amounts of energy. The opacity of neutrinos, determined by their scattering and absorption processes within the dense nuclear matter of neutron stars, affects the rate at which thermal energy is radiated away. This, in turn, impacts the cooling timescale of neutron stars and influences various observable properties, such as their surface temperature and luminosity. The opacity depends intricately on both density and temperature within neutron stars. As density increases towards the core, neutrino interactions become more frequent due to the higher density of scattering centers. Additionally, at higher temperatures, thermal energy enables more energetic collisions between neutrinos and surrounding particles, further enhancing opacity. Generally speaking, for a given density ϱ, there will be a temperature $T_{\rm tr}$ for which neutrinos will become *trapped*. In this case, chemical equilibrium should be computed taking into account the non vanishing neutrino chemical potential.

The criterion assumed to determined if neutrinos are trapped is the comparison between their mean free path λ and the stellar radius R. If $\lambda \lesssim R \sim 10$ km, we say that we should consider trapped neutrinos, and, therefore, a non vanishing chemical potential in the calculation of beta equilibrium. Clearly, over the whole density range present in an NS, there will be regions where neutrinos would be trapped and others where they would not.

The mean free path of neutrinos and anti-neutrinos in NS matter has been calculated for several decades with increasing levels of sophistication [128–132]. The main challenges are related to the inclusion of medium effects in the reaction rates, alongside the use of a fully thermodynamically consistent EOS at $T > 0$ that works as the basic ingredient of the calculation. In the direction of adding medium effects, Refs. [94, 95] have remarkably calculated the effects of nuclear correlations on the neutrino MFP based on the CBF effective interaction for PNM and SNM and $T = 0$.

In this Chapter, we compute the neutrino MFP associated to the reactions (3.1) and (3.3). The formalism utilised in this Chapter is based on the fundamental work of Reddy *et al.* [124], but we include the thermal effects discussed in Chapter

2 up to $T = 50$ MeV. We first perform the calculations in neutrino-transparent matter, estimate the temperature and density for which we would have neutrino trapping, and, then, recalculate the same quantities using the neutrino-trapped matter composition. Besides being useful to understand the regime where we should consider trapped neutrinos, it sets the ground for the inclusion of correlation effects that will be studied in the next chapters.

3.1 Neutrino mean free path in the non interacting Fermi gas

For the sake of generality, we will rewrite the charged-current and neutral-current reactions ((3.1) and (3.3), respectively) as

$$\nu_l + N_2 \to l + N_4, \tag{3.5}$$
$$\nu_l + N_2 \to \nu_l + N_4. \tag{3.6}$$

For low-energy neutrinos, we can write the interaction Lagrangian for the reactions from Weinberg-Salam theory,

$$\mathcal{L}_{int}^{cc} = \frac{G_F C}{\sqrt{2}} l_\mu j_W^\mu \tag{3.7}$$
$$\mathcal{L}_{int}^{nc} = \frac{G_F}{\sqrt{2}} l_\mu^\nu j_Z^\mu \tag{3.8}$$

where cc and nc stand for charged current and neutral current, respectively. Here, $G_F \simeq 1.436 \times 10^{-49}$ erg cm^{-3} $= 1.16638$ MeV^{-2} is the Fermi weak coupling constant and $C = \cos\theta_c = 0.973$ the Cabibbo factor. The lepton and nucleon weak charged currents are [1]

$$l_\mu = \bar{\psi}_l \gamma_\mu (1 - \gamma_5) \psi_\nu, \tag{3.9}$$
$$j_Z^\mu = \bar{\psi}_4 \gamma^\mu (g_V - g_A \gamma_5) \psi_2. \tag{3.10}$$

Analogously, the nucleon neutral currents are

$$l_\mu = \bar{\psi}_\nu \gamma_\mu (1 - \gamma_5) \psi_\nu, \tag{3.11}$$
$$j_W^\mu = \frac{1}{2} \bar{\psi}_4 \gamma^\mu (c_V - c_A \gamma_5) \psi_2. \tag{3.12}$$

The value of the coupling constants depends on the reaction taking place. In Table 3.1, we show the values for the axial (g_A, c_A) and vectorial (g_V, c_V) coupling constants appearing in the relevant reactions.

In the relativistic formalism, the differential cross section for the process $1 + 2 \to 3 + 4$ is given by

$$d\sigma = \frac{1}{(2E_1)(2E_2)v_{rel}} \langle |\mathcal{M}|^2 \rangle d\phi_{34} (2\pi)^4 \delta^4 (P_1 + P_2 - P_3 - P_4), \tag{3.13}$$

[1] The spinor normalisation is assumed to be such that $\psi^l = \frac{u^l}{\sqrt{2E_l}} e^{-ip_l x}$, with the bispinors following $\bar{u}_l u_l = 2m_l$.

Reaction	Vectorial	Axial
$\nu_l + n \to l^- + p$	1	1.26
$\nu_l + n \to \nu_l + n$	-1	-1.26
$\nu_l + p \to \nu_l + p$	0.08	1.26

Table 3.1. Coupling constants for reactions (3.5) and (3.6).

where v_{rel} is the relative velocity between particles in the initial state (see,e.g., Ref. [133]), $\langle|\mathcal{M}|^2\rangle$ the squared matrix element summed over final spins and averaged over initial spins, and

$$d\phi_{34} = \frac{d^3p_3}{(2\pi)^3 2E_3}\frac{d^3p_4}{(2\pi)^3 2E_4}(1-f_3)(1-f_4). \tag{3.14}$$

The inverse collision mean free path is given by

$$\frac{1}{\lambda(E_1)} = \int \langle \varrho_2 v_{rel} d\sigma\rangle = 2\int \frac{d^3p_2}{(2\pi)^3} f_2 v_{rel} \int d\sigma \tag{3.15}$$

$$= 2\int \frac{d^3p_2}{(2\pi)^3}\int \frac{d^3p_3}{(2\pi)^3}\int \frac{d^3p_4}{(2\pi)^3}(2\pi)^4\delta^4(P_1+P_2-P_3-P_4)W_{fi} \times f_2(E_2)(1-f_3(E_3))(1-f_4(E_4)), \tag{3.16}$$

where the factor 2 in front of the integrals is due to the spin degeneracy of particle 2, W_{fi} is the transition rate

$$W_{fi} = \frac{\langle|\mathcal{M}|^2\rangle}{2^4 E_1 E_2 E_3 E_4} \tag{3.17}$$

In these expressions, E_i, P_i, and f_i are the energy, 4-momentum, and Fermi distribution, respectively, of particle i. The transition rate *in vacuum* for both neutral- and charged-current reactions can be expressed as [124]

$$\begin{aligned} W_{fi} = G_F^2[&(\mathcal{V}+\mathcal{A})^2(1-v_2\cos\theta_{12})(1-v_4\cos\theta_{34}) \\ &+ (\mathcal{V}-\mathcal{A})^2(1-v_2\cos\theta_{23})(1-v_4\cos\theta_{14}) \\ &- (\mathcal{V}^2-\mathcal{A}^2)\frac{m^2}{E_2E_4}(1-\cos\theta_{13})], \end{aligned} \tag{3.18}$$

where m is the bare nucleon mass. $\mathcal{V}$ and $\mathcal{A}$ correspond to Cg_V and Cg_A in the case of charged-current reactions, and to $c_V/2$ and $c_A/2$ for neutral-current reactions. The particle velocities are $v_i = p_i/E_i$ and the angle between momentum vectors $\mathbf{p}_i$ and $\mathbf{p}_j$ is θ_{ij}.

According to our nuclear dynamics, nucleons can be treated as non relativistic. In this case, the nucleon velocities $v_i \ll 1$ and can be neglected in Eq. (3.19) and we have

$$W_{fi} = G_F^2[2\mathcal{V}^2 + 2\mathcal{A}^2 - (\mathcal{V}^2-\mathcal{A}^2)\frac{m^2}{E_2E_4}(1-\cos\theta_{13})]. \tag{3.19}$$

We still have left the angle between particles 1 and 3, θ_{13}. For reactions involving nucleons, this term gives a small contribution, since it is proportional to $\mathcal{V}^2 - \mathcal{A}^2$. Also, for neutrino-transparent matter (cold stars), neutrinos appear as a thermal excitation, i.e., their energy is $E_\nu \sim T$. Therefore, their energy is much smaller in comparison to the energy of the other constituents. We could safely neglect their contribution to the 3-momentum-conserving delta function in the integration and the term proportional to $\cos\theta_{13}$ would vanish. In the case of neutrino-trapped matter, this reasoning does not apply and this contribution may become non negligible. Here, for simplicity, we will neglect this term and consider W_{fi} to be

$$W_{fi} = G_F^2(\mathcal{V}^2 + 3\mathcal{A}^2). \tag{3.20}$$

Defining the 3-momentum transfer $\mathbf{q} = \mathbf{p_1} - \mathbf{p_3}$, so that $q = |\mathbf{q}|$, and the energy transfer $q_0 = E_1 - E_3$, we can rewrite the cross section in function of $S(q_0, q)$, the so-called *dynamic form factor* or *structure function*, that characterizes the *isospin response* of the system. The inverse mean free path is then

$$\frac{1}{\lambda(E_1)} = G_F^2(\mathcal{V}^2 + 3\mathcal{A}^2) \int \frac{d^3p_3}{(2\pi)^3}(1 - f_3(E_3))S(q_0, q)) \tag{3.21}$$

with

$$S(q_0, q) = 2\int \frac{d^3p_2}{(2\pi)^3} \int \frac{d^3p_4}{(2\pi)^3}(2\pi)^4\delta^4(P_1 + P_2 - P_3 - P_4)f_2(E_2)(1 - f_4(E_4)) \tag{3.22}$$

The expression 3.21 can be rewritten as a double integral in (q_0, q) space using $d^3p_3 = 2\pi q(E_3/E_1)dq_0dq$. Since E_3 ranges between 0 and ∞, the limits of q_0 are $-\infty$ and E_1. The limits of q are obtained by checking the relation $q^2 = E_1^2 + E_3^2 - 2E_1E_3\cos\theta_{13}$ for $\cos\theta_{13} = \pm 1$. Therefore, $|q_0| < q < 2E_1 - q_0$ and

$$\frac{\sigma(E_1)}{V} = \frac{G_F^2}{4\pi^2}(\mathcal{V}^2 + 3\mathcal{A}^2) \int_{-\infty}^{E_1} dq_0 \frac{E_3}{E_1}[1 - f_3(E_3)] \int_{|q_0|}^{2E_1 - q_0} dq q S(q_0, q) \tag{3.23}$$

Let us consider, as the most basic case, the scenario of non-interacting nucleons, where the response function 3.22 can be solved analytically by taking the following steps. The integral over p_4 can be performed through the use of the three-momentum delta function, such that $\mathbf{p_4} \to \mathbf{p_2} + \mathbf{q}$ and $E_4 = (\mathbf{p_2} + \mathbf{q})^2/2M$. We get

$$S(q_0, q) = \frac{1}{2\pi^2} \int d^3p_2 \delta(q_0 + E_2 - E_4)f_2(E_2)(1 - f_4(E_4)). \tag{3.24}$$

The energy delta function can be converted in a delta function involving the angle between $\mathbf{p_2}$ and $\mathbf{q}$:

$$\delta(q_0 + E_2 - E_4) = \frac{M}{p_2 q}\delta(\cos\theta - \cos\theta_0)\Theta(p_2^2 - p_-^2), \tag{3.25}$$

where

$$\cos\theta_0 = \frac{M}{p_2 q}\left(q_0 - \frac{q^2}{2M}\right), \quad p_-^2 = \frac{M^2}{q^2}\left(q_0 - \frac{q^2}{2M}\right). \tag{3.26}$$

To get this relation, we used the identity

$$\delta(g(x)) = \sum_i \frac{\delta(x - x_i)}{|g'(x_i)|} \tag{3.27}$$

and imposed the condition that $-1 < \cos\theta_0 < 1$ through the Heaviside step function. Substituting these results into the response function and performing the angular integration, we get

$$S(q_0, q) = \frac{M}{\pi q} \int_{p_-}^{\infty} dp_2 p_2 f_2(E_2)(1 - f_4(E_4)). \tag{3.28}$$

We can cast this integral in closed form as

$$S(q_0, q) = \frac{M^2 T}{\pi q} \left[\frac{z}{1 - \exp\{(-z)\}} \left(1 + \frac{\xi_-}{z}\right) \right] \tag{3.29}$$

where

$$z = \frac{q_0 + \mu_2 - \mu_4}{T} \tag{3.30}$$

$$\xi_- = \ln\left(\frac{1 + \exp((e_- - \mu_2)/T)}{1 + \exp((e_- + q_0 - \mu_4)/T)} \right) \tag{3.31}$$

$$e_- = \frac{p_-^2}{2M} = \frac{1}{4} \frac{(q_0 - q^2/2M)^2}{q^2/2M} \tag{3.32}$$

This expression is valid for both charged- and neutral-current reactions.

This scenario is obviously oversimplified, but can give important insights about the behaviour of λ. In the case of matter with electrons and muons, the two neutrino flavours present different results, given that they are present in different reactions. In most merger simulations, due to numerical complications, matter is assumed to be composed only of neutrons, protons, and electrons [134]. For now, we present the first results for *npe* matter.

In Fig. 3.1, we show λ for the charged-current reaction. In neutrino-transparent matter, neutrinos are thermal and it is reasonable to assume their energy to be $E_\nu \sim T$. Indeed, in Fig. 3.1 and in the following ones, we set $E_\nu = 3T$. We can see that already at $T = 10$ MeV the value of λ suggests we should consider the presence of neutrinos in matter composition because $\lambda < R$. Also, at low temperatures, λ increases with density, a counter intuitive result. Indeed, this is non physical, given that there is no interactions among nucleons.

The comparison between the different neutral-current reactions is shown in Fig. 3.2. The shortest MFP is the one related to the charged reaction, while the neutral reaction involving neutrons is the second most important, result expected due to higher density when compared to protons.

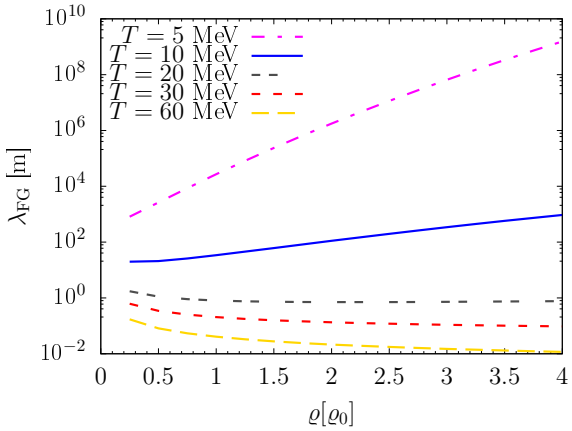

Figure 3.1. Neutrino mean free path for the charged-current reaction at different temperatures in *npe* matter.

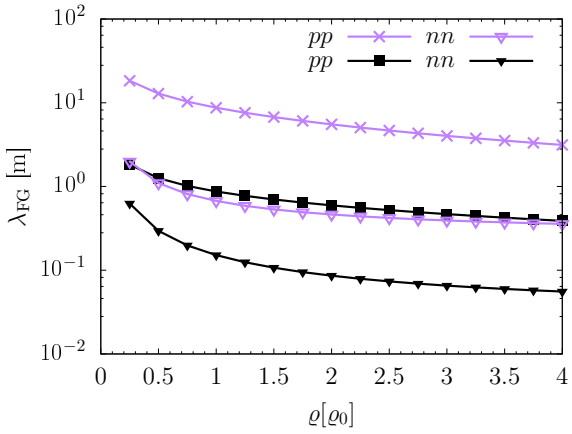

Figure 3.2. Comparison of neutrino mean free path between the different neutral-current reactions for the Fermi gas case. The purple curves correspond to $T = 30$ MeV, while the black corresponds to $T = 60$ MeV.

3.2 Calculation of neutrino mean free path: interacting matter

When considering interacting matter, the situation becomes more complicated due to the non trivial dependence of the single-particle energy on momentum. Nonetheless, as we have seen in Chapter 2, the single-particle spectrum can be efficiently parameterised by Eq. (2.93) if we consider the temperature and density dependence of $m^\star$. Indeed, with this simple, but accurate, approximation, the calculations of the response function presented in last section becomes as easy to handle as in the Fermi gas case.

The p_4 integration is the same and then the difference appears first in the energy integration. Following an analogous procedure, we can rewrite the energy delta function as

$$\delta(q_0 + E_2 - E_4) = \frac{M_4^*}{p_2 q}\delta(\cos\theta - \cos\theta_0)\Theta(E_2 - e_-)\Theta(e_+ - E_2) \tag{3.33}$$

with

$$\cos\theta_0 = \frac{M_4^*}{p_2 q}\left(c - \frac{\chi p_2^2}{2M_4^*}\right), \tag{3.34}$$

$$p_\pm^2 = \frac{2q^2}{\chi^2}\left[\left(1 + \frac{\chi m_4^* c}{q^2}\right) \pm \sqrt{1 + \frac{2\chi M_4^* c}{q^2}}\right], \tag{3.35}$$

$$E_2 = \frac{p_2^2}{2M_2^*}, \quad e_\pm = \frac{p_\pm^2}{2M_2^*}, \tag{3.36}$$

where

$$\chi = 1 - \frac{M_4^*}{M_2^*}, \quad c = q_0 + U_2 - U_4 - \frac{q^2}{2M_4^*}. \tag{3.37}$$

Note that now we have two Heaviside step functions in rewriting the energy delta function due to the two limits of p_2, $p_\pm$. With this definitions, the response function assumes the form

$$S(q_0, q) = \frac{M_2^* M_4^* T}{\pi q}\frac{\xi_- - \xi_+}{1 - exp(-z)} \tag{3.38}$$

where

$$\xi_\pm = \ln\left[\frac{1 + \exp((e_\pm - \mu_2 + U_2)/T)}{1 + \exp((e_\pm + q_0 - \mu_4 + U_2)/T)}\right]. \tag{3.39}$$

As a special case of these expressions, the neutral-current reactions have $M_2^* = M_4^*$. We get an expression almost identical to the non-interacting case, the only difference being the mean field potential added to the single-particle energy. Therefore, for the neutral-current reaction in the interacting case

$$z = \frac{q_0}{T}, \quad \mu_2 = \mu_4, \quad e_- = \frac{M_2^*}{2q^2}\left(q_0 - \frac{q^2}{2M_2^*}\right)^2, \quad e_+ = \infty \tag{3.40}$$

$$S(q_0, q) = \frac{M_2^{*2} T}{\pi q}\left[\frac{z}{1 - \exp\{(-z)\}}\left(1 + \frac{\xi_-}{z}\right)\right] \tag{3.41}$$

In Fig. 3.3 the comparison of the charged-current reaction between the Fermi gas and the interacting case is shown. In the left panel, we present the ratio $\lambda_{\rm CBF}/\lambda_{\rm FG}$, while in the right panel we show the exact value of $\lambda_{\rm CBF}$. At higher temperatures, the Fermi gas approximation works better, as expected, because thermal effects should be more relevant with respect to the interactions. At $T = 10$ MeV, there is a difference of almost 4 orders of magnitude at $4\varrho_0$. Indeed, if we see the panel on the right side, the anomalous behaviour of an increasing λ at high densities is corrected.

In Fig. 3.4 the plots show the comparison for both nn and pp neutral-current reactions. The differences between the interacting and non interacting case are much

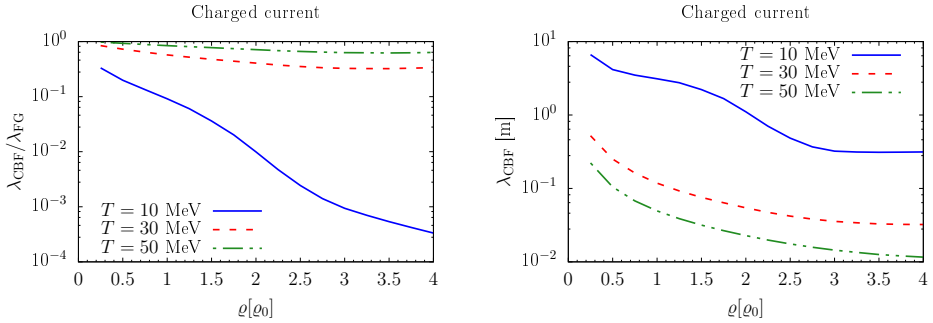

Figure 3.3. Comparison between the charged-current reaction neutrino mean free path calculated for interacting matter and for a Fermi gas.

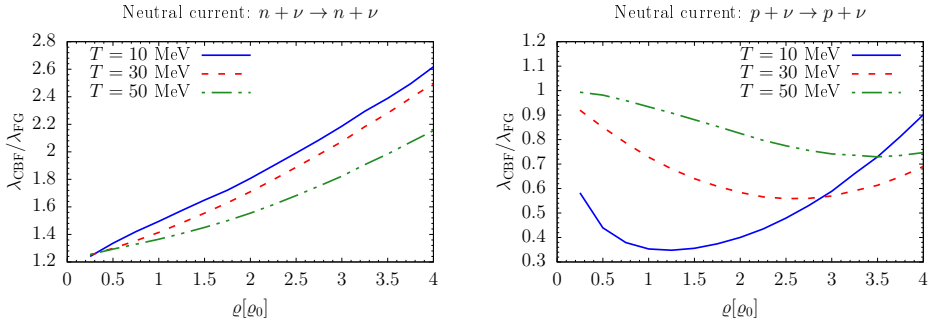

Figure 3.4. Comparison between the neutral-current reaction neutrino mean free path calculated for interacting matter and for a Fermi gas.

smaller in comparison to the charged-current reaction. It is interesting to see that for $n\nu n\nu$, λ increases when turning on the interactions. For $p\nu p\nu$, it depends on the density.

Despite being simple, we expect the results in the effective mass approximation, taking into account the density-temperature dependence, to give an accurate estimate of λ. Moreover, we can use these results as a proxy to estimate when we should consider neutrinos as trapped in the determination of chemical equilibrium. From Fig. 3.3, it appears that $T = 10$ MeV seems to be a reasonable temperature threshold $T_{\rm tr}$, in agreement with Ref. [135]. For $T < 10$ MeV, we could also have trapping for higher densities, but we assume $T_{\rm tr} = 10$ MeV for simplicity.

3.3 Beta equilibrium with neutrinos

Accounting for neutrinos in beta equilibrium means that we cannot neglect their chemical potential, such that Eq. (2.91) is modified. In charge-neutral beta-stable

$npe\mu\nu_e\bar{\nu}_e\nu_\mu\bar{\nu}_\mu$, the conditions to be satisfied are

$$\begin{cases} \mu_p + \mu_\ell = \mu_n + \mu_{\nu_\ell}, \\ \mu_{\nu_\ell} = -\mu_{\bar{\nu}_\ell}, \\ Y_p = 1 - Y_n, \\ Y_p = Y_e + Y_\mu, \\ Y_e + Y_{\nu_e} - Y_{\bar{\nu}_e} = Y_{L_e}, \\ Y_\mu + Y_{\nu_\mu} - Y_{\bar{\nu}_\mu} = Y_{L_\mu}. \end{cases}$$

The first two equations come from chemical equilibrium, the third from the conservation of baryon number, the fourth from local charge neutrality, the fifth and the sixth from the conservation of lepton number. Once we have fixed the density, temperature, and the lepton fractions Y_{L_e} and Y_{L_μ}, we are able to solve the system of equations. Note that the values of Y_L depend on the astrophysical system being analysed. In merger conditions [136], typical values are $Y_{L_e} = Y_{L_\mu} = 0.1$, while, for proto-neutron stars and supernovae [68], $Y_{L_e} = 0.4$ and $Y_{L_\mu} = 0$. Of course, the precise values depend on the evolution stage of the compact object, as well. Here, we assume these values as examples.

The calculation of the neutrino (and antineutrino) chemical potential follows the same procedure as the one for electrons, i.e., non interacting leptons; the only difference would be their mass set to zero. Let us start by the PNS composition, due to its simplicity. In Fig. 3.5 we present the matter composition of nucleons and charged leptons at $T = 10$ and 50 MeV (left and right, respectively). When comparing the two panels, it is visible that temperature plays an important in the appearance of muons. At $T = 10$ MeV, the muon fraction is too small and therefore does not considerably change Y_p. Also, their production threshold is around $1.5\varrho_0$. In Fig. 3.6, we show the net electron-neutrino fraction $Y_\nu = Y_{\nu_e} - Y_{\bar{\nu}_e}$. Increasing the temperature from $T = 10$ MeV to $T = 50$ MeV slightly changes the net neutrino fraction. Our results qualitatively agree with the ones from Ref. [137]. Also, for the sake of completeness, we present the effects of changing the temperature for the proton fraction in Fig. 3.7. In addition to changing the values of Y_p, we can also see that the convexity of the curve changes, analogously to the case without trapped neutrinos.

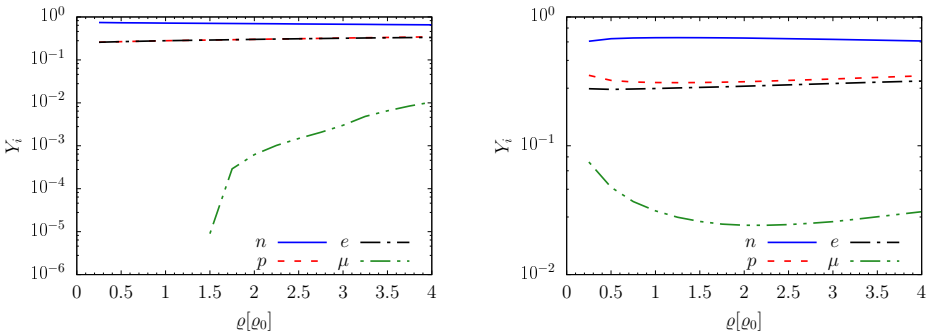

Figure 3.5. Matter composition of nucleons and charged leptons at $T = 10$ and 50 MeV (left and right, respectively) for the PNS scenario, that is, with $Y_{L_e} = 0.4$ and $Y_{L_\mu} = 0$.

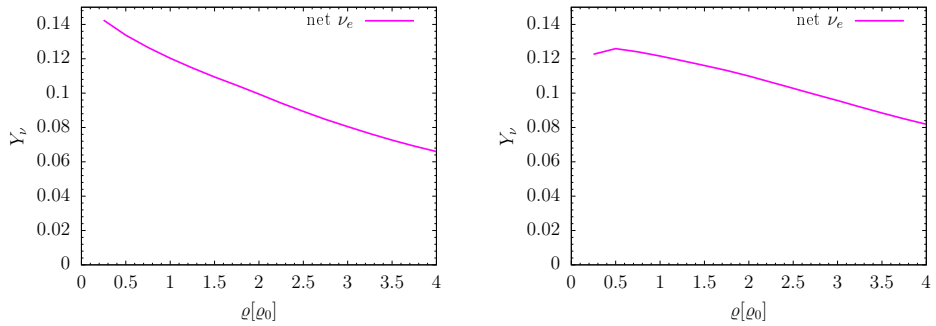

Figure 3.6. Net electron-neutrino fraction at $T = 10$ and 50 MeV (left and right, respectively) for the PNS scenario, that is, with $Y_{L_e} = 0.4$ and $Y_{L_\mu} = 0$. Increasing the temperature only slightly modifies the curves.

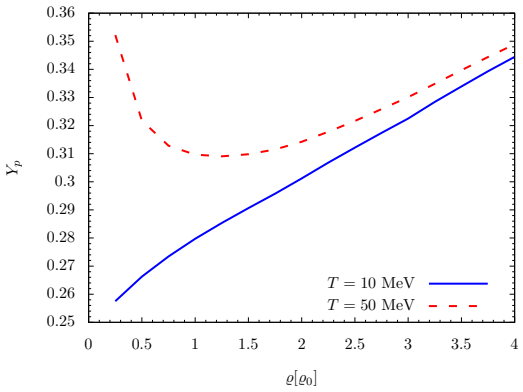

Figure 3.7. Proton fraction at $T = 10$ and 50 MeV for the PNS scenario, that is, with $Y_{L_e} = 0.4$ and $Y_{L_\mu} = 0$. We can see that increasing the temperature significantly changes the curves.

For the merger scenario, the composition is more complex due to the presence of muon neutrinos. In Fig. 3.8, we present the matter composition of nucleons and charged leptons, and in Fig. 3.9, the net neutrino fractions. We can see that the particle fractions are very different with respect to the PNS scenario. Now, even at $T = 10$ MeV, muons appear as an important constituent and, therefore, significantly changing the proton fraction. Also, the convexity of the proton fraction curve changes when we increase the temperature to $T = 50$ MeV, in contrast to the results presented in Chapter 2. Moreover, another interesting feature is the *negative* net neutrino fraction for both electron and muon flavours. A negative number means that the production of antineutrinos is favoured over the one of neutrinos. This can be understood through the observation that setting $Y_L = 0.1$ is a small number, so that, in order to follow the increase in Y_p and also Y_e (to conserve charge), we should have a negative net neutrino fraction. The same reasoning applies for the muon flavour.

As we did for the PNS scenario, in Fig. 3.10 we show how the proton fraction changes with temperature for the merger composition. The change of convexity, when going from $T = 10$ to 50 MeV is also verified here, but the most interesting feature would be the smaller Y_p in comparison to the PNS composition. This is a

consequence of a smaller Y_{L_e}, which inherently limits how much the proton fraction can grow.

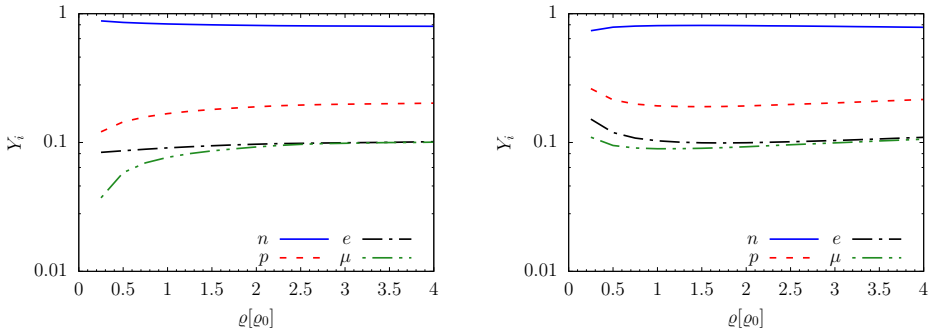

Figure 3.8. Matter composition of nucleons and charged leptons at $T = 10$ and 50 MeV (left and right, respectively) for the merger scenario, that is, with $Y_{L_e} = Y_{L_\mu} = 0.1$.

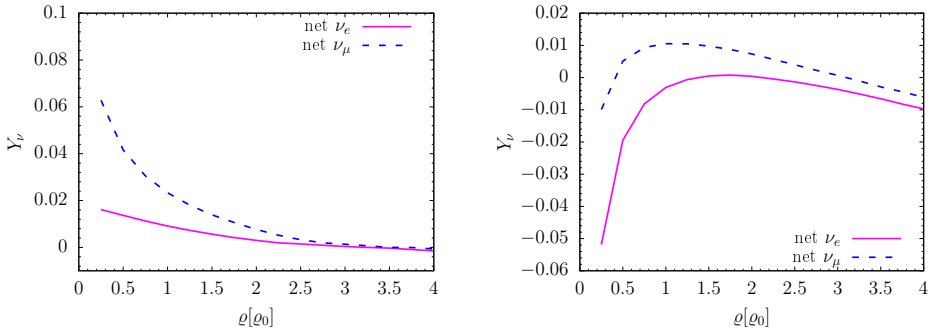

Figure 3.9. Net neutrino fractions at $T = 10$ and 50 MeV (left and right, respectively) for the merger scenario, that is, with $Y_{L_e} = Y_{L_\mu} = 0.1$. Temperature plays an important role in changing the fractions, which accompanies the changes in Fig. 3.8, specially the change of convexity of the Y_p curve.

3.4 Mean free path with trapped neutrinos

Now that we have discussed how matter composition changes when considering trapped neutrinos, we should come back to the calculation of the MFP. Trapped neutrinos would alter the calculation through the indirect change of matter composition, embedded in the Fermi distributions, and through their incoming energy. The first item can be easily solved by calculating the adequate effective masses based on the new particle fractions. For the second item, we can assume that the neutrinos would have an energy close to their Fermi surface, which would be especially reasonable at $T \lesssim 10$ MeV. In order to illustrate the changes in the MFP due to the presence of neutrinos, in Fig. 3.11 we plot the MFP associated to the charged-current reaction in *npe* matter with (assuming $Y_e = 0.1$) and without trapped neutrinos. In the left panel, we fix the neutrino energy to be $E_\nu = 3T$, while, in the right panel, $E_\nu = 3T + \mu_{\nu_e}$. The kink that appears in the right panel is a simple consequence of a neutrino fraction that goes to 0 (but the antineutrino fraction is still greater than 0).

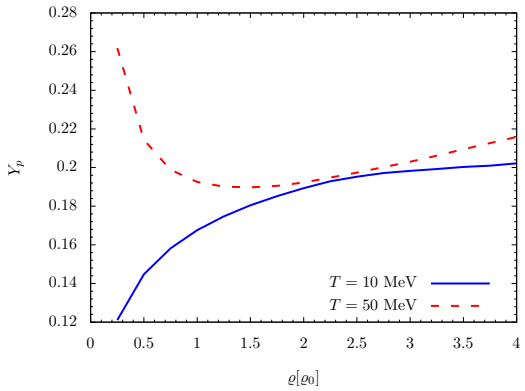

Figure 3.10. Proton fraction at $T = 10$ and 50 MeV for the merger scenario, that is, with $Y_{L_e} = Y_{L_\mu} = 0.1$.

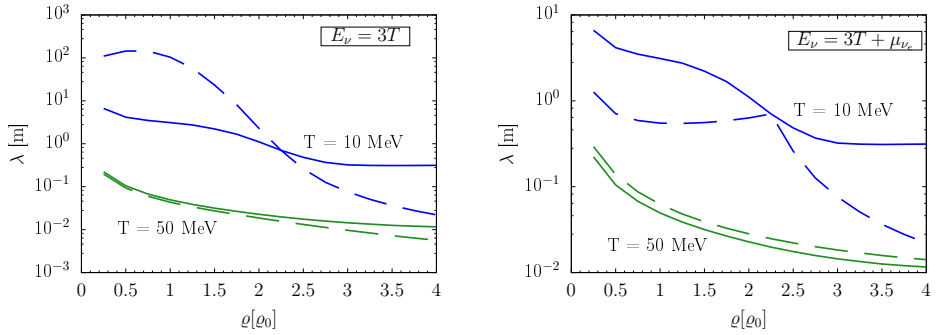

Figure 3.11. Electron-neutrino MFP in the *npe* matter with $Y_e = 0.1$ assuming two different incoming energies. For $E_\nu = 3T$, the behaviour is smooth and we can see an appreciable difference between the two curves for $T = 10$ MeV. When considering $E_\nu = 3T + \mu_{\nu_e}$, the curve presents the kink due to the chemical potential μ_{ν_e} that vanishes above $\sim 2.25\varrho_0$.

In Fig. 3.12, we display the results in the merger scenario, assuming the two different values of the neutrino energy. Adding the chemical potential contribution to E_ν significantly changes the MFP, by ~ 2 orders of magnitude. In Fig. 3.13, the difference between the two plots with different incoming energies is dramatic. There is a drop of more than 4 orders of magnitude when we increase the neutrino energy by μ_{ν_e}.

The effective mass parameterisation (2.93) appears as a useful tool to simplify the calculations, and, indeed, it is very accurate if one takes into account the dependence on temperature and density. On the other hand, the results we have shown in this chapter are referred to only mean field effects over a Fermi gas scenario. If one wants to properly include medium effects, the approach of Refs. [94, 95], for example, should be considered. It would essentially be a change of the vacuum axial and vectorial coupling constants to new ones that would be quenched due to nuclear correlations. In the next chapters, we discuss in detail this approach, establishing the relationship between the neutrino MFP and the emissivity.

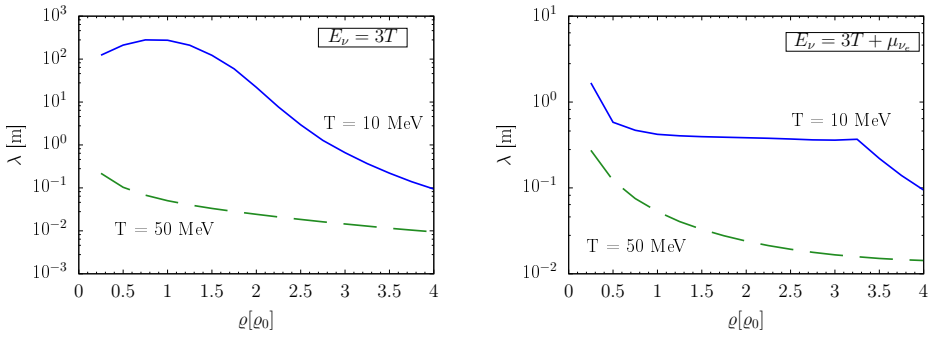

Figure 3.12. Electron-neutrino MFP in the *merger* scenario assuming two different incoming energies. For $E_\nu = 3T$, the behaviour is smooth and we can see an appreciable difference between the results for $T = 10$ MeV.

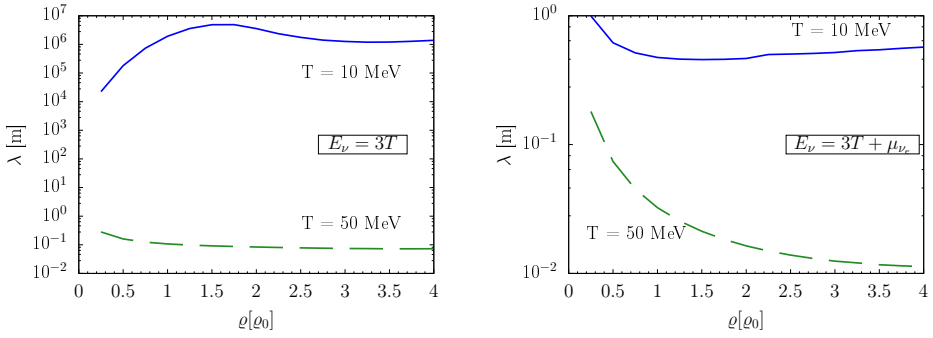

Figure 3.13. Electron-neutrino MFP in the *PNS* scenario assuming two different incoming energies. For $E_\nu = 3T$, the behaviour is smooth and we can see an appreciable difference between the results for $T = 10$ MeV.

Chapter 4

Direct URCA and nuclear correlations

Building upon the discussion of the preceding chapter, we once again emphasise that comprehending neutrino-nucleon interactions is fundamental for the description of astrophysical phenomena such as supernova explosions and the cooling of NSs and BNS mergers. From the oversimplified Fermi gas model we can already extract important information about the neutrino mean free path. A simple and straightforward way of adding dynamical effects is the mean-field approximation, in which the particles are treated as if they were moving independent of one another, with an effective mass.

The next step forward one could take would be including the effects of correlations among nucleons in the Fermi and Gamow-Teller transition amplitudes, associated with the terms in g_V and g_A of Eq. (3.10). The occurrence of sizeable correlation effects—arising from both Fermi statistics and nuclear forces—was first discussed in Refs. [138, 139].

In Ref. [92], the authors discussed the quenching of weak interactions in cold nuclear matter with arbitrary proton fraction. In Ref. [93], the neutrino mean free path in cold isospin-symmetric nuclear matter was determined by analysing the weak response. Both studies have been carried out using a CBF effective interaction derived considering the contribution of two-nucleon clusters and a nuclear Hamiltonian that solely encompasses two-nucleon interactions.

Based on the work of Ref. [93], the authors of Ref. [105] improved the approach based on the CBF formalism by incorporating the contributions of three- and many-nucleon interactions, which are known to play a critical role in the determination of the properties of dense nuclear matter. Subsequently, the resulting effective interaction was employed in Ref. [140] to conduct a thorough examination of the impact of short- and long-range correlations on the response of isospin-symmetric nuclear matter to charged-current neutrino interactions. In Ref. [95], the CBF effective interaction has been further improved taking into account the contributions of three-nucleon clusters. In the same work, the authors calculated the density and spin-density responses of cold isospin-symmetric nuclear matter. As for the generalisation to finite temperature, the authors of Ref. [141] calculated the reaction rates and the respective response function and mean free path up to $T = 10$ MeV.

However, they did not consider thermal modifications of the single-particle spectrum, and used the same transition matrix elements obtained for the $T = 0$ case.

The temperature of a newly formed neutron star is believed to be as high as a few 10^{11} K (tens of MeV). After a time $t \sim 50$ s, however, the neutrino mean free path becomes larger than the stellar radius, and the temperature begins to decrease due to the energy loss associated with neutrino emission processes. Depending on the properties of matter in the star interior, neutrino emission remains the dominant cooling mechanism for a time varying between few weeks and $\sim 10^6$ years. At the end of this epoch the temperature is reduced to $\sim 10^8$ K, and photon emission becomes dominant. In NS mergers, temperatures are also believed to reach a few tens of MeV in some regions of the binary collision. Therefore, not only we need a proper description of the neutrino MFP, but also a clear comprehension of the neutrino emissivity in these systems.

As pointed out in the previous chapter, the dUrca reaction is the most powerful, and leads to a rapid cooling of the emitting star. However, when analysing the low-temperature limit, one finds a strict density threshold for the activation of this mechanism, originating from the requirement of momentum conservation. In this limit, fermions are known to be close to their Fermi surfaces, so that there is a narrow region around $k = k_F$ that would represent their possible momentum values. This can be clearly understood from Figs. 2.5. When increasing the temperature, however, that is not longer true, and the strict density threshold condition is relaxed.

Calculating the exact expression for the neutrino emissivity at arbitrary temperature and density poses non trivial numerical difficulties, because the integration involves twelve dimensions, due to the presence of four particles. Nonetheless, if one takes the matrix element in vacuum 3.20, it is possible to cast the integration into a more friendly expression [135]. In addition, in the very low temperature regime, there is a well-known closed-form expression derived by Yakovlev *et al.* [122] which is widely used by the astrophysical community (see, e.g., Refs. [142–144] and references therein). It is worth mentioning that the authors of Ref. [122] also highlight the importance of renormalising the form factors g_V and g_A to take into account medium effects. However, in their work they do not take into account this correction and use the vacuum parameters.

Based on the work of Ref. [95], in this chapter we compute the neutrino emissivity associated with dUrca reactions at arbitrary temperature and proton fraction and taking in-medium effects. We are particularly interested in NS matter, so we assume charge neutrality and beta-equilibrium. The renormalisation of the weak vertex can be seen as a significant upgrade with respect to Ref. [141], due to the proper treatment of the single-particle spectrua, Fermi distributions and transition matrix elements at $T > 0$, as well as to the inclusion of three-nucleon interactions in our dynamical model. Regarding the calculation of the emissivity, we numerically compute its values for various temperature and densities, and contrast the independent particle picture, obtained from the Fermi gas model or the mean-field approximation, with the scenario in which correlations are taken into account. We connect these findings with the neutrino mean free path and provide a comprehensive discussion of the numerical techniques employed, as well as of the conditions under which the low-temperature approximation becomes invalid.

4.1 Effective weak operators

We can split the current (3.10), driving the process 3.1, into the two terms, leading to the Fermi and Gamow-Teller transitions. The former is associated with the coupling constant g_V, while the second to g_A. In a many-body system, such as nuclear matter, the non-relativistic operators describing these processes are

$$\begin{aligned} O^F_{\mathbf{q}} &= \sum_i O^F_{\mathbf{q}}(i) = g_V \sum_i e^{i\mathbf{q}\cdot\mathbf{r}_i}\tau_i^+, \\ \vec{O}^{GT}_{\mathbf{q}} &= \sum_i \vec{O}^{GT}_{\mathbf{q}}(i) = g_A \sum_i e^{i\mathbf{q}\cdot\mathbf{r}_i}\vec{\sigma}_i\tau_i^+, \end{aligned} \tag{4.1}$$

where $g_V = 1$ and $g_A = 1.26$ are the previously introduced coupling constants. The subscript i labels the particle i on which the operators are acting. We could write the non-relativistic transition operator in the unified notation

$$O^\mu_{\mathbf{q}} = (O^0_{\mathbf{q}}, \vec{O}_{\mathbf{q}}\ ) = (O^F_{\mathbf{q}}, -\vec{O}^{GT}_{\mathbf{q}}). \tag{4.2}$$

In these formulae, $\mathbf{q}$ represents the momentum delivered by the weak probe to the initial nucleon. Let us take, for instance, the reaction

$$n \to p + l + \bar{\nu}_l. \tag{4.3}$$

Here, we have $\mathbf{q} = -(\mathbf{k}_l + \mathbf{k}_{\bar{\nu}_l})$, because momentum conservation imposes $\mathbf{k}_n = \mathbf{k}_p + \mathbf{k}_l + \mathbf{k}_{\bar{\nu}_l}$. Note that the Gamow-Teller transition presents three components and we should compute them separately, as they are given by different Pauli matrices.

In many-body language, the weak transition matrix element would be given by

$$\langle \Psi_n | O_{\mathbf{q}} | \Psi_0 \rangle\,, \tag{4.4}$$

where $|\Psi_0\rangle$ and $|\Psi_n\rangle$ represent the initial and final many-body states, respectively. Also, the non-relativistic four-current can be written as

$$J = (J^0, \vec{J}\ ) = (\langle \Psi_n | O^F_{\mathbf{q}} | \Psi_0 \rangle\,, -\langle \Psi_n | \vec{O}^{GT}_{\mathbf{q}} | \Psi_0 \rangle). \tag{4.5}$$

If we neglect correlation effects, the initial and final states reduce to Slater determinants $|\Phi_0\rangle$ and $|\Phi_n\rangle$, and we recover the results usually found in the astrophysical literature.

In order to take into account correlation effects, we go back to the discussion of the CBF formalism and the cluster expansion technique. In the same fashion in which the effective interaction discussed in this Thesis has been obtained, we can define the effective weak operator $O^{\text{eff}}_{\mathbf{q}}$ through the relation

$$\langle \Phi_n | O^{\text{eff}}_{\mathbf{q}} | \Phi_0 \rangle = \frac{\langle \Phi_n | \mathcal{F}^\dagger O_{\mathbf{q}} \mathcal{F} | \Phi_0 \rangle}{\sqrt{\langle \Phi_0 | \mathcal{F}^\dagger \mathcal{F} | \Phi_0 \rangle \langle \Phi_n | \mathcal{F}^\dagger \mathcal{F} | \Phi_n \rangle}}, \tag{4.6}$$

A priori, the final state could be composed of many different correlated excited states, one particle-one hole, two particle-two hole etc. However, since the transition operator involves only one nucleon, the major contribution is expected to come from the one particle-one hole, or $1p1h$, excitations [95, 140]. Note that in any

independent-particle model, such as the Fermi gas model, only $1p1h$ excitations can be induced by Fermi and Gamow-Teller operators.

Hence, we can write our CBF matrix element as

$$\langle \Psi_{p_m;h_i}|O_{\mathbf{q}}|\Psi_0\rangle = \frac{\langle \Phi_{p_m;h_i}|\mathcal{F}^\dagger O_{\mathbf{q}}\mathcal{F}|\Phi_0\rangle}{\sqrt{\langle \Phi_0|\mathcal{F}^\dagger\mathcal{F}|\Phi_0\rangle \langle \Phi_{p_m;h_i}|\mathcal{F}^\dagger\mathcal{F}|\Phi_{p_m;h_i}\rangle}}, \tag{4.7}$$

where the labels p_m and h_i denote the particle and hole states, respectively, and include momentum, spin and isospin. In establishing the connection with Eq. (4.3), we can recognise h_i as the neutron and p_m as the proton. Thus, we are interested in analysing a many-body system where a neutron is replaced by a proton under the action of the transition operator, with the exchanged momentum given by the pair electron plus neutrino. When discussing about the emissivity, we will focus on the reaction (4.3), but the derivation of the mean free path of a neutrino participating in the process

$$\nu_l + n \to p + l \tag{4.8}$$

is the same, with the change $\mathbf{q} = \mathbf{k}_{\nu_l} - \mathbf{k}_e$.

The procedure for obtaining the effective weak operator consists of performing a cluster expansion of the numerator and denominator of the right hand side of Eq. (4.6). The smallness parameter of the expansion, providing a measure of the deviations from the system without correlations, is $f_{ij} - 1$, with the correlation functions f_{ij} from Eq. (2.48). Following Ref. [95, 145], we rewrite (4.6) as

$$\frac{\langle \Phi_{p_m;h_i}|\mathcal{F}^\dagger O_{\mathbf{q}}\mathcal{F}|\Phi_0\rangle}{\langle \Phi_0|\mathcal{F}^\dagger\mathcal{F}|\Phi_0\rangle} \cdot \frac{\sqrt{\langle \Phi_0|\mathcal{F}^\dagger\mathcal{F}|\Phi_0\rangle}}{\sqrt{\langle \Phi_{p_m;h_i}|\mathcal{F}^\dagger\mathcal{F}|\Phi_{p_m;h_i}\rangle}} \equiv R_a \cdot R_b, \tag{4.9}$$

so that it is easier to see the diagrams that cancel each other. A cluster expansion of both R_a and R_b needs to be performed, so that the order n of the series in terms of $f_{ij} - 1$ is given by

$$\langle \Psi_{p_m;h_i}|O_{\mathbf{q}}|\Psi_0\rangle^{(n)} = \sum_{l,m} R_a^{(l)} \cdot R_b^{(m)} \delta_{l+m=n}. \tag{4.10}$$

4.1.1 Cluster expansion of R_b

R_b does not involve the transition operator, so we can use the intuition we built in Chapter 2. Remember we can write the product of ttwo correlation operators as

$$\mathcal{F}^\dagger\mathcal{F} = 1 + \sum_{i<j} X^{(2)}(x_i, x_j) + \sum_{i<j<k} X^{(3)}(x_i, x_j, x_k) + \dots, \tag{4.11}$$

and, due to the symmetry of the ground state under a two-particle exchange, we have

$$\sum_{i<j<\dots} \langle \Phi_0|X^{(N)}(x_i, \dots, x_A)|\Phi_0\rangle = \frac{A!}{(A-N)!N!} \langle \Phi_0|X^{(N)}(x_1, \dots, x_A)|\Phi_0\rangle . \tag{4.12}$$

The same applies for the $1p1h$ state $\Phi_{p_m;h_i}$. Using the Slater determinant properties from Appendix C, we can extract N particles from the determinant such that

$$\begin{aligned}\langle\Phi_0|\mathcal{F}^\dagger\mathcal{F}|\Phi_0\rangle = &\sum_N \frac{1}{N!}\sum_{n_1<n_2<\ldots}\int dx_{1,\ldots,N}\mathcal{A}[\phi^*_{n_1}(x_1)\cdots\phi^*_{n_N}(x_N)]\\ &X^{(N)}(x_1,\ldots,x_N)\mathcal{A}[\phi_{n_1}(x_1)\cdots\phi_{n_N}(x_N)]\\ &=\sum_N \frac{1}{N!}\sum_{n_1,n_2,\ldots}\int dx_{1,\ldots,N}\phi^*_{n_1}(x_1)\cdots\phi^*_{n_N}(x_N)X^{(N)}(x_1,\ldots,x_N)\\ &\mathcal{A}[\phi_{n_1}(x_1)\cdots\phi_{n_N}(x_N)].\end{aligned} \tag{4.13}$$

We can rewrite this expression in such a way as to clearly see the cancellation among disconnected diagrams, following a procedure analogue to the one illustrated in Chapter 2. Let us introduce a new index $\bar{n}_i = 1,\ldots,h_i-1,h_i+1,\ldots,A$, i.e., a collection of states not including the hole state h_i. We can, then, rewrite the N-body term as

$$\begin{aligned}\langle\phi_0|\mathcal{F}^\dagger\mathcal{F}|\phi_0\rangle^{(N)} = &\sum_{\bar{n}_i}\frac{1}{N!}\int dx_{1,\ldots,N}\Big[\\ &\phi^*_{h_i}(x_1)\cdots\phi^*_{\bar{n}_N}(x_N)X^{(N)}(x_1,\ldots,x_N)\mathcal{A}[\phi_{h_i}(x_1)\cdots\phi_{\bar{n}_N}(x_N)]+\\ &\phi^*_{\bar{n}_1}(x_1)\cdots\phi^*_{h_i}(x_N)X^{(N)}(x_1,\ldots,x_N)\mathcal{A}[\phi_{\bar{n}_1}(x_1)\cdots\phi_{h_i}(x_N)]+\\ &\phi^*_{\bar{n}_1}(x_1)\cdots\phi^*_{h_i}(x_j)\cdots\phi^*_{\bar{n}_N}(x_N)X^{(N)}(x_1,\ldots,x_N)\mathcal{A}[\phi_{\bar{n}_1}(x_1)\cdots\phi_{h_i}(x_j)\cdots\phi_{\bar{n}_N}(x_N)]\Big].\end{aligned} \tag{4.14}$$

For the denominator, we can follow exactly the same procedure choosing to single out p_m from the determinants. For a given N, in the numerator we will be left with integrals involving the state h_i multiplied by terms that do not involve it. In the denominator, the same happens and the diagrams that do not involve p_m turn out to be the same as the ones in the numerator, by symmetry. We diagrammatically show the expansion of the numerator of R_b in Fig. 4.1, from which we can extract the rules

- The bare vertex arises from $\phi^*_{\bar{n}_i}(x_i)\phi_{\bar{n}_i}(x_i)$ and does not involve the hole state h_i. However, it tends to the standard vertex in the thermodynamic limit. The other vertex involves the hole state h_i and presents a loop indicating $\phi^*_{h_i}(x_i)\phi_{h_i}(x_i)$
- The bare exchange line does not involve the hole state, while the h_i exchange line indicates the presence of a term $\phi^*_{h_i}(x_i)\phi_{h_i}(x_j)$. Note that only one h_i vertex or h_i exchange line can appear in a given diagram.

In the denominator, we get the same diagrams by exchanging $h_i \leftrightarrow p_m$, so that the final expansion takes the form presented in Fig. 4.2. We can write R_b in a concise notation to indicate the expansion of Fig. 4.2

$$R_b = \sqrt{\frac{1+\sum_C(h_i)}{1+\sum_C(p_m)}}, \tag{4.15}$$

where the explicit calculation of the cluster terms appearing in this expression is left for the next sections.

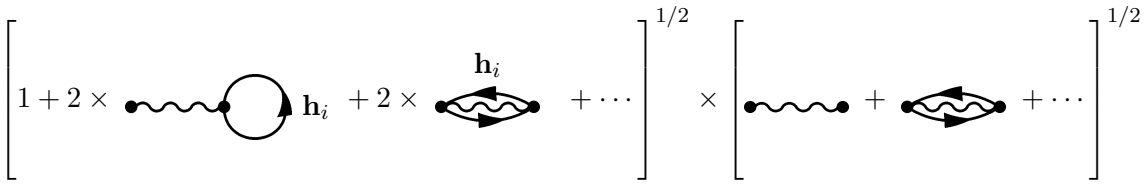

Figure 4.1. Diagrammatic representation of the cluster expansion of the numerator of R_b (4.14).

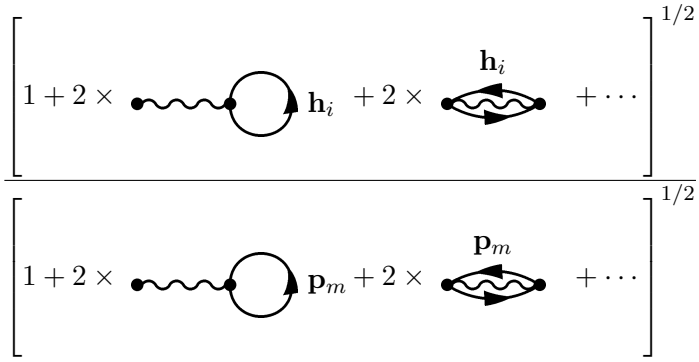

Figure 4.2. Diagrammatic representation of the net cluster expansion of R_b (4.14), after cancelling the diagrams not involving h_i nor p_m.

4.1.2 Cluster expansion of R_a

The expansion of the denominator of R_a is the same as R_b numerator's, with the only difference being the square root. The non trivial part here would be expanding the numerator of R_a, where the transition operator $O_{\mathbf{q}}$ appears. In analogy to what we have done many times, we can explore the symmetry of the $1p1h$ and ground states and write

$$\langle \Phi_{p_m;h_i} | \mathcal{F}^\dagger O_{\mathbf{q}} \mathcal{F} | \Phi_0 \rangle = A \, \langle \Phi_{p_m;h_i} | \mathcal{F}^\dagger O_{\mathbf{q}}(1) \mathcal{F} | \Phi_0 \rangle \,, \tag{4.16}$$

where the one-body operator $O_{\mathbf{q}}(1)$ acts only on particle 1. We can write the cluster expansion of $\mathcal{F}^\dagger O_{\mathbf{q}}(1)\mathcal{F}$ as

$$\mathcal{F}^\dagger O_{\mathbf{q}}(1)\mathcal{F} = O_{\mathbf{q}}(1) + \sum_{1<i} X_1^{(2)}(x_1; x_i) + \sum_{1<i<j} X_1^{(3)}(x_1; x_i, x_j) + \ldots, \tag{4.17}$$

where we single out the active particle 1, i.e., the particle at which the transition operator acts. Using the properties of minor Slater determinants discussed in Appendix C and of the antisymmetrisation operator $\mathcal{A}$, we can write (see Eq. (4.13))

$$A \, \langle \Phi_{p_m;h_i} | \mathcal{F}^\dagger O_{\mathbf{q}}(1) \mathcal{F} | \Phi_0 \rangle = \sum_N \frac{1}{(N-1)!} \sum_{\bar{n}_i} \int dx_{1,\ldots,N} \big[\tag{4.18}$$

$$\phi^*_{p_m}(x_1) \cdots \phi^*_{\bar{n}_N}(x_N) X_1^{(N)}(x_1; \ldots, x_N) \mathcal{A}[\phi_{h_i}(x_1) \cdots \phi_{\bar{n}_N}(x_N)] + \cdots +$$

$$\phi^*_{\bar{n}_1}(x_1) \cdots \phi^*_{p_m}(x_N) X_1^{(N)}(x_1; \ldots, x_N) \mathcal{A}[\phi_{\bar{n}_1}(x_1) \cdots \phi_{h_i}(x_N)] \big].$$

When using the Slater minors, one should bear in mind that the hole and particle states occupy the same "position" in the determinants, and so we can get the above expression where states involving h_i appear on the right and the ones involving p_m appear on the left.

As it happened with R_b, when we perform the expansion (4.18), we will get terms that contain particle and hole states multiplied by terms without them. The difference now, of course, will be related to the presence of the transition operator delivering momentum $\mathbf{q}$. The diagrams of this expansion can be seen in Fig. 4.3. Note that the diagrams on the right will be cancelled with the same ones coming from the denominator.

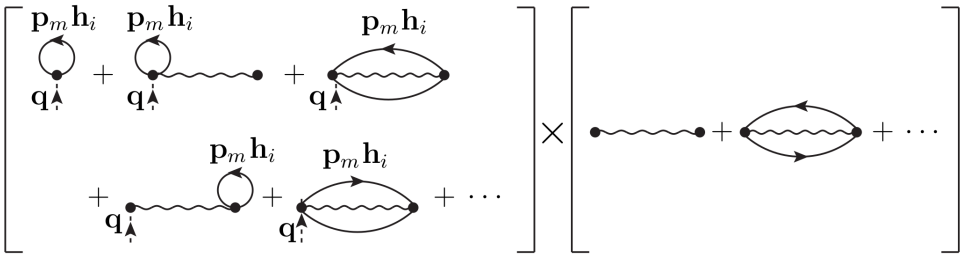

Figure 4.3. Diagrammatic representation of the cluster expansion of the numerator of R_a (4.18).

We can also write rules for the diagrams in Fig. 4.3:

- The weak transition operator $O_{\mathbf{q}}(1)$ is attached to the vertex of particle 1, delivering momentum $\mathbf{q}$, whose arrow indicates its direction.
- The bare exchange lines that appeared in the expansion of R_a also appear here, but now we emphasise they do not contain h_i nor p_m states.
- There is only one ph-exchange line, which comes as a result from $\phi^*_{p_m}(x_i)\phi^*_{h_i}(x_j)$. If $x_i = x_j$, we get the loop at the given vertex.

In analogy to Eq. (4.15), we can define the expansion of R_a as

$$R_a = \frac{\sum_C(q, p_m h_i)}{1 + \sum_C(h_i)} \tag{4.19}$$

4.1.3 Expansion of the transition matrix element

From Eqs. (4.15) and (4.19), we have

$$\langle \Psi_{p_m;h_i}|O_{\mathbf{q}}|\Psi_0\rangle = \frac{\sum_C(q, p_m h_i)}{\sqrt{1 + \sum_C(h_i)}\sqrt{1 + \sum_C(p_m)}}. \tag{4.20}$$

For the sake of claritying the notation, we can split the spin-isospin part of $O_{\mathbf{q}}$ from the momentum-dependent exponential, to obtain

$$O_{\mathbf{q}}(1) \equiv e^{i\mathbf{q}\cdot\mathbf{r}_1} O_{\sigma\tau}(1), \tag{4.21}$$

where we recognise from Eq. (4.1) that $O^F_{\sigma\tau}(1) = g_V\tau_1^+$ and $\vec{O}^{GT}_{\sigma\tau}(1) = g_A\vec{\sigma}_1\tau_1^+$.

For the expansion (4.20), we have taken into consideration first and second order corrections for the numerator and for the denominator at the two-body cluster level. Lovato *et al.* [94] have also considered first-order corrections at the three-body level for the numerator, and found that there were only two non vanishing diagrams. This is indeed the case for SNM and PNM, but for matter with $Y_p \neq Y_n$ there are other non vanishing diagrams. We have explicitly calculated their contributions to the matrix element and they have a small impact on the final values. Therefore, the results we present here are not significantly changed by adding three-body clusters to the expansion of $O_{\mathbf{q}}^{\text{eff}}$.

Zero-th order

The zero-th order term of (4.20) will be the Fermi gas result, which corresponds to approximating the denominator with unity and the numerator with its lowest contribution, i.e.

$$(\phi_{p_m;h_i}|O_{\mathbf{q}}|0)^{(0)} = A\,\langle\phi_{p_m;h_i}|O_{\mathbf{q}}(1)|\phi_0\rangle \equiv R_a^{(0)} \equiv O_N^{(0)}. \tag{4.22}$$

For the sake of clarity, let us explicitly carry out the internal product calculation, such that we have an example for the next orders. Due to the orthogonality of Slater minors, we can write

$$O_N^{(0)} = \int dx_1 \phi_{p_m}^*(x_1) O_{\mathbf{q}}(1) \phi_{h_i}(x_1), \tag{4.23}$$

where the single-particle states ϕ_i are defined by Eq. (2.4), implying that

$$\begin{aligned} O_N^{(0)} &= \frac{1}{V}\int dx_1 e^{-i(\mathbf{p}_m-\mathbf{q}-\mathbf{h}_i)\cdot\mathbf{r}_1}[\chi_{p_m}^\dagger(1)\eta_{p_m}^\dagger(1)O_{\sigma\tau}(1)\chi_{h_i}(1)\eta_{h_i}(1)] \\ &= \frac{1}{V}\int d\mathbf{r}_1 e^{-i(\mathbf{p}_m-\mathbf{q}-\mathbf{h}_i)\cdot\mathbf{r}_1}\,\langle\alpha_{p_m}|O_{\sigma\tau}(1)|\alpha_{h_i}\rangle \\ &= \delta_{\mathbf{q},\mathbf{p}_m-\mathbf{h}_i}\,\langle\alpha_{p_m}|O_{\sigma\tau}(1)|\alpha_{h_i}\rangle\,, \end{aligned} \tag{4.24}$$

where the Kronecker delta function represents the discretised momentum conservation. It is defined and related to the continuous Dirac delta through

$$\delta_{\mathbf{q},\mathbf{p}_m-\mathbf{h}_i} = \frac{1}{V}\int d\mathbf{r}_1 e^{-i(\mathbf{p}_m-\mathbf{q}-\mathbf{h}_i)\cdot\mathbf{r}_1} = \frac{(2\pi)^3}{V}\delta^{(3)}(\mathbf{h}_i+\mathbf{q}-\mathbf{p}_m) \tag{4.25}$$

In the spin-isospin matrix elements such as $\langle\alpha_{p_m}|O_{\sigma\tau}(1)|\alpha_{h_i}\rangle$, α comprehends the spin and isospin numbers of the state. Note that this is notation is completely general and could be applied to any kind of transition operator. Here, we are analysing the charged-current operators because we are interested in the dUrca reaction. In this situation, the isospin part is trivial with $\tau_{h_i} = n$ and $\tau_{p_m} = p$. The diagram corresponding to $O_N^{(0)}$ is shown in Fig. 4.4.

First order

At first order in $\hat{g}_{12} = \hat{f}_{12} - 1$, we should compute diagrams from the numerator and denominator. By expanding the expression (4.17) at the two-body level and

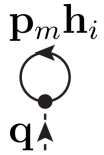

Figure 4.4. $O_N^{(0)}$ diagram given by Eq. (4.24).

keeping only the first order correction, one gets for the numerator

$$X_1^{(2)}(x_1;x_2) = \{\hat{g}_{12}, O_{\mathbf{q}}(1)\}, \tag{4.26}$$

therefore

$$O_{N_{2\mathrm{b}}}^{(1)} = \sum_{\bar{n}_i} \int dx_1 dx_2 [\phi^*_{p_m}(x_1)\phi^*_{\bar{n}_2}(x_2)\{\hat{g}_{12}, O_{\mathbf{q}}(1)\}\mathcal{A}[\phi_{h_i}(x_1)\phi_{\bar{n}_2}(x_2)] + \\ \phi^*_{\bar{n}_1}(x_1)\phi^*_{p_m}(x_2)\{\hat{g}_{12}, O_{\mathbf{q}}(1)\}\mathcal{A}[\phi_{\bar{n}_1}(x_1)\phi_{h_i}(x_2)]]. \tag{4.27}$$

This expression will give origin to four different terms, which we will call $O_{N_a}^{(1)}$, $O_{N_b}^{(1)}$, $O_{N_c}^{(1)}$ and $O_{N_d}^{(1)}$. Let us start by the first one

$$O_{N_a}^{(1)} = \sum_{\bar{n}_1} \int dx_1 dx_2 \phi^*_{\bar{n}_1}(x_1)\phi^*_{p_m}(x_2)\{\hat{g}_{12}, O_{\mathbf{q}}(1)\}\phi_{\bar{n}_1}(x_1)\phi_{h_i}(x_2) \tag{4.28}$$

$$= \frac{1}{V^2}\sum_{\bar{n}_1} \int dx_1 dx_2 e^{i\mathbf{q}\cdot\mathbf{r}_1} e^{-i(\mathbf{p}_m - \mathbf{h}_i)\cdot\mathbf{r}_2} \langle \alpha_{\bar{n}_1}\alpha_{p_m}|\{\hat{g}_{12}, O_{\sigma\tau}(1)\}|\alpha_{\bar{n}_1}\alpha_{h_i}\rangle . \tag{4.29}$$

The correlation functions depend only on the difference $\mathbf{r}_{12} = \mathbf{r}_1 - \mathbf{r}_2$, so we can perform the variable change

$$\mathbf{r}_{12} = \mathbf{r}_1 - \mathbf{r}_2, \quad \mathbf{R}_{12} = \frac{\mathbf{r}_1 + \mathbf{r}_2}{2}, \tag{4.30}$$

such that

$$O_{N_a}^{(1)} = \frac{1}{V}\delta_{\mathbf{q},\mathbf{p}_m - \mathbf{h}_i} \int d\mathbf{r}_{12} e^{i\mathbf{q}\cdot\mathbf{r}_{12}} \sum_{\bar{n}_1} \langle \alpha_{\bar{n}_1}\alpha_{p_m}|\{\hat{g}_{12}, O_{\sigma\tau}(1)\}|\alpha_{\bar{n}_1}\alpha_{h_i}\rangle . \tag{4.31}$$

This diagram and the following ones which we are going to use in our calculation converge in the thermodynamic limit, hence we can include the hole state in the sum again. In this limit, we apply (2.88) for the sum over momenta of the particle species λ. Mathematically speaking, we have

$$\sum_n = \sum_\sigma \sum_\tau \Big(\sum_{\mathbf{k}}\Big) = \sum_{\alpha_\lambda} \big(\sum_{\mathbf{k}_\lambda} n_{\mathbf{k}_\lambda}\big) \tag{4.32}$$

where the sum over $\mathbf{k}$ depends on the quantum numbers σ and τ, with λ referring to the notation introduced in Chapter 2. We can explore Eq. (2.89) and, then, obtain the result

$$O_{N_a}^{(1)} = \delta_{\mathbf{q},\mathbf{p}_m - \mathbf{h}_i} \int d\mathbf{r}_{12} e^{i\mathbf{q}\cdot\mathbf{r}_{12}} \sum_{\alpha_1} \varrho(\alpha_1) \langle \alpha_1\alpha_{p_m}|\{\hat{g}_{12}, O_{\sigma\tau}(1)\}|\alpha_1\alpha_{h_i}\rangle . \tag{4.33}$$

The same reasoning is applied to the other three diagrams arising from Eq. (4.27), but in two of them will have sums of the type

$$\sum_n e^{i\mathbf{k}_n\cdot\mathbf{r}} = \sum_\alpha \varrho(\alpha) L_\alpha(r,T), \tag{4.34}$$

where $L_\alpha(r,T)$ is the generalised Slater function (B.8). The remaining first-order two-body diagrams are

$$O^{(1)}_{N_b} = -\delta_{\mathbf{q},\mathbf{p}_m-\mathbf{h}_i}\int d\mathbf{r}_{12} e^{-i\mathbf{p}_m\cdot\mathbf{r}_{12}} \sum_{\alpha_1}\varrho(\alpha_1)L_{\alpha_1}(r,T)\left\langle\alpha_1\alpha_{p_m}|\{\hat{g}_{12},O_{\sigma\tau}(1)\}P^{\sigma\tau}_{12}|\alpha_1\alpha_{h_i}\right\rangle, \tag{4.35}$$

$$O^{(1)}_{N_c} = \delta_{\mathbf{q},\mathbf{p}_m-\mathbf{h}_i}\int d\mathbf{r}_{12} \sum_{\alpha_2}\varrho(\alpha_2)\left\langle\alpha_{p_m}\alpha_2|\{\hat{g}_{12},O_{\sigma\tau}(1)\}|\alpha_{h_i}\alpha_2\right\rangle, \tag{4.36}$$

$$O^{(1)}_{N_d} = -\delta_{\mathbf{q},\mathbf{p}_m-\mathbf{h}_i}\int d\mathbf{r}_{12} e^{-i\mathbf{h}_i\cdot\mathbf{r}_{12}} \sum_{\alpha_2}\varrho(\alpha_2)L_{\alpha_2}(r,T)\left\langle\alpha_{p_m}\alpha_2|\{\hat{g}_{12},O_{\sigma\tau}(1)\}P^{\sigma\tau}_{12}|\alpha_{h_i}\alpha_2\right\rangle. \tag{4.37}$$

For the denominator, we can identify

$$X^{(2)}(x_1,x_2) = 2\hat{g}_{12}, \tag{4.38}$$

and then we get four first-order corrections

$$O^{(1)}_{D_a} = 2\int d\mathbf{r}_{12}\sum_{\alpha_1}\varrho(\alpha_1)\left\langle\alpha_1\alpha_{p_m}|\hat{g}_{12}|\alpha_1\alpha_{p_m}\right\rangle, \tag{4.39}$$

$$O^{(1)}_{D_b} = -2\int d\mathbf{r}_{12} e^{-i\mathbf{p}_m\cdot\mathbf{r}_{12}}\sum_{\alpha_1}\varrho(\alpha_1)L_{\alpha_1}(r,T)\left\langle\alpha_1\alpha_{p_m}|\hat{g}_{12}P^{\sigma\tau}_{12}|\alpha_1\alpha_{p_m}\right\rangle, \tag{4.40}$$

$$O^{(1)}_{D_c} = 2\int d\mathbf{r}_{12}\sum_{\alpha_1}\varrho(\alpha_1)\left\langle\alpha_1\alpha_{h_i}|\hat{g}_{12}|\alpha_1\alpha_{h_i}\right\rangle, \tag{4.41}$$

$$O^{(1)}_{D_d} = -2\int d\mathbf{r}_{12} e^{-i\mathbf{h}_i\cdot\mathbf{r}_{12}}\sum_{\alpha_1}\varrho(\alpha_1)L_{\alpha_1}(r,T)\left\langle\alpha_1\alpha_{h_i}|\hat{g}_{12}P^{\sigma\tau}_{12}|\alpha_1\alpha_{h_i}\right\rangle. \tag{4.42}$$

Some comments are in order. When we use the relations (4.32) and (4.34), we are directly adding the temperature dependence to the transition matrix element. The particle densities are fixed through the conditions of beta-equilibrium at given ϱ and T, and, as we have seen in Chapter 2, they significantly change as we increase T. Furthermore, the Slater functions are properly determined by the thermodynamic consistent Fermi distributions. One could also add a temperature dependence to the correlation functions f_{12}, but, for that, the effective interaction should be derived at $T > 0$ from scratch. Direct calculations of updated correlation functions with temperatures up to 20 MeV have shown, though, that thermal corrections to f_{12} are rather small. At $T = 20$ MeV, the differences with respect to the $T = 0$ case are $\sim 3\%$ for $\varrho = \varrho_0$ in SNM [96].

Regarding the expressions presented above, we recover the results widely discussed in Refs. [94, 95, 140] in the $T \to 0$ limit. In the case of SNM or PNM, applied in these words, we can slightly simplify the calculations by noting that $\varrho_\lambda = \varrho/\nu$, with ν being the degeneracy parameter. In SNM and PNM, $\nu = 4$ and $\nu = 2$, respectively. Finally, the diagrammatic expansion of Eqs. (4.33), (4.35) and (4.39) can be found in Figs. 4.5 and 4.6.

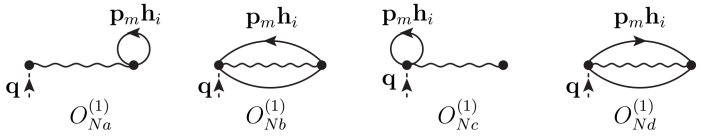

Figure 4.5. First order diagrams contributing to the numerator in Eq. (4.20).

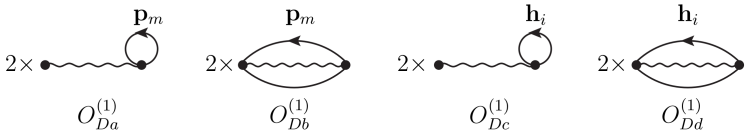

Figure 4.6. First order diagrams contributing to the denominator in Eq. (4.20).

Second order

The second order diagrams possess the same form of the first order ones, with the only substitution of using the next order of $X_1^{(2)}$ and $X^{(2)}$. Up to second order, we have

$$X_1^{(2)}(x_1;x_2) = \{\hat{g}_{12}, O_{\mathbf{q}}(1)\} + \hat{g}_{12}O_{\mathbf{q}}(1)\hat{g}_{12}, \tag{4.43}$$

$$X^{(2)}(x_1,x_2) = 2\hat{g}_{12} + g_{12}^2. \tag{4.44}$$

Therefore, the second-order diagrams are given by the expressions

$$O^{(2)}_{N_a} = \delta_{\mathbf{q},\mathbf{p}_m-\mathbf{h}_i}\int d\mathbf{r}_{12}e^{i\mathbf{q}\cdot\mathbf{r}_{12}}\sum_{\alpha_1}\varrho(\alpha_1)\,\langle\alpha_1\alpha_{p_m}|\hat{g}_{12}O_{\sigma\tau}(1)\hat{g}_{12}|\alpha_1\alpha_{h_i}\rangle\,., \tag{4.45}$$

$$O^{(2)}_{N_b} = -\delta_{\mathbf{q},\mathbf{p}_m-\mathbf{h}_i}\int d\mathbf{r}_{12}e^{-i\mathbf{p}_m\cdot\mathbf{r}_{12}}\sum_{\alpha_1}\varrho(\alpha_1)L_{\alpha_1}(r,T)\,\langle\alpha_1\alpha_{p_m}|\hat{g}_{12}O_{\sigma\tau}(1)\hat{g}_{12}P_{12}^{\sigma\tau}|\alpha_1\alpha_{h_i}\rangle\,, \tag{4.46}$$

$$O^{(2)}_{N_c} = \delta_{\mathbf{q},\mathbf{p}_m-\mathbf{h}_i}\int d\mathbf{r}_{12}\sum_{\alpha_2}\varrho(\alpha_2)\,\langle\alpha_{p_m}\alpha_2|\hat{g}_{12}O_{\sigma\tau}(1)\hat{g}_{12}|\alpha_{h_i}\alpha_2\rangle\,, \tag{4.47}$$

$$O^{(2)}_{N_d} = -\delta_{\mathbf{q},\mathbf{p}_m-\mathbf{h}_i}\int d\mathbf{r}_{12}e^{-i\mathbf{h}_i\cdot\mathbf{r}_{12}}\sum_{\alpha_2}\varrho(\alpha_2)L_{\alpha_2}(r,T)\,\langle\alpha_{p_m}\alpha_2|\hat{g}_{12}O_{\sigma\tau}(1)\hat{g}_{12}P_{12}^{\sigma\tau}|\alpha_{h_i}\alpha_2\rangle\,, \tag{4.48}$$

and

$$O^{(2)}_{D_a} = \int d\mathbf{r}_{12}\sum_{\alpha_1}\varrho(\alpha_1)\,\langle\alpha_1\alpha_{p_m}|\hat{g}_{12}^2|\alpha_1\alpha_{p_m}\rangle\,, \tag{4.49}$$

$$O^{(2)}_{D_b} = -\int d\mathbf{r}_{12}e^{-i\mathbf{p}_m\cdot\mathbf{r}_{12}}\sum_{\alpha_1}\varrho(\alpha_1)L_{\alpha_1}(r,T)\,\langle\alpha_1\alpha_{p_m}|\hat{g}_{12}^2P_{12}^{\sigma\tau}|\alpha_1\alpha_{p_m}\rangle\,, \tag{4.50}$$

$$O^{(2)}_{D_c} = \int d\mathbf{r}_{12}\sum_{\alpha_1}\varrho(\alpha_1)\,\langle\alpha_1\alpha_{h_i}|\hat{g}_{12}^2|\alpha_1\alpha_{h_i}\rangle\,, \tag{4.51}$$

$$O^{(2)}_{D_d} = -\int d\mathbf{r}_{12}e^{-i\mathbf{h}_i\cdot\mathbf{r}_{12}}\sum_{\alpha_1}\varrho(\alpha_1)L_{\alpha_1}(r,T)\,\langle\alpha_1\alpha_{h_i}|\hat{g}_{12}^2P_{12}^{\sigma\tau}|\alpha_1\alpha_{h_i}\rangle\,. \tag{4.52}$$

The diagrammatic expression can be found in Figs. 4.7 and 4.8, whose only difference with respect to Figs. 4.5 and 4.6 is the double wavy line indicating the second order in $\hat{g}_{12}$.

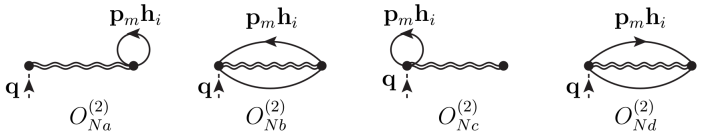

Figure 4.7. Second order diagrams contributing to the numerator in Eq. (4.20).

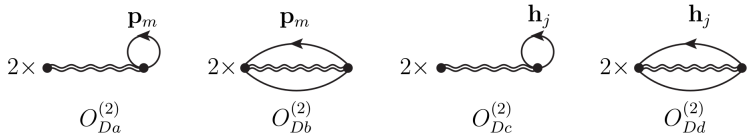

Figure 4.8. Second order diagrams contributing to the denominator in Eq. (4.20).

The effective operator employed in our study, defined by Eq.(4.6), has been obtained from Eqs. (4.7) and (4.9). The cluster terms included in the calculation of R_a and R_b are depicted in Figs. 4.5-4.8.

4.2 Thermal modifications of the transition matrix element

When analysing the effect of adding correlations to the transition operators, it is usually useful to understand how they affect the Fermi and the Gamow-Teller transitions separately. In the calculation of emissivity, when squaring the transition amplitude we have mixed terms involving different components of the GT operator, but no mixing between F and GT operators. In this section, we present results illustrating how the squared amplitude changes with respect to the Fermi gas case.

Before proceeding with that, let us discuss some features of the functions which are integrated in obtaining the first and second order corrections. To begin with, we can understand what is the relevant integration range in $r_{12} = |\mathbf{r}_{12}|$ through the panels in Fig. 2.2, keeping in mind that in the expansion we performed in the last section the deviation from the Fermi gas model are described by powers of the operator $\hat{g}_{12} = \hat{f}_{12} - 1$. By looking at Fig. 2.2, we can directly infer that the relevant range for the corrections corresponds to $r_{12} \lesssim 3$ fm. Also, the deviations from unity become more relevant as the density increases. For instance, let us fix the states h_i and p_m and the exchanged momentum $|\mathbf{q}|$. Thermal effects are introduced by modifying the Slater functions, which reflect the changes in the Fermi distributions. In Fig. 4.9, we show how the proton (left panel) and neutron (right panel) Slater functions depend on r_{12} in *npe* matter at $\varrho = \varrho_0$ and different temperatures. Note that the proton Slater function is highly sensitive to changes in temperature, which is expected due to the low proton fraction in beta-equilibrated matter. The neutron Slater functions also present a change, but it is much milder. At lower densities, the

changes are much stronger, but the density regime of interest to us would be on the higher end, because dUrca is expected to be relevant there. In Fig. 4.10, we show the results for $\varrho = 3\varrho_0$, where we can clearly see that thermal changes are less pronounced with respect to lower density scenario, although still appreciable.

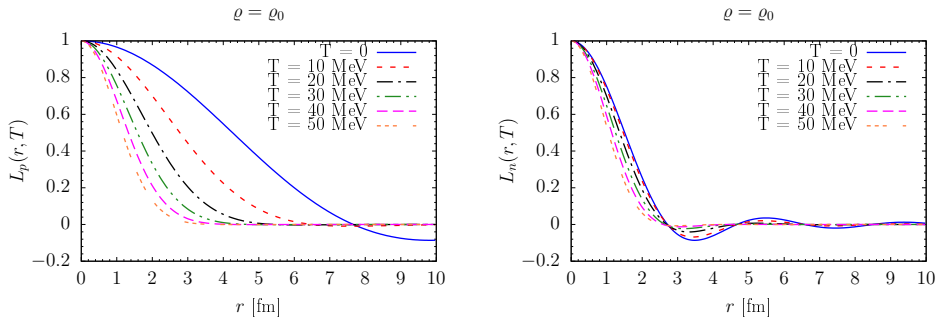

Figure 4.9. Proton (left panel) and neutron (right panel) Slater functions at $\varrho = \varrho_0$ in *npe* beta-equilibrated matter.

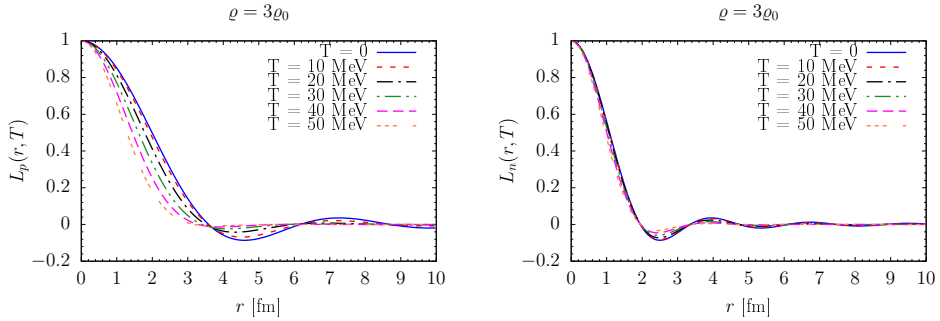

Figure 4.10. Proton (left panel) and neutron (right panel) Slater functions at $\varrho = 3\varrho_0$ in *npe* beta-equilibrated matter.

The matrix element (4.20), squared and summed over nucleon spins, enters the calculation of the emissivity and neutrino mean free path. It is therefore interesting to analyse how this quantity changes with temperature. Let us define

$$\begin{aligned}\Lambda_{\alpha\beta} &= \sum_{\text{spins}} \langle i|J_\alpha^\dagger|f\rangle \langle f|J_\beta|i\rangle \\ &= \sum_{\text{spins}} \langle 0|{O^{\text{eff}}_{\mathbf{q}\alpha}}^\dagger|\psi_{p_m;h_i}\rangle \langle \psi_{p_m;h_i}|O^{\text{eff}}_{\mathbf{q}\beta}|0\rangle\,, \end{aligned} \tag{4.53}$$

where the current J_α is defined by Eq. (4.5). For a pure Fermi and a pure Gamow-Teller transition, the relevant contributions are Λ_{00} and $\Lambda_{11}+\Lambda_{22}+\Lambda_{33}$, respectively. Obviously, there will also be the 3-momentum conserving delta function in $\Lambda_{\alpha\beta}$, but in the following we will leave it aside.

The quantity Λ depends on the momenta $\mathbf{q}$, $\mathbf{h}_i$ and $\mathbf{p}_m$. In the calculation of the emissivity associated to the process (4.3), we have $\mathbf{q} = -(\mathbf{k}_e + \mathbf{k}_{\bar{\nu}_e})$, $\mathbf{h}_i = \mathbf{k}_n$ and $\mathbf{p}_m = \mathbf{k}_p$. In order to calculate every correction term to Λ, we can choose a

coordinate system such that $\mathbf{q}$ is along the z-axis and $\mathbf{k}_e$ and $\mathbf{k}_{\bar{\nu}_e}$ lie in the xz-plane. Also, due to the momentum conservation implied by the Kronecker deltas, we will have non vanishing integrals only if $\mathbf{k}_n - \mathbf{k}_p = \mathbf{k}_e + \mathbf{k}_{\bar{\nu}_e}$; thus, $\mathbf{k}_n$ and $\mathbf{k}_p$ can be set to lie in the xz-plane without loss of generality. Here, we are going to analyse *npe* matter in beta-equilibrium without trapped neutrinos.

In the Fermi gas case, $\Lambda_{\alpha\beta}$ takes the form

$$\Lambda_{\alpha\beta} = \begin{pmatrix} 2g_V^2 & 0 & 0 & 0 \\ 0 & 2g_A^2 & 0 & 0 \\ 0 & 0 & 2g_A^2 & 0 \\ 0 & 0 & 0 & 2g_A^2 \end{pmatrix}, \tag{4.54}$$

showing that there are no off-diagonal terms. In Fig. 4.11, we show the ratio between the correlated and Fermi gas Λ_{00}, calculated fixing $\mathbf{q} = (0, 0, -k_{F_e})$, $|\mathbf{k}_n| = k_{F_n}$ and $|\mathbf{k}_p| = k_{F_p}$, as a function of the angle θ between $\mathbf{k}_n$ and the z-axis, at density $\varrho = \varrho_0$ and $3\varrho_0$. For both densities, adding correlations to the calculation leads to a quenching of the matrix elements.

At $\varrho = \varrho_0$, the temperature does affect the quenching, although only slightly. From $T = 0$ to $T = 50$ MeV, we have a variation from ~ 0.735 to ~ 0.765, that is, a variation of $\sim 4\%$. The approximate value of 0.7 agrees with the results of previous works [92, 140]. At $\varrho = 3\varrho_0$, on the other hand, the deviation with respect to the $T = 0$ curve varies with θ. It is worth noting that there is a strong dependence on θ, with a quenching varying from ~ 0.4 to ~ 0.25. This also makes sense, as the momenta we have fixed are large and, therefore, a slight change in the direction plays a more important role with respect to lower densities. Also, the fact that the quenching is stronger at $3\varrho_0$ with respect to ϱ_0 is reasonable, because nuclear correlations should play a more important role at higher densities.

In Fig. 4.12, we show the same figures, but now for the Gamow-Teller transition, i.e., $\Lambda_{11} + \Lambda_{22} + \Lambda_{33}$. As in the Fermi transition, temperature is more important at the lowest density, but now we have a more significant quenching even at $\varrho = \varrho_0$. For the sake of completeness, in Fig. 4.13 we also show the mixed term Λ_{13} at $T = 0$ and $\varrho = \varrho_0$ and $3\varrho_0$. We can clearly see, while being non vanishing, Λ_{13} is much smaller than $\Lambda_{11} + \Lambda_{22} + \Lambda_{33}$.

It should be noted that so far we have used only considerations regarding correlations and the corrections to the matrix element (4.20). When studying neutrino emissivity and mean free path, we should also take into account how the phase space changes with temperature and density. This will the subject of the discussion in the next section.

4.3 Neutrino emissivity from the dUrca process

In beta-equilibrated *npe* matter without trapped neutrinos, the emissivity expression can be written as

$$Q = 2 \int \frac{d\mathbf{k}_n}{(2\pi)^3} dW_{i\to f} E_\nu f_n (1 - f_p)(1 - f_e), \tag{4.55}$$

where $dW_{i\to f}$ is the differential probability of process (4.3) and f_i is the Fermi distribution of particle i. Note that the term $f_n(1 - f_p)(1 - f_e)$ is related to Pauli

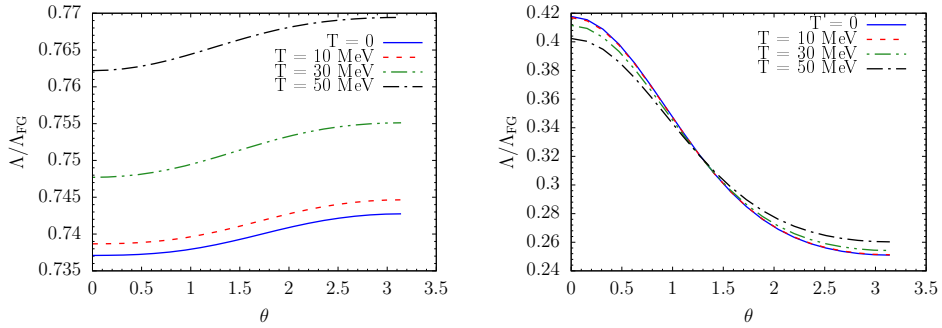

Figure 4.11. Ratio between Λ_{00} (Fermi transition), defined in Eq. (4.53) in the correlated and in the Fermi gas case. In the left and right panels, density is fixed at $\varrho = \varrho_0$ and $3\varrho_0$, respectively. Also, for both plots, we have fixed $\mathbf{q} = (0, 0, -k_{F_e})$, $|\mathbf{k}_n| = k_{F_n}$ and $|\mathbf{k}_p| = k_{F_p}$ and the horizontal axis denotes the angle between $\mathbf{k}_n$ and the z-axis.

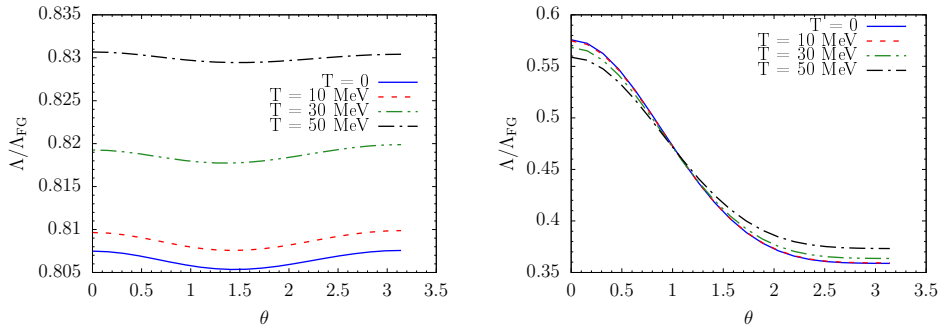

Figure 4.12. Same figure as 4.11, but now for the Gamow-Teller transition, i.e., $\Lambda_{11} + \Lambda_{22} + \Lambda_{33}$.

blocking and the factor 2 in front of the integral comes from the fact that, in beta-equilibrium, the rate of the two reactions

$$n \to p + e + \bar{\nu}_e, \tag{4.56}$$

$$p + e \to n + \nu_e \tag{4.57}$$

are the same. Hence, it is sufficient to compute the emissivity associated with the first one and, then, double the result. In the case of trapped neutrinos, one should also add a Pauli blocking factor related to $\bar{\nu}_e$ and another one to ν_e, which would be appropriate for the different reactions.

The differential probability $dW_{i\to f}$ can be otained from Fermi's golden rule

$$dW_{i\to f} = (2\pi)^4 \delta(E_n - E_p - E_e - E_\nu)\delta^{(3)}(\mathbf{k}_n - \mathbf{k}_p - \mathbf{k}_e - \mathbf{k}_\nu)\times \sum_{\text{spins}} |\mathcal{M}_{fi}|^2 \frac{d\mathbf{k}_p}{(2\pi)^3}\frac{d\mathbf{k}_e}{(2\pi)^3 2E_e}\frac{d\mathbf{k}_\nu}{(2\pi)^3 2E_\nu}, \tag{4.58}$$

where the squared transition amplitude summed over spins, $\sum_{\text{spins}} |\mathcal{M}_{fi}|^2$, is written

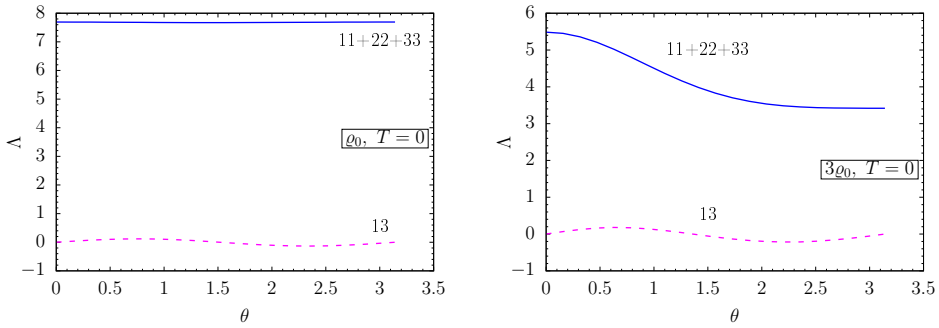

Figure 4.13. Comparison between $\Lambda_{11}+\Lambda_{22}+\Lambda_{33}$ and Λ_{13} at $T=0$, but changing the density from ϱ_0 (left panel) to $3\varrho_0$ (right panel).

from the definitions (4.5), (4.53) and (3.9)

$$\sum_{\text{spins}}|\mathcal{M}_{fi}|^2=\frac{G^2}{2}\sum_{\substack{\text{spins}\\ \text{nucleons}}}\langle i|J_\alpha^\dagger|f\rangle\langle f|J_\beta|i\rangle\sum_{\substack{\text{spins}\\ \text{leptons}}}[\bar{u}_e\gamma^\alpha(1-\gamma^5)v_\nu]^\dagger[\bar{u}_e\gamma^\beta(1-\gamma^5)v_\nu]$$
$$=\frac{G^2}{2}\Lambda_{\alpha\beta}\mathcal{L}^{\alpha\beta}, \tag{4.59}$$

with $G=G_FC$ and

$$\mathcal{L}^{\alpha\beta}=8\{k_e^\alpha k_\nu^\beta+k_e^\beta k_\nu^\alpha-(k_e\cdot k_\nu)g^{\alpha\beta}+i\epsilon^{\alpha\beta\rho\delta}k_{e\rho}k_{\nu\delta}\}, \tag{4.60}$$

where $g^{\alpha\beta}$ is the Minkowski metric tensor with signature $(1,-1,-1,-1)$ and $\epsilon^{\alpha\beta\rho\delta}$ the four-dimensional Levi-Civita symbol. Therefore, the emissivity (4.55) can be recast as

$$Q=G^2\frac{(2\pi)^4}{(2\pi)^{12}}\int d\mathbf{k}_n d\mathbf{k}_p d\mathbf{k}_e d\mathbf{k}_\nu\delta(E_n-E_p-E_e-E_\nu)\delta^{(3)}(\mathbf{k}_n-\mathbf{k}_p-\mathbf{k}_e-\mathbf{k}_\nu)$$
$$\Lambda_{\alpha\beta}\frac{\mathcal{L}^{\alpha\beta}}{4E_eE_\nu}E_\nu f_n(1-f_p)(1-f_e) \tag{4.61}$$

In this expression, $\Lambda_{\alpha\beta}$ refers to the same definition (4.53) without the 3-momentum-conserving delta function, which has been explicitly written in the integrand.

Let us proceed with the evaluation of (4.61) with the coordinate system described in the last section, i.e., with

$$\begin{aligned}\mathbf{k}_e+\mathbf{k}_\nu&=(0,0,|\mathbf{k}_e+\mathbf{k}_\nu|),\\ \mathbf{k}_e&=(k_{ex},0,k_{ez}),\\ \mathbf{k}_\nu&=(k_{\nu x},0,k_{\nu z}).\end{aligned} \tag{4.62}$$

We also have that $\Lambda_{\alpha\beta}$ is a symmetric tensor and $\Lambda_{0i}=0$. As a consequence, the contraction $\Lambda_{\alpha\beta}\mathcal{L}^{\alpha\beta}$ becomes

$$\begin{aligned}\Lambda_{\alpha\beta}\mathcal{L}^{\alpha\beta}=8\{&\Lambda_{00}(E_eE_\nu+\mathbf{k}_e\cdot\mathbf{k}_\nu)+\Lambda_{11}(E_eE_\nu+\mathbf{k}_e\cdot\mathbf{k}_\nu-2k_{ez}k_{\nu z})+\\ &\Lambda_{22}(E_eE_\nu-\mathbf{k}_e\cdot\mathbf{k}_\nu)+\Lambda_{33}(E_eE_\nu-\mathbf{k}_e\cdot\mathbf{k}_\nu+2k_{ez}k_{\nu z})+\\ &2\Lambda_{13}k_{\nu x}(k_{ez}-k_{\nu z})\}\end{aligned} \tag{4.63}$$

Note that $\Lambda_{\alpha\beta}$ depends on $\mathbf{k}_e + \mathbf{k}_\nu$ through $\mathbf{q} = -(\mathbf{k}_e + \mathbf{k}_\nu)$, so we can perform the following change of variables

$$\mathbf{k} = \mathbf{k}_e + \mathbf{k}_\nu, \tag{4.64}$$

$$\mathbf{K} = \frac{\mathbf{k}_e - \mathbf{k}_\nu}{2}, \tag{4.65}$$

such that

$$\mathbf{k}_e = \mathbf{K} + \frac{\mathbf{k}}{2}, \tag{4.66}$$

$$\mathbf{k}_\nu = -\mathbf{K} + \frac{\mathbf{k}}{2}, \tag{4.67}$$

$$\mathbf{k}_e \cdot \mathbf{k}_\nu = -K^2 + \frac{k^2}{4}, \tag{4.68}$$

and, therefore,

$$\begin{aligned}\Lambda_{\alpha\beta}\mathcal{L}^{\alpha\beta} = 2\Big[&\Lambda_{00}(4E_eE_\nu + k^2 - 4Q^2) + \Lambda_{11}(4E_eE_\nu - k^2 - 4K^2 + 8K_z^2) + \\ &\Lambda_{22}(4E_eE_\nu - k^2 + 4K^2) + \Lambda_{33}(4E_eE_\nu + k^2 + 4K^2 - 8K_z^2) + \\ &8\Lambda_{13}K_z(-2K_x)\Big].\end{aligned} \tag{4.69}$$

Defining the function $\mathcal{H}(k, K, \theta_Q)$ as

$$\mathcal{H}(k, K, \theta_Q) = \frac{1}{4E_eE_\nu}\Lambda_{\alpha\beta}\mathcal{L}^{\alpha\beta}, \tag{4.70}$$

we can recast (4.61) into

$$\begin{aligned}Q = G^2\frac{(2\pi)^4}{(2\pi)^{12}}4\pi\int(k^2dk)d\mathbf{K}d\mathbf{k}_n d\mathbf{k}_p\delta(E_n - E_p - E_e - E_\nu)\delta^{(3)}(\mathbf{k}_n - \mathbf{k}_p - \mathbf{k}) \\ \times\mathcal{H}(k, K, \theta_Q)E_\nu f_n(1 - f_p)(1 - f_e).\end{aligned} \tag{4.71}$$

Now, we can integrate over $\mathbf{k}_p$ in order to get rid of the momentum conserving delta function and setting $\mathbf{k}_p = \mathbf{k}_n - \mathbf{k}$

$$\begin{aligned}Q = G^2\frac{(2\pi)^4}{(2\pi)^{12}}4\pi\int(k^2dk)d\mathbf{K}d\mathbf{k}_n\delta(E_n - E_p - E_e - E_\nu)\mathcal{H}(k, K, \theta_Q)E_\nu \\ \times f_n(1 - f_p)(1 - f_e).\end{aligned} \tag{4.72}$$

The effective mass approximation (2.93) that we have extensively discussed in Chapter 2 and applied in Chapter 3 comes in useful now. From Fig. 2.9, we have seen that this approximation is very accurate provided we take into consideration the whole density-temperature dependence of the effective masses. Indeed, through this approximation, we expect to reproduce with great accuracy the phase space of (4.72). Furthermore, the energy-conserving delta function can be considerably simplified, as in the calculation of the neutrino mean free path described in Chapter 3. In the discussion that follows, when we refer to the Fermi gas case, we mean the

non-correlated transition matrix element, but with the above mentioned mean-field spectrum. The Fermi distributions appearing in (4.72) assume the form

$$\begin{aligned} f_p &= \frac{1}{1+e^{x_p}}, \\ f_n &= \frac{1}{1+e^{x_n}}, \\ f_e &= \frac{1}{1+e^{x_e}}, \end{aligned} \tag{4.73}$$

with

$$\begin{aligned} x_p = \frac{E_p-\mu_p}{T} &= \frac{1}{T}\Big(\frac{k_p^2}{2m_p^\star}+U_p-\mu_p\Big) \\ &= \frac{1}{T}\left(\frac{1}{2m_p^\star}(k_n^2+k^2-2k_nk\cos(\theta_n))+U_p-\mu_p\right) \end{aligned} \tag{4.74}$$

$$x_n = \frac{E_n-\mu_n}{T} = \frac{1}{T}\left(\frac{k_n^2}{2m_n^\star}+U_n-\mu_n\right) \tag{4.75}$$

$$x_e = \frac{E_e-\mu_e}{T} = \frac{1}{T}\left(\sqrt{K^2+\frac{k^2}{4}+kK\cos(\theta_K)+m_e^2}-\mu_e\right) \tag{4.76}$$

Note also that

$$E_\nu = k_\nu = \sqrt{K^2+\frac{k^2}{4}-kK\cos(\theta_K)}. \tag{4.77}$$

The energy-conserving delta function takes the form

$$\delta\Big[-\frac{1}{2m_p^\star}\Big(k_n^2+k^2-2k_nk\cos(\theta_n)\Big)+\omega\Big], \tag{4.78}$$

with

$$\omega = \frac{k_n^2}{2m_n^\star}+U_n-U_p-\sqrt{K^2+\frac{k^2}{4}+kK\cos(\theta_K)+m_e^2}-E_\nu. \tag{4.79}$$

Here, we can again use the property (3.27), assuming x to be $\cos(\theta_n)$. The new delta function will involve

$$\delta[\cos(\theta_n)-\cos(\theta_{n_0})], \tag{4.80}$$

with

$$\cos(\theta_{n_0}) = \frac{k_n^2+k^2-2m_p^\star\omega}{2k_nk} \tag{4.81}$$

and a step function to ensure that $-1 \le \cos(\theta_{n_0}) \le 1$

$$\Theta[(2k_nk)^2-(2m_p^\star\omega-k_n^2-k^2)^2]. \tag{4.82}$$

Therefore,

$$Q = G^2 \frac{4\pi(2\pi)^2}{(2\pi)^8} m_p^\star \int (k\ dk)(K^2\ \sin\theta_K\ dK\ d\theta_K)(k_n\ dk_n) \\ \Theta[(2k_n k)^2 - (2m_p^\star\omega - k_n^2 - k^2)^2]\mathcal{H}(k, K, \theta_Q)E_\nu \\ \times f_n(1-f_p)(1-f_e), \tag{4.83}$$

Expression (4.83) can be numerically calculated using an appropriate integration routine. Here, it is important to note that we have different thermal effects on the phase space and on the function $\mathcal{H}(k, K, \theta_Q)$. The effects on the latter can be understood from what we have discussed in last section, especially in Figs. 4.11 and 4.12. From these figures, we can expect thermal effects to be more relevant at lower densities, but it is important to note that these figures are valid for one specific combination of momentum values. When computing the emissivity through (4.83), however, we integrate over the whole phase space and the differences among temperatures may not be as strong as one might have expected.

Regarding the phase space effects, they can be understood using the simple Fermi gas case, without correlations. The results we have discussed in Chapter 3 used the simple mean-field approximation for the spectrum and we can already see how temperature dramatically changes the neutrino mean free path. In this case, the response function had a closed-form expression and integration could be carried out without any significant difficulties.

For the emissivity, on the other hand, the integration is more complex and some approximations have been used in the literature in order to overcome this technical issue. In particular, the so-called *phase space decomposition* [122] has been widely used to study the neutrino emissivity from neutron stars that are close to reach their final thermal state, i.e., when $T/T_F \ll 1$. By phase space decomposition, it is intended that

$$d^3k_i = m_i^\star k_{Fi} dE_i d\Omega_i, \tag{4.84}$$

where the approximation (2.93) has been used and the particle momentum is set to the Fermi momentum. When $T/T_F \ll 1$, this approximation is indeed very accurate, as particles lie close to their Fermi momentum. In the next section, we discuss how we can insert the renormalised transition matrix element into this approximation, before going to a more detailed analysis of (4.83).

4.4 Low-temperature emissivity

Let us come back to Eq. (4.61) and discuss how we can render it simpler. The typical Fermi temperature of NS matter is a few hundreds of MeV for neutrons and few tens to hundreds of MeV for protons and electrons; thus, for sufficiently low temperatures, usually $T \lesssim 1$ MeV, we can safely assume that particles have their momenta set to k_F. From Chapter 2, we have seen that equilibrium properties slightly change up to $T \lesssim 10$ MeV, however for dynamical properties these small differences in the Fermi distributions may play an important role.

For now, let us assume that we can set $k = k_F$ in in all smooth functions of energy and momentum under the integral (4.61). The energy exchange in the dUrca reaction naturally takes place in the temperature scale $\sim T$, so it is expected that neutrinos will have energy $\sim T$ in matter without trapped neutrinos. In the momentum conserving delta function, therefore, the neutrino momentum is much smaller than the other particles momenta. If we neglect $\mathbf{k}_\nu$ in the 3-momentum delta function, we then have

$$Q = G^2 \frac{(2\pi)^4}{(2\pi)^{12}} \int d\mathbf{k}_n d\mathbf{k}_p d\mathbf{k}_e d\mathbf{k}_\nu \delta(E_n - E_p - E_e - E_\nu)\delta^{(3)}(\mathbf{k}_n - \mathbf{k}_p - \mathbf{k}_e) \\ \Lambda_{\alpha\beta}\frac{\mathcal{L}^{\alpha\beta}}{4E_eE_\nu} E_\nu f_n(1-f_p)(1-f_e). \tag{4.85}$$

In other words, we assume that the neutrino does not contribute to momentum exchange between the initial and the final states. Hence, $\Lambda_{\alpha\beta}$ will depend only on $\mathbf{k}_e$. Fixing $\mathbf{k}_e$ along the z-axis, every term in $\Lambda_{\alpha\beta}\mathcal{L}^{\alpha\beta}$ that involve the direction of the neutrino momentum will vanish in the integration, such that we are left with

$$\Lambda_{\alpha\beta}\frac{\mathcal{L}^{\alpha\beta}}{4E_eE_\nu} = 2[\Lambda_{00} + (\Lambda_{11} + \Lambda_{22} + \Lambda_{33})], \tag{4.86}$$

implying, in turn,

$$Q = G^2 \frac{1}{(2\pi)^8} 8\pi \int (E_\nu^3\, dE_\nu) d\mathbf{k}_n d\mathbf{k}_p d\mathbf{k}_e \delta(E_n - E_p - E_e - E_\nu) \\ \times \delta^{(3)}(\mathbf{k}_n - \mathbf{k}_p - \mathbf{k}_e)[\Lambda_{00} + (\Lambda_{11} + \Lambda_{22} + \Lambda_{33})]. \tag{4.87}$$

In this expression, we can decompose the phase space accordingly to (4.84), yielding [1]

$$Q = G^2 \frac{1}{(2\pi)^8} 8\pi \Big(\prod_i k_{Fi} m_i^\star\Big)\langle\Lambda\rangle I_1, \tag{4.88}$$

where

$$\langle\Lambda\rangle = \int d\Omega_1 d\Omega_2 d\Omega_3 [\Lambda_{00} + (\Lambda_{11} + \Lambda_{22} + \Lambda_{33})]\delta^{(3)}(\mathbf{k}_n - \mathbf{k}_p - \mathbf{k}_e), \tag{4.89}$$

$$I_1 = \int dE_\nu E_\nu^3 \Big(\int dE_1 dE_2 dE_3 f_1(1-f_2)(1-f_3)\delta(E_1 - E_2 - E_3 - E_\nu)\Big). \tag{4.90}$$

Here, the subscripts 1, 2 and 3 refer to n, p and e, respectively.

The integral I_1 is standard [122, 146], but it is worth commenting about it. Let us change variables $x_i = (E_i - \mu_i)/T$ for the the neutron, the proton and the electron, while $x_\nu = E_\nu/T$ for the neutrino. Hence, we can write

$$I_1 = T^6 \int_0^\infty dx_\nu x_\nu^3 \int \Big(\int_{-\mu_1/T}^\infty dx_1 \\ \int_{-\mu_2/T}^\infty dx_2 \int_{-\mu_3/T}^\infty dx_3 f_1(1-f_2)(1-f_3)\delta(x_1 - x_2 - x_3 - x_\nu)\Big), \tag{4.91}$$

[1] For the electron, $m_i^\star$ is actually $\sqrt{k_{Fe}^2 + m_e^2}$.

and, by replacing $x_i \to -x_i$ and using $1 - f(x_i) = f(-x_i)$,

$$I_1 = T^6 \int_0^\infty dx_\nu x_\nu^3 \int \Big(\int_{-\mu_1/T}^{\infty} dx_1 \int_{-\infty}^{\mu_2/T} dx_2 \int_{\infty}^{\mu_3/T} dx_3 f_1 f_2 f_3 \delta(x_1 + x_2 + x_3 - x_\nu) \Big). \tag{4.92}$$

In a strongly degenerate system, such as neutron star matter at $T/T_F \ll 1$, we can approximate $\mu/T \to \infty$. In this case,

$$I_1 = T^6 I = T^6 \frac{457\pi^6}{5040}. \tag{4.93}$$

As the very first attempt, one could try analysing how temperature would affect the integration by inserting the true chemical potentials into (4.92) instead of using $\mu/T \to \infty$.

Now let us proceed with the calculation of $\langle\Lambda\rangle$. We can write the three-dimensional delta function as

$$\delta^{(3)}(\mathbf{k}_n - \mathbf{k}_p - \mathbf{k}_e) = \delta(k_p - |\mathbf{k}_n - \mathbf{k}_e|) \frac{\delta(\Omega_p - \Omega_{n-e})}{k_p^2}, \tag{4.94}$$

such that, in the integration (4.89), we have

$$\langle\Lambda\rangle = \frac{1}{k_p^2} \int d\Omega_n d\Omega_e [\Lambda_{00} + (\Lambda_{11} + \Lambda_{22} + \Lambda_{33}] \delta(k_p - |\mathbf{k}_n - \mathbf{k}_e|). \tag{4.95}$$

Now, again using (3.27), we can rewrite

$$\begin{aligned} \delta(k_p - \sqrt{k_n^2 + k_e^2 - 2k_n k_e \cos\theta_n}) =& \frac{k_p}{k_n k_e} \delta(\cos\theta_n - \frac{k_n^2 + k_e^2 - k_p^2}{2k_n k_e}) \\ & \times \Theta[(2k_n k_e)^2 - (k_n^2 + k_e^2 - k_p^2)^2], \end{aligned} \tag{4.96}$$

and, therefore,

$$\langle\Lambda\rangle = \frac{8\pi^2}{k_{Fn} k_{Fp} k_{Fe}} \Theta_{npe} [\Lambda_{00} + (\Lambda_{11} + \Lambda_{22} + \Lambda_{33})] \Big|_{k=k_F, \cos\theta_n = \cos\theta_n'} \tag{4.97}$$

where we should note that the momenta have been fixed at their Fermi momentum values and

$$\cos\theta_n' = \frac{k_{Fn}^2 + k_{Fe}^2 - k_{Fp}^2}{2k_{Fn} k_{Fe}}, \tag{4.98}$$

$$\Theta_{npe} = \Theta[k_{Fp} + k_{Fe} - k_{Fn}]. \tag{4.99}$$

Finally, we can recast (4.88) into the form

$$Q = G^2 \frac{64\pi^3}{(2\pi)^8} (m_n^\star m_p^\star m_e^\star) T^6 \frac{457\pi^6}{5040} \Lambda_{k_F} \Theta_{npe}, \tag{4.100}$$

$$\Lambda_{k_F} = [\Lambda_{00} + (\Lambda_{11} + \Lambda_{22} + \Lambda_{33})] \Big|_{k=k_F, \cos\theta_n = \cos\theta_n'} \tag{4.101}$$

At very low temperatures, we can safely take the values of Λ_{k_F} at $T = 0$. The most important feature to understand is the dependence of Λ_{k_F} on the density. There is a direct dependence through the Fermi momenta fixed at a given ϱ, but also indirectly through $\cos\theta'_n$ that depends on these, as well. As one would expect, we also have the activation threshold expressed by the Heaviside step function in (4.100). This is defined as a density threshold because the proton fraction increases with density, thus, for lower densities, it may not be large enough to yield a sufficiently large k_{Fp} (and k_{Fe}, by consequence). In order to illustrate this concept, in Fig. 4.15, we show how the ratio $(k_{Fp} + k_{Fe})/k_{Fn}$ changes with density. According to Eq. (4.100), neutrino emission through dUrca would start around $\varrho = 2.5\varrho_0$ for the temperatures presented. It should be clear, though, that the emissivity would not be exactly 0 below the threshold. It is strongly suppressed by the strict momentum conservation condition, but not exactly 0. This will be better exemplified in the next section, where we calculate the rates at different temperatures without assuming degeneracy approximations.

It is worth mentioning that, in the case of $npe\mu$ matter, the muon dUrca may be active, as well. For the muon channel, we would have the exact same expression of Eq. (4.100), with the substitution $e \to \mu$. The same density threshold reflected by the presence of the Heaviside step function in Eq. (4.99) would appear for the muon channel, that is, we would have $\Theta_{np\mu} = \Theta[k_{Fp} + k_{F\mu} - k_{Fn}]$. For the sake of completeness, in Fig. 4.14, we present the mass-radius curve obtained with the EOS employed in our work. This curve refers to $npe\mu$ matter at $T = 0$ and we highlight the point where the electron and muon dUrca set in, i.e., where above mentioned density threshold is satisfied. As we can see, for an NS of canonical mass ($1.4M_\odot$), we would have both dUrca channels open.

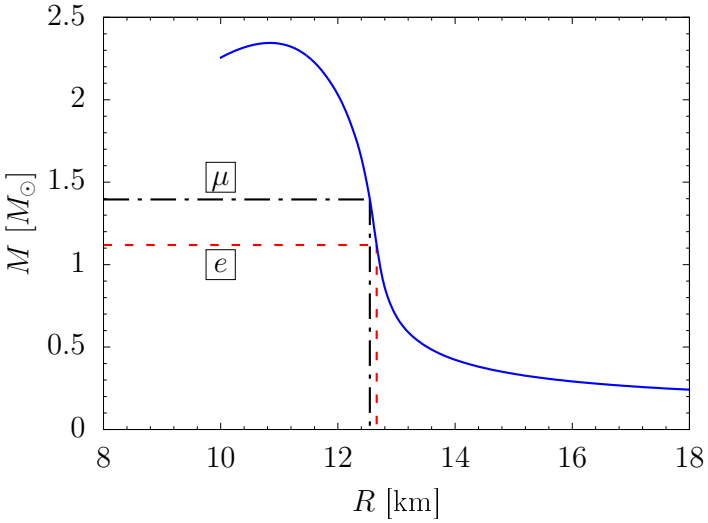

Figure 4.14. Mass-radius diagram for the $T = 0$ EOS, assuming $npe\mu$ matter. The red dashed line and black dot-dashed line refer, respectively, to the stellar configuration at which electron and muon dUrca set in.

In Fig. 4.16, we compare the results of the correlated transition matrix element with the Fermi gas case at $T = 0.1$ MeV. Also, in Fig. 4.17, we plot the ratio of the

curves shown in the former figure. It is interesting to note that the quenching of the emissivity becomes less prominent with increasing density. Close to the activation threshold, the quenching is around 50%, while at the maximum density of $4\varrho_0$, there is actual a slight increase with respect to the Fermi gas case. This behaviour can be understood from Fig. 4.18, where we plot $\Lambda_{00} + \Lambda_{11} + \Lambda_{22} + \Lambda_{33}$ as a function of theta and the density, while fixing $|\mathbf{k}_n| = k_{Fn}$, $|\mathbf{k}_p| = k_{Fp}$ and $|\mathbf{k}_e| = k_{Fe}$ for every density. There is an interplay between the angles θ'_n which are chosen from (4.98) and the way $\Lambda_{\alpha\beta}$ depends on ϱ for arbitrary θ. If we fix θ, we can see that there is a point, which happens to be around $2.5\varrho_0$, where $\Lambda_{00} + \Lambda_{11} + \Lambda_{22} + \Lambda_{33}$ reaches its minimum value. For higher densities, it starts to increase.

This result is surely intriguing and deserves further investigation. In the literature, many works have studied the correlated transition matrix element at lower densities, up to $\sim \varrho_0$. At higher densities, to the best of our knowledge, there has not been a direct calculation of an effective weak transition operator up to $4\varrho_0$. In this density regime, other mechanisms involving many-body clusters may play a role and modify the results. We emphasise that the results discussed here, while being certainly interesting in their own right, should be seen as a step towards the development of a unified description of a variety of nuclear matter properties.

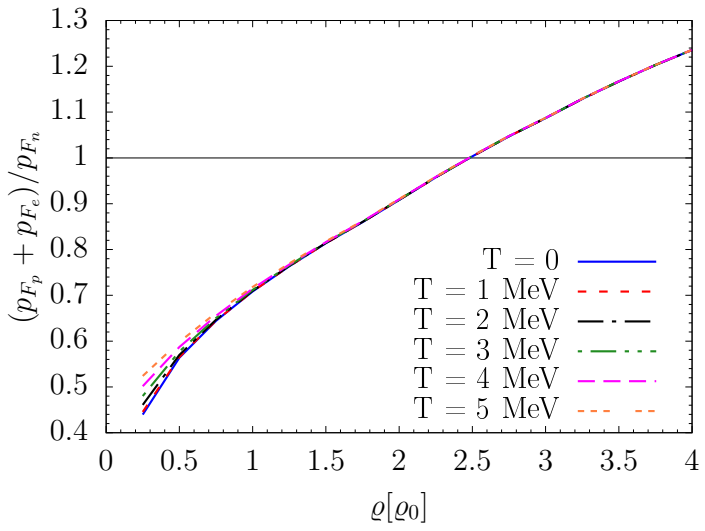

Figure 4.15. Activation threshold of the dUrca reaction at different temperatures.

4.5 Arbitrary-temperature emissivity

In the present section, we numerically solve (4.83) without using the low-temperature approximation discussed in the last section. Here, our focus will be on moderate and high temperatures, i.e., 5 MeV $\lesssim T \lesssim$ 50 MeV. As we increase the temperature, the Fermi distributions deviate more and more from the Heaviside step function; in the same way, the sharp dUrca activation threshold is expected to be smoothed out. This means that before the threshold the dUrca rate is amplified and after the threshold it is damped, with respect to the degeneracy approximation.

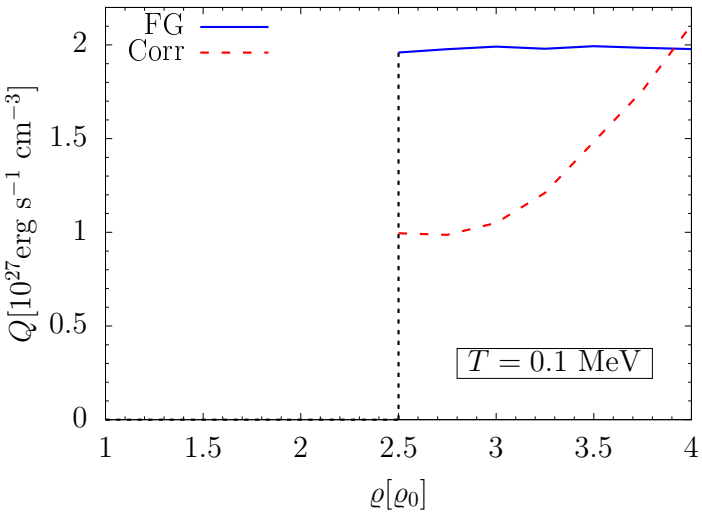

Figure 4.16. Neutrino emissivity at $T = 0.1$ MeV calculated with expression (4.100), using the correlated $\Lambda_{\alpha\beta}$ and the Fermi gas case. Note that the dUrca threshold takes place at $\varrho = 2.5\varrho_0$.

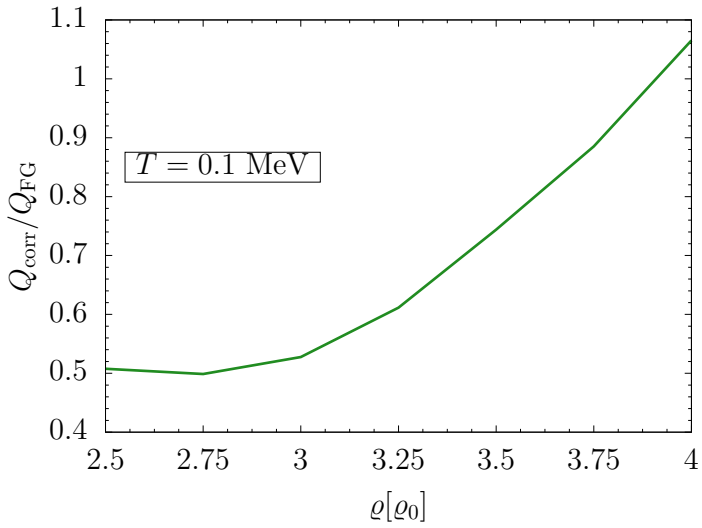

Figure 4.17. Ratio between the curves presented in Fig. 4.16, showing that the quenching of the emissivity varies significantly with density. Also, the maximum quenching takes place at $\varrho \sim 2.75\varrho_0$, right after the activation threshold.

This phenomenon is referred to as *thermal broadening* of the dUrca threshold.

Moreover, the most interesting feature of (4.100) is the temperature dependence that goes with $\propto T^6$. This strong dependence on temperature relies on the fact that, with respect to the $T = 0$ case, any small thermal excitation plays a fundamental role. At much higher temperatures, relevant to neutron star mergers and proto-neutron stars, the dynamical properties are not dictated by thermal fluctuations, given that temperature significantly influences also the equilibrium properties.

Regarding the numerical calculation of Eq. (4.83), it is expected that algorithms

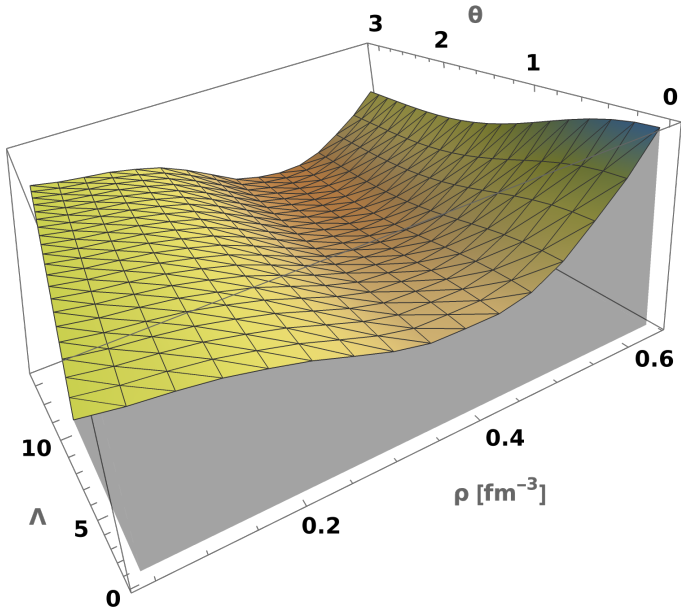

Figure 4.18. $\Lambda_{00} + \Lambda_{11} + \Lambda_{22} + \Lambda_{33}$ as a function of density and the angle θ between $\mathbf{k}_n$ and $\mathbf{k}_e$. In this plot, particles momenta have been fixed at their Fermi momentum value.

find it easier to solve the case where the temperature is higher, due to the smoothing of the Fermi distributions. At $T \lesssim 1$ MeV, they present a sharp variation around k_F and, naturally, numerical routines take much more time to converge. Also, the sharper the Fermi distribution, the worse the effective mass approximation (2.93) becomes. The latter observation comes from the fact that, in a density-temperature regime where degeneracy is extremely strong, small variations in the single-particle spectrum substantially alters the Fermi distributions' shape. From our tests, at temperatures $T \lesssim 1$ MeV, the deviation with respect to the degenerate expression (4.100) is small and the approximation turns out to be very useful by its closed-form expression.

Before proceeding to the results, let us comment about the numerical methods utilised when solving (4.83). The first feature to note is the presence of the Fermi distribution f_n, which, after a given momentum close to k_{Fn}, steeply goes to 0. When setting the numerical infinity of the k_n integration, we have chosen a momentum value such that the Fermi distribution $f_n = \{1 + \exp[(k_n^2/2m_n^\star + U_n - \mu_n)/T]\}^{-1}$ is smaller than 0.1% with respect to the value at $k_n = 0$.

The second feature to observe is the numerical infinity of $|\mathbf{k}|$. We can use the same reasoning as for the neutrons, but now we should take into account the momentum delivered by the neutrino. In what follows, we consider only *npe* matter without trapped neutrinos, so we have chosen the numerical infinity according to the same criterion described above in addition to a factor $5T$, which should account for the neutrino. For K, the numerical infinity has been set to the same value.

Regarding the numerical integration routine, we have tested a few different algorithms. The results presented here have been carried out using the Suave Monte Carlo routine from CUBA library [147]. We have used Wolfram Mathematica as

the front-end software, but the routine is implemented in C and communicates with Mathematica through a MathLink API. Suave (short for SUbregion-Adaptive VEgas) uses Vegas-like importance sampling combined with a globally adaptive subdivision strategy: until the requested accuracy is reached, the region with the largest error at the time is bisected in the dimension in which the fluctuations of the integrand are reduced most. The number of new samples in each half is prorated for the fluctuation in that half. In order to achieve accurate results, we have utilised 10^6 sampling points, setting its parameter *NMin* to 10^3. This parameter is the minimum number of samples a former pass must contribute to a subregion to be considered in that region's compound integral value. We have also tested Mathematica's Global Adaptive routine with the Gauss-Kronrod rule, i.e., a Gaussian quadrature using optimal sampling points (through polynomial interpolation) to form a weighted sum of the integrand values over these points. The Suave Monte Carlo routine turned out to be faster and with the best results, having an average absolute error of 2% for each density and temperature. Mathematica's routine yielded an average absolute error of 10% and its results agree with Suave's in the uncertainty interval.

In order to establish a baseline for comparing the correlated case with the independent-particle model, we have chosen the same integration setup with the same parameters for both scenarios. In Figs. 4.19, 4.20 and 4.21, we show the results of numerically integrating (4.83) at $T = 5,\ 10, 20$ MeV. The red dot-dashed curves represent the results assuming the correlated $\Lambda_{\alpha\beta}$, while the solid blue line is the integration with (4.54). We also report with the black dashed line the results coming from calculating (4.100).

Regardless of adding correlations or not, we can see that there is a significant deviation from the low-temperature approximation (4.100). The difference of effects when increasing the temperature in computing equilibrium and dynamical phenomena is noteworthy; in Chapter 2, we have seen that, up to $T = 10$ MeV, thermal effects were rather mild. Taking the same temperature of $T = 10$ MeV, from Fig. 4.20 we can see that there is a deviation of 3 orders of magnitude between the degenerate and the exact results at $\varrho = 2.5\varrho_0$.

At $T = 5$ MeV, the exact calculation converges to the degenerate approximation at $\varrho \approx 4\varrho_0$. At $T = 10$ MeV and $T = 20$ MeV, this convergence would happen later, according to the the curve slope. This is in agreement with the Fermi distribution behaviour, but with a much more visible effect. It is worth mentioning that the difference in orders of magnitude between $\varrho = \varrho_0$ and $\varrho = 4\varrho_0$ is larger at a lower temperature, which is a consequence of the more restricted phase space where particles can exchange momentum respecting the conservation laws.

Carrying out the same analysis we have done in the last section when discussing the degeneracy approximation, we plot in Fig. 4.22 the ratio between the correlated case and the independent-particle model. We see that the behaviour of adding correlations is approximately the same for the three values of temperature displayed, which accompanies the results presented in Figs. 4.11 and 4.12. The larger differences in this plot appear at higher densities, a result that may be a consequence of the larger proton fraction and the surpassing of the dUrca threshold.

Comments about the results are in order. We should remember that the effect of rising the temperature enters the calculation of correlations through the generalised Slater functions and the adjusted densities at $T > 0$. However, these quantities are

determined from the equilibrium properties of the system. In other words, given that temperature barely changes equilibrium properties up to $T = 10$ MeV, these effects will follow the same trend in $\Lambda_{\alpha\beta}$. On top of that, we have that momentum space is restrict due to momentum conservation at low densities. Despite having a broader region allowed, particles will mostly exchange momentum close to their Fermi values. When surpassing the dUrca threshold, although being defined at $T = 0$, the momentum conservation condition is relaxed and, naturally, these effects will enter the evaluation of $\Lambda_{\alpha\beta}$. Generally speaking, we could expect that thermal differences in the correlated results would be more prominent after the dUrca threshold, despite being present in a higher density regime.

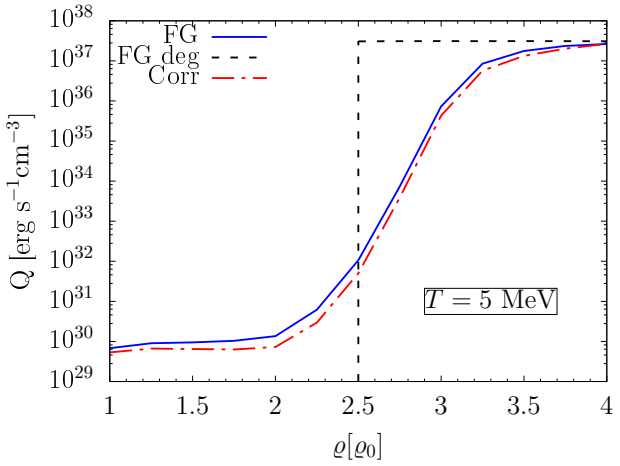

Figure 4.19. Neutrino emissivity using the correlated $\Lambda_{\alpha\beta}$ (Corr) and the Fermi gas case (4.54) (FG) at $T = 5$ MeV. In both curves, the results presented correspond to the numerical calculation of Eq. (4.83). The black dashed line (FG deg), on the other hand, corresponds to the degenerate limit, (4.100), where we see the dUrca density threshold at $2.5\varrho_0$ (please refer to Fig. 4.16).

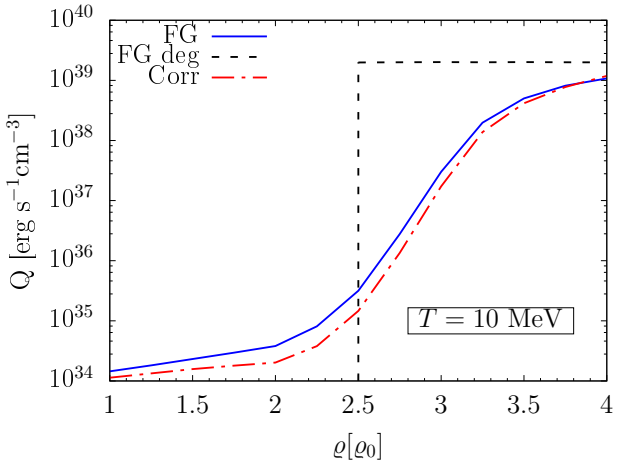

Figure 4.20. Same as figure 4.19, but at $T = 10$ MeV.

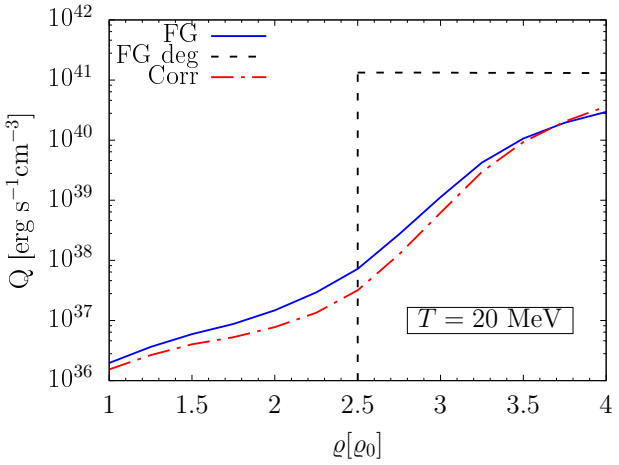

Figure 4.21. Same as figure 4.19, but at $T = 20$ MeV.

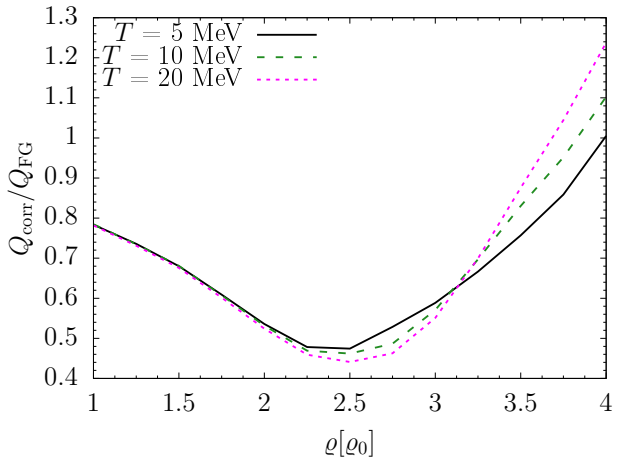

Figure 4.22. Ratio of the neutrino emissivity results using the correlated and non-correlated tensor $\Lambda_{\alpha\beta}$ at different temperatures. The results correspond to the ratios between curves "Corr" and "FG" from Fig. 4.19, 4.20 and 4.21. Note that changes due to different temperatures are more prominent at higher densities. See text for discussion.

Chapter 5

Summary and Outlook

Understanding the properties of hot nuclear matter is of paramount importance in the astrophysical scenarios of neutron star mergers and proto-neutron star evolution. In the former, extreme temperatures and densities give rise to highly non trivial phenomena, whose comprehension is essential for deciphering the dynamics of heavy element synthesis, gravitational wave emissions, and kilonovas. Similarly, in the latter scenario, the properties of hot nuclear matter dictate crucial aspects such as neutrino emission rates, cooling mechanisms, and the onset of nuclear processes. Therefore, the availability of a dynamical model strongly constrained by phenomenology and suitable for use in finite-temperature nuclear theory will be crucial. Such a model should be capable of reliably describing equilibrium and dynamical quantities.

The approach described in the first two chapters of this Thesis has been employed to obtain the EOS of matter with arbitrary neutron excess in the density region extending up to 4 ϱ_0—in which the applicability of the description in terms of nucleons is supported by electron-nucleus scattering data [5]—and temperatures up to 50 MeV. We utilised an effective interaction derived from a nuclear Hamiltonian comprising both two- and three-nucleon potentials. This effective potential can be seen as the result of a renormalisation of the bare NN potential in coordinate space; it takes into account both dynamical and statistical correlations among nucleons in the nuclear medium. The generalisation to finite temperature is obtained through a variational procedure, thermodynamically consistent by construction.

In the calculation of equilibrium properties, the most prominent feature emerging from our results is the strong interplay between temperature and density, that can be ultimately traced back to the shape of the Fermi distribution. For any given temperature, thermal effects turn out to decrease with density, although in some instances they are still significant at density as high as $\sim 4\varrho_0$. The average properties of our finite-temperature EOS clearly emerge from our plots showing the free energy, entropy, internal energy and pressure at arbitrary ϱ and T.

One should bear in mind that the discussion of temperature effects in nuclear matter should not be limited to thermal contributions to average properties. As shown by the results discussed in the first two chapters, the most fundamental properties, including the Fermi distributions, single-particle spectra and effective masses, are significantly modified at $T > 0$. A consistent inclusion of the temperature dependence of these quantities is essential to accurately describe nuclear collision

rates in matter, which in turn determine out-of-equilibrium phenomena [67, 75, 106, 117, 118, 148]. Assuming beta-equilibrium, we have seen that thermal modifications on these quantities are different for protons and neutrons. Due to a large neutron excess in beta-stable matter, protons are more sensitive to a rise in temperature, a feature that plays a role in calculating the aforementioned reactions.

As a first step towards the understanding of dynamical phenomena, in Chapter 3 we have studied the neutrino mean free path with the formalism developed by Reddy *et al.* [124]. In the calculation, we utilised the parameterisation of the particle spectra in function of the effective masses, which we had shown to be accurate at $T > 0$ if we take into account the full density-temperature dependence. The results show that there is a major difference between the Fermi gas and the interacting cases. For the charged-current reaction, the MFP in interacting matter is 1 to 4 orders of magnitude smaller with respect to the Fermi gas at $T = 10$ MeV. At $T = 30$ and 50 MeV, this difference decreases significantly. This result stems from the observation that as temperature increases, matter tends to resemble a Fermi gas more closely.

We use the initial discussion about the neutrino mean free path as a proxy to comment about neutrino trapping. The presence of trapped neutrinos in simulations is a key feature in merger simulations (see, e.g., Ref. [149] and references therein), so discussing about their presence in our EOS occurs to be extremely relevant. The exact density-temperature point for which neutrinos become trapped depends on the astrophysical regime being analysed. If we take a merger simulation, for example, temperature varies from the remnant core to its surface, thus implying that neutrinos may be trapped in some regions, but not in others. Here, we assume that the onset of trapping would happen to be when the mean free path path satisfies $\lambda \lesssim R_{\rm NS} \sim 10$ km, taking the value of λ computed in matter without the trapped neutrinos. This condition is verified for the whole density range presented in Chapter 2 at $T \gtrsim 10$ MeV, so we take $T = 10$ MeV value as the baseline.

In order to determine beta-equilibrium without trapped neutrinos, fixing a given density ϱ and temperature T is enough to solve the system of equations. When solving beta-equilibrium for neutrino-opaque matter, we should also take into account the equations of conservation of lepton number. The system of equilibrium equations, thus, depends on four inputs now: ϱ, T, Y_{L_e} and Y_{L_μ}. The lepton fractions Y_{L_e} and Y_{L_μ} have been set to typical values found in the literature for proto-neutron stars and mergers [1]. In both cases, we observe the same change of concavity in the proton fraction curve when temperature is increased that we had observed in npe and $npe\mu$ matter. In the PNS scenario, due to the high value of Y_{L_e}, the net electron-neutrino fraction turns out to be always positive, i.e., the production of neutrinos is favoured over antineutrinos'. On the other hand, in the merger scenario, the net electron- and muon-neutrino fraction become negative when temperature is increased. We also recalculated the neutrino mean free path assuming matter composition with trapped neutrinos. Apart from the clear changes in the particle fractions, incoming neutrinos (and antineutrinos) may have a much higher energy than before due to their non vanishing chemical potentials, which we have shown to have a clear impact on the final results.

[1] Note that this is just terminology. In different stages of a simulation, chemical conditions become extremely different.

In Chapter 4, we calculate the neutrino emissivity with a deeper discussion about nuclear correlation effects in the reaction (4.3). Using the same formalism presented in Chapter 2, we build an effective transition operator up to the two-body cluster level at $T > 0$. Thermal effects appear in the definition of the effective operators through the adjusted proton fractions and the generalised Slater functions. The latter are more affected at lower densities and, following the previous discussion, protons are more sensitive to $T > 0$. In the quantity $\Lambda_{\alpha\beta}$, defined in Eq. (4.53), we verify a quenching of the transition matrix density for the Fermi and Gamow-Teller transitions. This quenching turns out to be larger for the Fermi transition than for the Gamow-Teller one. Moreover, temperature appears to play a role also at higher densities, result which can be seen from Fig. 4.11 and 4.12.

The neutrino emissivity associated to the dUrca reactions has been extensively studied in literature, mostly in the regime where temperature is very low, i.e., $T \lesssim 1$ MeV. In this scenario, we can decompose the phase space using the effective mass approximation and setting $k = k_F$, which leads us to a closed-form expression. Using this approximation, which is expected to be rather reliable at low T, we have shown how inserting nuclear correlations would affect the result. We have found that the quenching of the transition matrix element is around 50% close to the dUrca activation threshold ($\sim 2.5\varrho_0$) and decreases towards $4\varrho_0$.

In the temperature range relevant to mergers and proto-neutron stars, however, we cannot rely on this low-temperature approximation. By performing numerical integration of Eq. (4.83), we have obtained the neutrino emissivity at $T = 5, 10,$ and 20 MeV, exploring scenarios with both correlated and non correlated transition matrix elements. Already at $T = 5$ MeV —a rather low temperature regarding changes in the equilibrium properties of the EOS —we can observe a large deviation with respect to the degenerate case. The convergence to the latter case would be reached right after $4\varrho_0$. At higher temperatures, clearly the convergence would be reached at larger densities.

Regarding the role of correlations, we found that the maximum quenching would happen at $\sim 2.5\varrho_0$, in the vicinity of the activation threshold, being around 50%. The ratio $Q_{\rm corr}/Q_{\rm FG}$ turns out to be similar for the three temperatures considered, in addition to the fact it agrees with the results coming from the degeneracy approximation. It is interesting to observe, however, that thermal effects in the correlated results are more prominent at higher densities, especially after the dUrca activation threshold. This can be understood as follows. At $T > 0$, the dUrca activation threshold is not well defined due to its thermal broadening; nevertheless, it is naturally expected that, above it, more particles with momenta $k > k_F$ and $k < k_F$ will be allowed to contribute to the integrand. In other words, the correlated $\Lambda_{\alpha\beta}$ will be evaluated at many more momentum points and the differences among different temperatures will be amplified.

Finally, let us discuss potential avenues for further development based on the results presented here. The calculation of the emissivity with correlations in Chapter 4 can be readily generalised to the case of matter with trapped neutrinos. Apart from the numerical details, one must recalculate all the relevant functions with updated particle fractions and only include the Pauli blocking factor $1 - f_{\bar{\nu}_e}$ in (4.83). If one wants to take into account muons in matter composition, it suffices to calculate the emissivity in the muonic channel. Moreover, the correlated weak transition matrix

element can also be readily applied to other relevant dynamical quantities depending on the reaction rate.

Regarding the renormalisation of the transition matrix element using a cluster expansion technique, we could in principle the results by adding other many-body clusters. At lower densities, though, we do not expect a large change. The addition of other three-body clusters is being carried out at the moment.

It is important to note that the effective interaction formalism employed in this Thesis is a powerful and consistent framework, well suited to study a wide variety of phenomena relevant for neutron star physics. The same analysis of equilibrium and dynamical properties discussed here is being carried out with an updated version of the present effective interaction, where the boost corrections mentioned in Chapter 1 is taken into account. Adding boost corrections could have an important impact on the quantities studied here, given that they would soften the EOS and, thus, increase the dUrca density threshold.

As a final comment, we would like to stress that the weak vertex should be renormalised also in the amplitude of the mUrca reaction. In this case, we should also care about more complex strong interaction processes, leading to modifications of the nucleon propagator. In our formalism, however, these effects turn out to of higher order in the effective interaction.

Appendix A

AV6 algebra

A.1 O^n algebra

The six operators (1.32) introduced in Chapter 1 have the very important properties of forming an algebra with respect to multiplication, as they satisfy the relations

$$O^i O^j = \sum_k K_k^{ij} O^K \ . \tag{A.1}$$

The values of K_k^{ij} can be easily found exploiting the $SU(2)$ algebra of Pauli matrices [96]. The *fundamental representation* is commonly defined choosing σ_3 in diagonal form,

$$\sigma^1 = \begin{pmatrix} 0 & 1 \\ 1 & 0 \end{pmatrix} = |\uparrow\rangle \langle\downarrow| + |\downarrow\rangle \langle\uparrow| \,, \tag{A.2}$$

$$\sigma^2 = \begin{pmatrix} 0 & -i \\ i & 0 \end{pmatrix} = -i\,|\uparrow\rangle \langle\downarrow| + i\,|\downarrow\rangle \langle\uparrow| \,, \tag{A.3}$$

$$\sigma^3 = \begin{pmatrix} 1 & 0 \\ 0 & -1 \end{pmatrix} = |\uparrow\rangle \langle\uparrow| - |\downarrow\rangle \langle\downarrow| \,, \tag{A.4}$$

where $|\uparrow\rangle$ and $|\downarrow\rangle$ represent the state with the spin projection $m_s = +1$ and $m_s = -1$, respectively. The commutation and anti-commutation relations of the Pauli matrices are

$$\begin{aligned} [\sigma_i, \sigma_j] &= 2i\epsilon_{ijk}\sigma^k \\ \{\sigma_i, \sigma_j\} &= 2\delta_{ij}. \end{aligned}$$

The same representation and identities apply to isospin space.

A.2 Two-particle system

When dealing with two-particle states, it is convenient to establish the connection between the $|m_{s1}m_{s2}\rangle$ and $|S\ M_S\rangle$ bases

$$\begin{aligned} |00\rangle &= \frac{1}{\sqrt{2}}(|\uparrow\downarrow\rangle - |\downarrow\uparrow\rangle), \\ |1-1\rangle &= |\downarrow\downarrow\rangle\,, \\ |10\rangle &= \frac{1}{\sqrt{2}}(|\uparrow\downarrow\rangle + |\downarrow\uparrow\rangle), \\ |11\rangle &= |\uparrow\uparrow\rangle\,. \end{aligned} \tag{A.5}$$

The operators $\boldsymbol{\sigma}_1 = (\sigma_1^1, \sigma_1^2, \sigma_1^3)$ and $\boldsymbol{\sigma}_2 = (\sigma_2^1, \sigma_2^2, \sigma_2^3)$ act on the particles 1 and 2, respectively. It is possible to show that

$$(\boldsymbol{\sigma}_1 \cdot \boldsymbol{\sigma}_2)^2 = 3 - 2(\boldsymbol{\sigma}_1 \cdot \boldsymbol{\sigma}_2). \tag{A.6}$$

As $(\boldsymbol{\sigma}_1 \cdot \boldsymbol{\sigma}_2)$ is a scalar quantity, we can interpret the above equation as algebraic whose solutions are $(\boldsymbol{\sigma}_1 \cdot \boldsymbol{\sigma}_2) = -3$ and $(\boldsymbol{\sigma}_1 \cdot \boldsymbol{\sigma}_2) = 1$. They correspond, respectively, to the states of total spin $S = 0$ (spin singlet channel) and $S = 1$ (spin triplet channel). With these operators, we can define projection operators

$$P_{S=0} = P_1 = \frac{1 - (\boldsymbol{\sigma}_1 \cdot \boldsymbol{\sigma}_2)}{4}, \tag{A.7}$$

$$P_{S=1} = P_3 = \frac{3 + (\boldsymbol{\sigma}_1 \cdot \boldsymbol{\sigma}_2)}{4}, \tag{A.8}$$

which project onto states of total spin $S = 0$ or $S = 1$, respectively.

The projection operators satisfy

$$P_{2S+1}\,|S'\rangle = \delta_{SS'}\,|S'\rangle\,, \tag{A.9}$$

$$P_{2S+1}^2 = P_{2S+1}, \tag{A.10}$$

$$P_1 + P_3 = 1, \tag{A.11}$$

$$P_1 P_3 = P_3 P_1 = 0. \tag{A.12}$$

Moreover, we can also define spin and isospin exchange operators based on

$$\begin{aligned} (P_3 - P_1)\,|\uparrow\uparrow\rangle &= |\uparrow\uparrow\rangle\,, \quad (P_3 - P_1)\,|\downarrow\downarrow\rangle = |\downarrow\downarrow\rangle\,, \\ (P_3 - P_1)\,|\uparrow\downarrow\rangle &= |\downarrow\uparrow\rangle\,, \quad (P_3 - P_1)\,|\downarrow\uparrow\rangle = |\uparrow\downarrow\rangle\,. \end{aligned}$$

The spin exchange operator can be defined as

$$P_\sigma\,|S\ M_S\rangle = (-)^{S+1}\,|S\ M_S\rangle\,, \tag{A.13}$$

while, for isospin,

$$P_\tau\,|T\ M_T\rangle = (-)^{T+1}\,|T\ M_T\rangle\,. \tag{A.14}$$

Combining both results, we have the spin-isospin exchange operator

$$P_{\sigma\tau} \equiv P_\sigma P_\tau = \frac{1}{4}\Big(1 + (\boldsymbol{\sigma}_1 \cdot \boldsymbol{\sigma}_2)\Big)\Big(1 + (\boldsymbol{\tau}_1 \cdot \boldsymbol{\tau}_2)\Big), \tag{A.15}$$

with

$$P_{\sigma\tau}\,|S\ M_S, T\ M_T\rangle = (-)^{S+T}\,|S\ M_S, T\ M_T\rangle \tag{A.16}$$

A.3 The tensor operator S_{12}

Let us now turn to the tensor operator S_{12}, defined as

$$S_{12} \equiv \frac{3}{r^2}(\boldsymbol{\sigma}_1 \cdot \mathbf{r})(\boldsymbol{\sigma}_2 \cdot \mathbf{r}) - (\boldsymbol{\sigma}_1 \cdot \boldsymbol{\sigma}_2), \tag{A.17}$$

where $\mathbf{r}$ is a unit vector along the direction of the relative coordinate of particles 1 and 2, while $r = |\mathbf{r}|$. Using the properties of Pauli matrices, it can be easily shown that

$$S_{12}(\boldsymbol{\sigma}_1 \cdot \boldsymbol{\sigma}_2) = (\boldsymbol{\sigma}_1 \cdot \boldsymbol{\sigma}_2)S_{12} = S_{12}. \tag{A.18}$$

This relation implies that S_{12} acts on $S = 1$ state only and annihilates $S = 0$ state. Moreover,

$$S_{12}^2 = 6 - 2S_{12} + 2(\boldsymbol{\sigma}_1 \cdot \boldsymbol{\sigma}_2) = 8 - 2S_{12}\ , \tag{A.19}$$

and

$$\boldsymbol{\nabla} S_{12} = \frac{3}{r^2}\Big[\boldsymbol{\sigma}_1(\boldsymbol{\sigma}_2 \cdot \mathbf{r}) + \boldsymbol{\sigma}_2(\boldsymbol{\sigma}_1 \cdot \mathbf{r}) - 2\frac{\mathbf{r}}{r^2}(\boldsymbol{\sigma}_1 \cdot \mathbf{r})(\boldsymbol{\sigma}_2 \cdot \mathbf{r})\Big] \tag{A.20}$$

$$\boldsymbol{\nabla}^2 S_{12} = -\frac{6}{r^2}S_{12}\ . \tag{A.21}$$

The above relations imply that for a generic function $u(r)$ depending on the radial coordinate r

$$(\boldsymbol{\nabla} u) \cdot (\boldsymbol{\nabla} S_{12}) = \left(\frac{du}{dr}\right)(\boldsymbol{\sigma}_1 \cdot \boldsymbol{\sigma}_2) \cdot (\boldsymbol{\nabla} S_{12}) = 0\ . \tag{A.22}$$

Further useful properties of the tensor operator are

$$\begin{aligned}
(\boldsymbol{\nabla} S_{12})^2 &= \frac{6}{r^2}(8 - S_{12}) \\
[S_{12}, (\boldsymbol{\nabla} S_{12})] &= \frac{36}{r} i(\mathbf{S} \times \mathbf{r}) \\
[S_{12}, (\boldsymbol{\nabla} S_{12})]\boldsymbol{\nabla} &= -\frac{36}{r^2}(\mathbf{L} \cdot \mathbf{S}) \\
[S_{12}, \boldsymbol{\nabla}^2 S_{12}] &= 0 \\
(\boldsymbol{\nabla} S_{12})[S_{12}, \boldsymbol{\nabla}] &= -(\boldsymbol{\nabla} S_{12})^2.
\end{aligned} \tag{A.23}$$

A.4 Change of representation

In this section, we present the change of representation used in Eq. (1.36) for a generic function x that can be expanded in the operatorial basis (1.32)

$$x = \sum_{p=1}^{6} x_{ij}^{p} O^{p} = \sum_{TS} [x_{TS} + \delta_{S1} x_{tT} S_{12}] P_{2S+1} \Pi_{2T+1}, \tag{A.24}$$

where the ordering of the operators is the same as in Eq. (1.32). We should explicitly write the projectors and the S_{12} operators in function of $(\boldsymbol{\sigma}_1 \cdot \boldsymbol{\sigma}_2)$ and $(\boldsymbol{\tau}_1 \cdot \boldsymbol{\tau}_2)$. Once we have done that, we get the following result

$$\begin{pmatrix} x_{00} \\ x_{01} \\ x_{10} \\ x_{11} \end{pmatrix} = \begin{pmatrix} 1 & -3 & -3 & 9 \\ 1 & -3 & 1 & -3 \\ 1 & 1 & -3 & -3 \\ 1 & 1 & 1 & 1 \end{pmatrix} \begin{pmatrix} x^1 \\ x^2 \\ x^3 \\ x^4 \end{pmatrix}, \tag{A.25}$$

$$\begin{pmatrix} x_{t0} \\ x_{t1} \end{pmatrix} = \begin{pmatrix} 1 & -3 \\ 1 & 1 \end{pmatrix} \begin{pmatrix} x^5 \\ x^6 \end{pmatrix}. \tag{A.26}$$

The inverse transformation can be obtained by inverting the square matrices.

Appendix B

Energy of asymmetric nuclear matter at $T \neq 0$

In Chapter 2, we have written the definitions of the thermodynamical quantities as a sum over spin-isospin-momentum states. In this Appendix, we will explicitly carry out the calculations using the wavefunction representation, so that we have practical expressions.

Let us start from (2.81), splitting the analysis into the kinetic and the potential terms. For the kinetic contribution, we have

$$\frac{\langle K\rangle}{N} = \frac{1}{N}\sum_{\lambda\mathbf{k}} \frac{k^2}{2m} n_\lambda(k,T) = \frac{1}{\varrho}\frac{1}{(2\pi)^3}\sum_\lambda \int d^3k \frac{k^2}{2m} n_\lambda(k,T). \tag{B.1}$$

In the case of finite-temperature, the further simplification would be to perform the angular integration. In case of $T = 0$, we have $n_\lambda(k,0) \to \theta(\mu_\lambda - e_{F_\lambda})$, and, therefore

$$\frac{\langle K\rangle}{N} = \sum_\lambda x_\lambda T_F^\lambda, \tag{B.2}$$

with

$$T_F^\lambda = \frac{3}{5}\frac{k_{F_\lambda}^2}{2m}. \tag{B.3}$$

For the potential energy term, the integration is slightly more difficult. We should remember that our wave functions are given by (2.4), so that

$$\frac{\langle V\rangle}{N} = \frac{1}{N}\frac{1}{2}\sum_{kk'}\sum_{\lambda\lambda'}\int d^3r_1 d^3r_2 \frac{e^{-i(\mathbf{k}\cdot\mathbf{r}_1+\mathbf{k}'\cdot\mathbf{r}_2)}}{V}\Big[\langle\lambda\lambda'|v^{\text{eff}}|\lambda\lambda'\rangle \frac{e^{i(\mathbf{k}\cdot\mathbf{r}_1+\mathbf{k}'\cdot\mathbf{r}_2)}}{V} - \tag{B.4}$$

$$\langle\lambda\lambda'|v^{\text{eff}}|\lambda'\lambda\rangle \frac{e^{i(\mathbf{k}\cdot\mathbf{r}_2+\mathbf{k}'\cdot\mathbf{r}_1)}}{V}\Big] n_\lambda(k,T) n_{\lambda'}(k',T) \tag{B.5}$$

where v^{eff} has 6 terms, corresponding to the six operators of Eq. (1.32). Continuing

the calculation and taking the continuum limit of momentum states,

$$\begin{aligned}\frac{\langle V\rangle}{N} &= \frac{1}{N}\frac{1}{2}\sum_{\lambda\lambda'}\int\frac{d^3k}{(2\pi)^3}\frac{d^3k'}{(2\pi)^3}\int d^3r_1 d^3r_2\Big[\,\langle\lambda\lambda'|v^{\rm eff}|\lambda\lambda'\rangle - \\ &\qquad\qquad \langle\lambda\lambda'|v^{\rm eff}|\lambda'\lambda\rangle\, e^{-i(\mathbf{k}-\mathbf{k}')\cdot(\mathbf{r}_1-\mathbf{r}_2)}\Big] n_\lambda(k,T) n_{\lambda'}(k',T) \\ &= \frac{V}{N}\frac{1}{2}\sum_{\lambda\lambda'}\int\frac{d^3k}{(2\pi)^3}\frac{d^3k'}{(2\pi)^3}\int d^3r\Big[\,\langle\lambda\lambda'|v^{\rm eff}|\lambda\lambda'\rangle - \\ &\qquad\qquad \langle\lambda\lambda'|v^{\rm eff}|\lambda'\lambda\rangle\, e^{-i(\mathbf{k}-\mathbf{k}')\cdot\mathbf{r}}\Big] n_\lambda(k,T) n_{\lambda'}(k',T) \\ &= \frac{\varrho}{2}\sum_{\lambda\lambda'} x_\lambda x_{\lambda'}\int d^3r\Big[\,\langle\lambda\lambda'|v^{\rm eff}|\lambda\lambda'\rangle - \langle\lambda\lambda'|v^{\rm eff}|\lambda'\lambda\rangle\, L_\lambda(r,T) L_{\lambda'}(r,T)\Big],\end{aligned} \tag{B.6}$$

where we have used the change of variables

$$\mathbf{r} = \mathbf{r}_1 - \mathbf{r}_2, \quad \mathbf{R} = \frac{\mathbf{r}_1 + \mathbf{r}_2}{2}, \tag{B.7}$$

Equation (2.89), and the definition of the generalised Slater function

$$L_\lambda(r,T) = \frac{1}{\varrho_\lambda}\int\frac{d^3k}{(2\pi)^3} e^{i\mathbf{k}\cdot\mathbf{r}} n_\lambda(k,T). \tag{B.8}$$

In the case of $T \to 0$, $L_\lambda(r,T) \to \ell(k_{F_\lambda} r)$ with $\ell(z) = 3(\sin z - z\cos z)/z^3$. Note that the Fermi distribution $n_\lambda(k,T)$ will be a numerical function, given that it would be calculated simultaneously to the spectrum with an iterative procedure to reach thermodynamic consistency.

The matrix elements $\langle\lambda\lambda'|v^{\rm eff}|\lambda\lambda'\rangle$ are calculated by using Eq. (2.54). We can define

$$V^{\rm D}_{\lambda\mu}(\mathbf{r}) = \sum_p v^p(r) A^p_{\lambda\mu}(\cos\theta), \tag{B.9}$$

$$V^{\rm E}_{\lambda\mu}(\mathbf{r}) = \sum_p v^p(r) B^p_{\lambda\mu}(\cos\theta), \tag{B.10}$$

where

$$A^p(\cos\theta) = \langle\lambda\mu|O^p_{ij}|\lambda\mu\rangle\,, \tag{B.11}$$

$$B^p(\cos\theta) = \langle\lambda\mu|O^p_{ij}|\mu\lambda\rangle\,, \tag{B.12}$$

and $\cos\theta = (\mathbf{r}\cdot\hat{\mathbf{z}})/|\mathbf{r}|$. The matrices $A^p(\cos\theta)$ and $B^p(\cos\theta)$ are

$$A^1 = \begin{pmatrix} 1 & 1 & 1 & 1 \\ 1 & 1 & 1 & 1 \\ 1 & 1 & 1 & 1 \\ 1 & 1 & 1 & 1 \end{pmatrix},\ A^2 = \begin{pmatrix} 1 & 1 & -1 & -1 \\ 1 & 1 & -1 & -1 \\ -1 & -1 & 1 & 1 \\ -1 & -1 & 1 & 1 \end{pmatrix},$$

$$A^3 = \begin{pmatrix} 1 & -1 & 1 & -1 \\ -1 & 1 & -1 & 1 \\ 1 & -1 & 1 & -1 \\ -1 & 1 & -1 & 1 \end{pmatrix},\ A^4 = \begin{pmatrix} 1 & -1 & -1 & 1 \\ -1 & 1 & 1 & -1 \\ -1 & 1 & 1 & -1 \\ 1 & -1 & -1 & 1 \end{pmatrix},$$

$$A^5 = A^2(3\cos^2\theta - 1),$$
$$A^6 = A^4(3\cos^2\theta - 1),$$

$$B^1 = \begin{pmatrix} 1 & 0 & 0 & 0 \\ 0 & 1 & 0 & 0 \\ 0 & 0 & 1 & 0 \\ 0 & 0 & 0 & 1 \end{pmatrix}, \; B^2 = \begin{pmatrix} 1 & 0 & 2 & 0 \\ 0 & 1 & 0 & 2 \\ 2 & 0 & 1 & 0 \\ 0 & 2 & 0 & 1 \end{pmatrix},$$

$$B^3 = \begin{pmatrix} 1 & 2 & 0 & 0 \\ 2 & 1 & 0 & 0 \\ 0 & 0 & 1 & 2 \\ 0 & 0 & 2 & 1 \end{pmatrix}, \; B^4 = \begin{pmatrix} 1 & 2 & 2 & 4 \\ 2 & 1 & 4 & 2 \\ 2 & 4 & 1 & 2 \\ 4 & 2 & 2 & 1 \end{pmatrix},$$

$$B^5 = \begin{pmatrix} 1 & -1 & 0 & 0 \\ -1 & 1 & 0 & 0 \\ 0 & 0 & 1 & -1 \\ 0 & 0 & -1 & 1 \end{pmatrix} (3\cos^2\theta - 1),$$

$$B^6 = \begin{pmatrix} 1 & -1 & 2 & -2 \\ -1 & 1 & -2 & 2 \\ 2 & -2 & 1 & -1 \\ -2 & 2 & -1 & 1 \end{pmatrix} (3\cos^2\theta - 1).$$

For the other quantities, a similar calculation can be performed. The single-particle energy, especially, is given by

$$e_{k\lambda} = \frac{\mathbf{k}^2}{2m} + \sum_{\lambda'} \varrho_{\lambda'} \int d^3r \Big[V^D_{\lambda\lambda'}(r) - V^E_{\lambda\lambda'}(r) j_0(kr) L_{\lambda'}(r,T) \Big] \tag{B.13}$$
$$+ \frac{1}{2} \sum_{\lambda'\lambda''} \varrho_{\lambda'} \varrho_{\lambda''} \int d^3r \Big\{ \Big[\frac{\partial}{\partial \varrho} V^D_{\lambda'\lambda''}(r) \Big] - \Big[\frac{\partial}{\partial \varrho} V^E_{\lambda'\lambda''}(r) \Big] L_{\lambda'}(r,T) L_{\lambda''}(r,T) \Big\},$$

with $j_0(z) = \sin z/z$.

Appendix C

Slater determinants

We can write the ground state of A non interacting fermions, denoted by Ψ_0, as a Slater determinant of single-particle states $\psi_{n_i}(x_i)$

$$\Psi_0 = \begin{vmatrix} \psi_1(x_1) & \psi_2(x_1) & \dots & \psi_N(x_1) \\ \psi_1(x_2) & \psi_2(x_2) & \dots & \psi_N(x_2) \\ \vdots & \vdots & \ddots & \vdots \\ \psi_1(x_N) & \psi_2(x_N) & \dots & \psi_N(x_N) \end{vmatrix} . \tag{C.1}$$

where $\psi_{n_i}(x_i)$ is given by Eq. (2.4). In this expression, x_j comprehends continuous and discrete degrees of freedom, i.e., position, spin and isospin.

In Chapter 4, when singling out particles in the cluster expansion, we have used the properties of the minors of (C.1). Let us single out only one particle through

$$\Psi_0 = \frac{1}{\sqrt{A}} \sum_{n_1} (-1)^{n+1} \psi_{n_1}(x_1) \Psi^0_{m\neq n_1}(x_2 \dots x_A) \,, \tag{C.2}$$

where $\Psi^0_{m\neq n_1}(x_2 \dots x_A)$ denotes the Slater determinant of system with $A-1$ particles and one hole in the state n_1. Here, $\Psi^0_{m\neq n_1}(x_2 \dots x_A)$ is a minor of (C.1) where the first row and the n_1th column have been removed.

If we want to single out two particles, we should take care of the antisymmetrisation property of a fermion state. Let us suppose we have particles in states n_1 and n_2, where n_1 will be removed first from the determinant. If $n_2 < n_1$, we should add the same multiplicative factor appearing in Eq. (C.2), $(-1)^{n_2+1}$. If $n_2 > n_1$, however, we should take into account that n_1 had already been removed from the determinant, so the multiplicative factor is actually $(-1)^{n_2}$. Then, we can write

$$\Psi_0 = \frac{1}{\sqrt{A(A-1)}} \Big[\sum_{n_1>n_2} (-1)^{n_1+n_2} \psi_{n_1}(x_1)\psi_{n_2}(x_2) \Psi^0_{m\neq n_1,n_2}(x_3 \dots x_A) + \sum_{n_1<n_2} (-1)^{n_1+n_2+1} \psi_{n_1}(x_1)\psi_{n_2}(x_2) \Psi^0_{m\neq n_1,n_2}(x_3 \dots x_A) \Big] . \tag{C.3}$$

We can also write this expression in a more compact way

$$\Psi_0 = \frac{1}{\sqrt{A(A-1)}} \sum_{n_1<n_2} (-1)^{n_1+n_2+1} \mathcal{A}[\psi_{n_1}(x_1)\psi_{n_2}(x_2)] \Psi^0_{m\neq n_1,n_2}(x_3 \dots x_A) \tag{C.4}$$

by exploring the antisymmetrisation operator defined

$$\mathcal{A} = 1 - \sum_{i<j} \hat{P}_{ij} + \sum_{i<j<k} (\hat{P}_{ij}\hat{P}_{jk} + \hat{P}_{ik}\hat{P}_{kj}) + \cdots \tag{C.5}$$

where $\hat{P}_{ij}$ is the two-particle exchange operator. It is defined by

$$\hat{P}_{ij}\psi_{n_i}(x_i)\psi_{n_j}(x_j) = \psi_{n_i}(x_j)\psi_{n_j}(x_i). \tag{C.6}$$

Using the spin-isospin exchange operator defined in Appendix A, we can write $\hat{P}_{ij}$ as

$$\hat{P}_{ij} = \hat{P}_{ij}^{\sigma\tau} \times \hat{P}_{ij}^{\mathbf{r}}, \tag{C.7}$$

with

$$\hat{P}_{ij}^{\mathbf{r}} = \exp[-i(\mathbf{k}_i - \mathbf{k}_j) \cdot (\mathbf{r}_i - \mathbf{r}_j)]. \tag{C.8}$$

For the calculations we have carried out, we also needed the $1p1h$ many-body state. Analogously to how we have isolated particles from Ψ_0, we can also isolate particles from $\Psi_{p;h}$ with

$$\Psi_{ph} = \frac{1}{\sqrt{A(A-1)}} \sum_{n_1<n_2} (-1)^{n_1+n_2+1} \mathcal{A}[\psi_{\tilde{n}_1}(x_1)\psi_{\tilde{n}_2}(x_2)]\Psi^{ph}_{m\neq\tilde{n}_1,\tilde{n}_2}(x_3 \ \ldots \ x_A)\,. \tag{C.9}$$

The indexes n_i have the values $1, \ldots, h, \ldots, A$, while

$$\begin{cases} \tilde{n}_i = p & \text{if } i = h, \\ \tilde{n}_i = n_i & \text{otherwise.} \end{cases} \tag{C.10}$$

Following these equations, we can generalise to the case of removing N particles

$$\begin{aligned} \Psi_0 = \sqrt{\frac{(A-N)!}{A!}} \sum_{n_1<\cdots<n_N} (-1)^{n_1+\cdots+n_N+1} \qquad & \text{(C.11)} \\ \times \mathcal{A}[\psi_{n_1}(x_1)\cdots\psi_{n_N}(x_N)]\Psi^0_{m\neq n_1,\ldots,n_N}(x_{N+1},\ldots,x_A), & \\ \Psi_{ph} = \sqrt{\frac{(A-N)!}{A!}} \sum_{\tilde{n}_1<\cdots<\tilde{n}_N} (-1)^{\tilde{n}_1+\cdots+\tilde{n}_N+1} \qquad & \text{(C.12)} \\ \times \mathcal{A}[\psi_{\tilde{n}_1}(x_1)\cdots\psi_{\tilde{n}_N}(x_N)]\Psi^{ph}_{\tilde{m}\neq\tilde{n}_1,\ldots,\tilde{n}_N}(x_{N+1},\ldots,x_A). & \end{aligned}$$

Moreover, with these definitions, we have that the minors are orthonormal, i.e.

$$\int dx_{N+1,\ldots,A} \Psi_0^{\dagger\, m\neq n_1,\ldots,n_N}(x_{N+1},\ldots,x_A)\Psi_0^{m\neq l_1,\ldots,l_N}(x_{N+1},\ldots,x_A) = \delta_{n_1 l_1}\ldots\delta_{n_N l_N}, \tag{C.13}$$

where it is assumed that $n_1 < \cdots < n_N$.

Bibliography

[1] C. A. Raithel, F. Özel, and V. Paschalidis, The Astrophysical Journal **875**, 12 (2019).

[2] C. A. Raithel, F. Özel, and D. Psaltis, The Astrophysical Journal **915**, 73 (2021).

[3] M. Dutra, O. Lourenço, S. S. Avancini, B. V. Carlson, A. Delfino, D. P. Menezes, C. Providência, S. Typel, and J. R. Stone, Phys. Rev. C **90**, 055203 (2014).

[4] H. Heiselberg and V. Pandharipande, Annual Review of Nuclear and Particle Science **50**, 481 (2000).

[5] O. Benhar, Particles **6**, 611 (2023).

[6] J. W. Clark, Prog. Part. Nucl. Phys. **2**, 89 (1979).

[7] S. Fantoni and A. Fabrocini, in *Microscopic Quantum Many-Body Theories and Their Applications*, Lecture Notes in Physics, Vol. 501, edited by Jesùs Navarro and Artur Polls (Springer, Berlin, Heidelberg, 1998) p. 119.

[8] O. Benhar and S. Fantoni, *Nuclear Matter Theory* (CRC Press, 2020).

[9] M. Baldo and G. Burgio, Progress in Particle and Nuclear Physics **91**, 203 (2016).

[10] S. Shlomo, V. Kolomietz, and G. Colo, The European Physical Journal A-Hadrons and Nuclei **30**, 23 (2006).

[11] G. Colò, Physics of Particles and Nuclei **39**, 286 (2008).

[12] M. B. Tsang, J. R. Stone, F. Camera, P. Danielewicz, S. Gandolfi, K. Hebeler, C. J. Horowitz, J. Lee, W. G. Lynch, Z. Kohley, R. Lemmon, P. Möller, T. Murakami, S. Riordan, X. Roca-Maza, F. Sammarruca, A. W. Steiner, I. Vidaña, and S. J. Yennello, Phys. Rev. C **86**, 015803 (2012).

[13] M. Oertel, M. Hempel, T. Klähn, and S. Typel, Rev. Mod. Phys. **89**, 015007 (2017).

[14] J. M. Lattimer, Particles **6**, 30 (2023).

[15] B.-A. Li and X. Han, Physics Letters B **727**, 276 (2013).

[16] F. J. Fattoyev, J. Carvajal, W. G. Newton, and B.-A. Li, Phys. Rev. C **87**, 015806 (2013).

[17] F. J. Fattoyev, W. Newton, and B.-A. Li, The European Physical Journal A **50**, 1 (2014).

[18] B.-A. Li, B.-J. Cai, W.-J. Xie, and N.-B. Zhang, Universe **7** (2021), 10.3390/universe7060182.

[19] W.-J. Xie and B.-A. Li, The Astrophysical Journal **883**, 174 (2019).

[20] S. M. A. Imam, T. Malik, C. Providência, and B. K. Agrawal, "Implications of comprehensive nuclear and astrophysics data on the equations of state of neutron star matter," (2024), arXiv:2401.06018 [nucl-th] .

[21] V. Carvalho, M. Ferreira, and C. Providência, "From ns observations to nuclear matter properties: a machine learning approach," (2024), arXiv:2401.05770 [nucl-th] .

[22] B. T. Reed, F. J. Fattoyev, C. J. Horowitz, and J. Piekarewicz, Phys. Rev. Lett. **126**, 172503 (2021).

[23] B. P. Abbott, R. Abbott, T. D. Abbott, F. Acernese, K. Ackley, C. Adams, T. Adams, P. Addesso, R. X. Adhikari, V. B. Adya, and et al. (The LIGO Scientific Collaboration and the Virgo Collaboration), Physical Review Letters **119**, 161101 (2017), arXiv:1710.05832 [gr-qc] .

[24] E. Yüksel and N. Paar, Physics Letters B **836**, 137622 (2023).

[25] I. Sick, Atoms **6** (2018), 10.3390/atoms6010002.

[26] J. Arrington, C. S. Armstrong, T. Averett, O. K. Baker, L. de Bever, C. W. Bochna, W. Boeglin, B. Bray, R. D. Carlini, G. Collins, C. Cothran, D. Crabb, D. Day, J. A. Dunne, D. Dutta, R. Ent, B. W. Filippone, A. Honegger, E. W. Hughes, J. Jensen, J. Jourdan, C. E. Keppel, D. M. Koltenuk, R. Lindgren, A. Lung, D. J. Mack, J. McCarthy, R. D. McKeown, D. Meekins, J. H. Mitchell, H. G. Mkrtchyan, G. Niculescu, I. Niculescu, T. Petitjean, O. Rondon, I. Sick, C. Smith, B. Terburg, W. F. Vulcan, S. A. Wood, C. Yan, J. Zhao, and B. Zihlmann, Phys. Rev. Lett. **82**, 2056 (1999).

[27] V. G. J. Stoks, R. A. M. Klomp, M. C. M. Rentmeester, and J. J. de Swart, Phys. Rev. C **48**, 792 (1993).

[28] H. Yukawa, Proc. Phys. Math. Soc. Jap. **17**, 48 (1935).

[29] J. Hu, H. Toki, and H. Shen, Scientific Reports **6**, 35590 (2016).

[30] R. B. Wiringa, V. G. J. Stoks, and R. Schiavilla, Phys. Rev. C **51**, 38 (1995).

[31] R. B. Wiringa and S. C. Pieper, Phys. Rev. Lett. **89**, 182501 (2002).

[32] O. Benhar, A. Lovato, and G. Camelio, The Astrophysical Journal **959**, 52 (2022).

[33] J.-i. Fujita and H. Miyazawa, Progress of Theoretical Physics **17**, 360 (1957), https://academic.oup.com/ptp/article-pdf/17/3/360/5252121/17-3-360.pdf .

[34] B. S. Pudliner, V. R. Pandharipande, J. Carlson, and R. B. Wiringa, Phys. Rev. Lett. **74**, 4396 (1995).

[35] J. Carlson, V. Pandharipande, and R. Wiringa, Nuclear Physics A **401**, 59 (1983).

[36] A. Lovato, I. Bombaci, D. Logoteta, M. Piarulli, and R. B. Wiringa, Phys. Rev. C **105**, 055808 (2022).

[37] A. Akmal, V. R. Pandharipande, and D. G. Ravenhall, Phys. Rev. C **58**, 1804 (1998).

[38] R. B. Wiringa, S. C. Pieper, J. Carlson, and V. R. Pandharipande, Phys. Rev. C **62**, 014001 (1995).

[39] E. Epelbaum, H.-W. Hammer, and U.-G. Meißner, Rev. Mod. Phys. **81**, 1773 (2009).

[40] R. Machleidt and D. Entem, Physics Reports **503**, 1 (2011).

[41] S. Weinberg, Physics Letters B **251**, 288 (1990).

[42] A. Gezerlis, I. Tews, E. Epelbaum, S. Gandolfi, K. Hebeler, A. Nogga, and A. Schwenk, Phys. Rev. Lett. **111**, 032501 (2013).

[43] A. Gezerlis, I. Tews, E. Epelbaum, M. Freunek, S. Gandolfi, K. Hebeler, A. Nogga, and A. Schwenk, Phys. Rev. C **90**, 054323 (2014).

[44] M. Piarulli, A. Baroni, L. Girlanda, A. Kievsky, A. Lovato, E. Lusk, L. E. Marcucci, S. C. Pieper, R. Schiavilla, M. Viviani, and R. B. Wiringa, Phys. Rev. Lett. **120**, 052503 (2018).

[45] T. Malik, H. Pais, and C. Providência, "Unified neutron star equations of state calibrated to nuclear properties," (2024), arXiv:2401.10842 [nucl-th] .

[46] J. Keller, K. Hebeler, C. J. Pethick, and A. Schwenk, "Neutron star matter as a dilute solution of protons in neutrons," (2024), arXiv:2401.13461 [nucl-th] .

[47] Y. Lim and A. Schwenk, "Symmetry energy and neutron star properties constrained by chiral effective field theory calculations," (2023), arXiv:2307.04063 [nucl-th] .

[48] M. G. Alford, L. Brodie, A. Haber, and I. Tews, Phys. Rev. C **106**, 055804 (2022).

[49] F. Sammarruca and R. Millerson, Universe **8** (2022), 10.3390/universe8020133.

[50] D. Lonardoni, I. Tews, S. Gandolfi, and J. Carlson, Phys. Rev. Res. **2**, 022033 (2020).

[51] Bombaci, Ignazio and Logoteta, Domenico, A&A **609**, A128 (2018).

[52] R. Essick, P. Landry, A. Schwenk, and I. Tews, Phys. Rev. C **104**, 065804 (2021).

[53] C. Drischler, J. Holt, and C. Wellenhofer, Annual Review of Nuclear and Particle Science **71**, 403 (2021), https://doi.org/10.1146/annurev-nucl-102419-041903 .

[54] M. Piarulli, L. Girlanda, R. Schiavilla, R. N. Pérez, J. E. Amaro, and E. R. Arriola, Phys. Rev. C **91**, 024003 (2015).

[55] I. Tews, J. Margueron, and S. Reddy, Phys. Rev. C **98**, 045804 (2018).

[56] I. Tews, J. Carlson, S. Gandolfi, and S. Reddy, The Astrophysical Journal **860**, 149 (2018).

[57] C. D. Capano, I. Tews, S. M. Brown, B. Margalit, S. De, S. Kumar, D. A. Brown, B. Krishnan, and S. Reddy, Nature Astronomy **4**, 625 (2020).

[58] O. Komoltsev and A. Kurkela, Phys. Rev. Lett. **128**, 202701 (2022).

[59] A. Sabatucci and O. Benhar, Phys. Rev. C **101**, 045807 (2020).

[60] J. L. Forest, V. R. Pandharipande, and J. L. Friar, Phys. Rev. C **52**, 568 (1995).

[61] J. Walecka, Annals of Physics **83**, 491 (1974).

[62] L. Baiotti and L. Rezzolla, Rep. Prog. in Phys. **80**, 096901 (2017).

[63] C. A. Raithel, V. Paschalidis, and F. Özel, Phys. Rev. D **104**, 063016 (2021).

[64] A. Figura, J.-J. Lu, G. F. Burgio, Z.-H. Li, and H.-J. Schulze, Phys. Rev. D **102**, 043006 (2020).

[65] A. Figura, F. Li, J.-J. Lu, G. F. Burgio, Z.-H. Li, and H.-J. Schulze, Phys. Rev. D **103**, 083012 (2021).

[66] P. Hammond, I. Hawke, and N. Andersson, Phys. Rev. D **104**, 103006 (2021).

[67] M. G. Alford, L. Bovard, M. Hanauske, L. Rezzolla, and K. Schwenzer, Phys. Rev. Lett. **120**, 041101 (2018).

[68] G. Camelio, A. Lovato, L. Gualtieri, O. Benhar, J. A. Pons, and V. Ferrari, Phys. Rev. D **96**, 043015 (2017).

[69] M. Prakash, I. Bombaci, M. Prakash, P. J. Ellis, J. M. Lattimer, and R. Knorren, Physics Reports **280**, 1 (1997).

[70] J. D. Kaplan, C. D. Ott, E. P. O'Connor, K. Kiuchi, L. Roberts, and M. Duez, The Astrophysical Journal **790**, 19 (2014).

[71] J.-J. Lu, Z.-H. Li, G. F. Burgio, A. Figura, and H.-J. Schulze, Phys. Rev. C **100**, 054335 (2019).

[72] H. Kanzawa, K. Oyamatsu, K. Sumiyoshi, and M. Takano, Nucl. Phys. A **791**, 232 (2007).

[73] O. Benhar and A. Lovato, Phys. Rev. C **96**, 054301 (2017).

[74] L. Tonetto and O. Benhar, Phys. Rev. D **106**, 103020 (2022).

[75] O. Benhar, A. Lovato, and L. Tonetto, Universe **9** (2023), 10.3390/universe9080345.

[76] B. D. DAY, Rev. Mod. Phys. **39**, 719 (1967).

[77] H. A. Bethe, Annual Review of Nuclear Science **21**, 93 (1971), https://doi.org/10.1146/annurev.ns.21.120171.000521 .

[78] M. Baldo, Nuclear Physics A **519**, 243 (1990).

[79] H. Müther and A. Polls, Progress in Particle and Nuclear Physics **45**, 243 (2000).

[80] M. Baldo and C. Maieron, Journal of Physics G: Nuclear and Particle Physics **34**, R243 (2007).

[81] R. Jastrow, Phys. Rev. **98**, 1479 (1955).

[82] J. W. Clark and P. Westhaus, Phys. Rev. **141**, 833 (1966).

[83] S. Fantoni and A. Fabrocini, in *Microscopic Quantum Many-Body Theories and Their Applications: Proceedings of a European Summer School Held at Valencia, Spain, 8–19 September 1997* (Springer, 2007) pp. 119–186.

[84] S. A. Rice, P. Gray, and A. G. De Rocco, American Journal of Physics **34**, 1209 (1966).

[85] S. Fantoni and S. Rosati, Nuovo Cim., A **20A** (1974), 10.1007/BF02727446.

[86] S. Fantoni and S. Rosati, Lettere al Nuovo Cimento (1971-1985) **10**, 545 (1974).

[87] V. R. Pandharipande and H. A. Bethe, Phys. Rev. C **7**, 1312 (1973).

[88] J. Dabrowski and W. Piechocki, Physics Letters B **84**, 20 (1979).

[89] S. Fantoni and S. Rosati, Nuovo Cimento. A **25**, 593 (1975).

[90] V. R. Pandharipande and R. B. Wiringa, Rev. Mod. Phys. **51**, 821 (1979).

[91] S. Fantoni and V. R. Pandharipande, Phys. Rev. C **37**, 1697 (1988).

[92] S. Cowell and V. R. Pandharipande, Phys. Rev. C **67**, 035504 (2003).

[93] S. T. Cowell and V. R. Pandharipande, Phys. Rev. **C70**, 035801 (2004).

[94] A. Lovato, C. Losa, and O. Benhar, Nuclear Physics A **901**, 22 (2013).

[95] A. Lovato, O. Benhar, S. Gandolfi, and C. Losa, Phys. Rev. C **89**, 025804 (2014).

[96] M. Valli, *Shear Viscosity of Neutron Matter from Realistic Nucleon-Nucleon Interactios*, Ph.D. thesis, Sapienza University of Rome (2007).

[97] D. Thouless, *The Quantum Mechanics of Many-Body Systems* (Academic Press, New York, 1961).

[98] L. D. Landau and E. M. Lifshitz, *Statistical Physics* (Pergamon Press, Oxford, 1969).

[99] N. M. Hugenholtz and L. Van Hove, Physica **24**, 363 (1958).

[100] A. Lejeune, P. Grange, M. Martzollf, and J. Cugnon, Nucl. Phys. A **453**, 189 (1986).

[101] J. Heyer, T. T. S. Kuo, J. P. Shen, and S. S. Wu, Phys. Lett. B **202**, 465 (1988).

[102] O. Benhar, *Structure and Dynamics of Compact Stars*, Vol. 1019 (Springer Nature, 2023).

[103] P. Haensel, A. Potekhin, and D. Yakovlev, *Neutron Stars 1: Equation of State and Structure*, Astrophysics and Space Science Library (Springer New York, 2007).

[104] S. L. Shapiro and S. A. Teukolsky, *Black holes, white dwarfs, and neutron stars: The physics of compact objects* (John Wiley & Sons, 2008).

[105] O. Benhar and M. Valli, Phys. Rev. Lett. **99**, 232501 (2007).

[106] M. Alford, A. Harutyunyan, and A. Sedrakian, Phys. Rev. D **104**, 103027 (2021).

[107] M. Baldo and L. S. Ferreira, Phys. Rev. C **59**, 682 (1999).

[108] G. F. Burgio and H.-J. Schulze, Astronomy & Astrophysics **518**, A10 (2010).

[109] S. Bernuzzi, M. Breschi, B. Daszuta, A. Endrizzi, D. Logoteta, V. Nedora, A. Perego, D. Radice, F. Schianchi, F. Zappa, I. Bombaci, and N. Ortiz, Monthly Notices of the Royal Astronomical Society **497**, 1488 (2020), https://academic.oup.com/mnras/article-pdf/497/2/1488/33558021/staa1860.pdf .

[110] V. Nedora, S. Bernuzzi, D. Radice, B. Daszuta, A. Endrizzi, A. Perego, A. Prakash, M. Safarzadeh, F. Schianchi, and D. Logoteta, The Astrophysical Journal **906**, 98 (2021).

[111] A. Bauswein, H.-T. Janka, and R. Oechslin, Phys. Rev. D **82**, 084043 (2010).

[112] K. Hotokezaka, K. Kyutoku, H. Okawa, M. Shibata, and K. Kiuchi, Phys. Rev. D **83**, 124008 (2011).

[113] A. Endrizzi, R. Ciolfi, B. Giacomazzo, W. Kastaun, and T. Kawamura, Classical and Quantum Gravity **33**, 164001 (2016).

[114] T. Dietrich, S. Bernuzzi, M. Ujevic, and W. Tichy, Phys. Rev. D **95**, 044045 (2017).

[115] T. Dietrich, M. Ujevic, W. Tichy, S. Bernuzzi, and B. Brügmann, Phys. Rev. D **95**, 024029 (2017).

[116] C. Constantinou, B. Muccioli, M. Prakash, and J. M. Lattimer, Annals of Physics **363**, 533 (2015).

[117] E. R. Most, S. P. Harris, C. Plumberg, M. G. Alford, J. Noronha, J. Noronha-Hostler, F. Pretorius, H. Witek, and N. Yunes, Monthly Notices of the Royal Astronomical Society **509**, 1096 (2021), https://academic.oup.com/mnras/article-pdf/509/1/1096/41135859/stab2793.pdf .

[118] E. R. Most, A. Haber, S. P. Harris, Z. Zhang, M. G. Alford, and J. Noronha, "Emergence of microphysical viscosity in binary neutron star post-merger dynamics," (2022), arXiv:2207.00442 [astro-ph.HE] .

[119] F. Zappa, S. Bernuzzi, D. Radice, and A. Perego, Monthly Notices of the Royal Astronomical Society **520**, 1481 (2023), https://academic.oup.com/mnras/article-pdf/520/1/1481/49116821/stad107.pdf .

[120] G. Camelio, L. Gavassino, M. Antonelli, S. Bernuzzi, and B. Haskell, Phys. Rev. D **107**, 103031 (2023).

[121] G. Camelio, L. Gavassino, M. Antonelli, S. Bernuzzi, and B. Haskell, Phys. Rev. D **107**, 103032 (2023).

[122] D. Yakovlev, A. Kaminker, O. Gnedin, and P. Haensel, Physics Reports **354**, 1 (2001).

[123] D. Yakovlev and C. Pethick, Annual Review of Astronomy and Astrophysics **42**, 169 (2004), https://doi.org/10.1146/annurev.astro.42.053102.134013 .

[124] S. Reddy, M. Prakash, and J. M. Lattimer, Phys. Rev. D **58**, 013009 (1998).

[125] A. Schmitt and P. Shternin, "Reaction rates and transport in neutron stars," in *The Physics and Astrophysics of Neutron Stars*, edited by L. Rezzolla, P. Pizzochero, D. I. Jones, N. Rea, and I. Vidaña (Springer International Publishing, Cham, 2018) pp. 455–574.

[126] L. F. Roberts, S. Reddy, and G. Shen, Phys. Rev. C **86**, 065803 (2012).

[127] L. F. Roberts and S. Reddy, Phys. Rev. C **95**, 045807 (2017).

[128] R. F. Sawyer, Phys. Rev. D **11**, 2740 (1975).

[129] R. F. Sawyer and A. Soni, The Astrophysical Journal **230**, 859 (1979).

[130] S. W. Bruenn, Astrophysical Journal Supplement Series **58**, 771 (1985).

[131] P. Haensel and A. J. Jerzak, Astronomy and Astrophysics **179**, 127 (1987).

[132] A. Burrows, S. Reddy, and T. A. Thompson, Nuclear Physics A **777**, 356 (2006), special Issue on Nuclear Astrophysics.

[133] M. E. Peskin and D. V. Schroeder, *An introduction to quantum field theory* (CRC press, 2018).

[134] Loffredo, Eleonora, Perego, Albino, Logoteta, Domenico, and Branchesi, Marica, A&A **672**, A124 (2023).

[135] M. G. Alford and S. P. Harris, Phys. Rev. C **98**, 065806 (2018).

[136] L. Baiotti, Progress in Particle and Nuclear Physics **109**, 103714 (2019).

[137] M. Alford, A. Harutyunyan, and A. Sedrakian, Phys. Rev. D **100**, 103021 (2019).

[138] A. Burrows and R. F. Sawyer, Phys. Rev. C **58**, 554 (1998).

[139] A. Burrows and R. F. Sawyer, Phys. Rev. C **59**, 510 (1999).

[140] O. Benhar and N. Farina, Physics Letters B **680**, 305 (2009).

[141] S. Cowell and V. R. Pandharipande, Phys. Rev. C **73**, 025801 (2006).

[142] M. Mendes, F. J. Fattoyev, A. Cumming, and C. Gale, The Astrophysical Journal **938**, 119 (2022).

[143] T. Sarkar, V. B. Thapa, and M. Sinha, Phys. Rev. C **108**, 035801 (2023).

[144] A. Dohi, N. Nishimura, H. Sotani, T. Noda, H.-L. Liu, S. Nagataki, and M. Hashimoto, The Astrophysical Journal **937**, 124 (2022).

[145] S. Fantoni and V. Pandharipande, Nuclear Physics A **473**, 234 (1987).

[146] G. Baym and C. Pethick, *Landau Fermi-liquid theory: concepts and applications* (John Wiley & Sons, 2008).

[147] T. Hahn, Computer Physics Communications **168**, 78 (2005).

[148] L. Suleiman, M. Oertel, and M. Mancini, Phys. Rev. C **108**, 035803 (2023).

[149] P. L. Espino, P. Hammond, D. Radice, S. Bernuzzi, R. Gamba, F. Zappa, L. F. L. Micchi, and A. Perego, (2023), arXiv:2311.00031 [astro-ph.HE] .